



UNIVERSIDAD NACIONAL DE COLOMBIA
Facultad de Ciencias - Departamento de Física

Physical properties of mixed-spin chains

Edgardo Segundo Solano Carrillo

For the acquisition of the degree of Master of Science in Physics

Advisor: Jerson Silva Valencia, Ph.D.

Correlated Systems Group
Bogotá, September 13 - 2010

*To the memoir of my mother, the great vision of my
father, and the constant support of my wife.*

Abstract

In this thesis we investigate some open questions about the physical properties of mixed-spin chains, which consists of an alternate array of spins S and s distributed along a line. We consider ground-state static properties of these systems such as magnetization plateaux, quantum phase transitions and entanglement. By developing a new molecular-field theory and using the density matrix renormalization group (DMRG) algorithm, we show that mixed-spin Ising chains with crystal-field anisotropy and external magnetic field, exhibit $2s + 1$ plateaux in the magnetization curve in a given range of the anisotropy parameters. This generalizes to mixed-spin chains the well-known results for Ising spin- S chains, where $2S + 1$ plateaux appear in the magnetization curve. We also proved the validity of the spin-wave theory for mixed-spin Heisenberg chains with crystal-field anisotropy in the easy-axis regime, which could be important in the theoretical investigation of the low-temperature properties of these systems. Using a measure of entanglement, the negativity, complemented with purity calculations, we were able to signal the quantum phase transition in a mixed-spin Heisenberg chain with positive single-ion anisotropy. We also showed that this anisotropy arbitrarily increases the characteristic temperatures above which the entanglement (and thus the quantum behavior) disappears in the system. When an external magnetic field is added, we showed how the critical point of the system can be calculated using entanglement and purity with more accuracy than customary condensed matter approaches. We then move to the description of ground-state dynamical properties of mixed-spin chains, investigated with a recent extension of DMRG to study real-time dynamics in one-dimensional quantum systems. We show results of the evolution of a domain-wall in a mixed $(S, s) = (1, \frac{1}{2})$ spin chain. By comparing with the evolution of a similar initial state prepared in a spin-1/2 chain with the same Hamiltonian, which has been reported recently, we encounter that the spreading of the domain-wall in our mixed-spin chain is much faster than that of the spin-1/2 chain, which is favorable for possible applications in the transport of bitwise information in magnetic nanostructures. We also investigated, in this case, the evolution of the von Neumann entropy between

the two halves of the mixed-spin chain, showing that it saturates faster than that of the spin-1/2 chain, a result which corroborates the faster propagation of information in the mixed-spin system. The following step in the thesis is the study of static properties of mixed-spin chains at finite temperature. After presenting the known common features in the thermodynamics of ferrimagnetic mixed-spin chains, we discuss the most up-to-date DMRG algorithms for finite temperatures. Then we give an example of a recently synthesized dimerized mixed-spin chain with a novel magnetic behavior, clarifying why this compound deviates from the well-known ferrimagnetic features in the thermal properties of mixed-spin chain. Finally we give an outlook of the implementation of a recent DMRG algorithm for calculating spectral functions at finite temperature. This will enable us to investigate, for the first time, quantities such as optical conductivity, spectral lines, and so on, for mixed-spin chains, which are related directly with experimental measurements.

Papers and presentations at meetings

During the research performed in this thesis, the following papers have been published in (and/or submitted to) national and international journals:

- E. Solano-Carrillo, R. Franco and J. Silva-Valencia, Magnetic properties of a ferrimagnetic mixed (1,3/2) spin chain with inhomogeneous crystal-field anisotropy, *Journal of Magnetism and Magnetic Materials* **322**, 1917-1922 (2010).
- E. Solano-Carrillo, R. Franco and J. Silva-Valencia, Formation of quantum magnetization plateaux in mixed-spin Ising chains with single-ion anisotropy, *Journal of Magnetism and Magnetic Materials* **322**, 3760-3764 (2010).
- E. Solano-Carrillo, R. Franco and J. Silva-Valencia, Interacting spin-wave dispersion relations of ferrimagnetic Heisenberg chains with crystal-field anisotropy, in Press, *Solid State Communications*. (2010). DOI:10.1016/j.ssc.2010.08.003
- E. Solano-Carrillo, R. Franco and J. Silva-Valencia, Unconventional features of the low-temperature properties of a dimerized quantum mixed-spin chain, in Press, *Physica Status Solidi B* (2010). DOI: 10.1002/pssb.201046183
- E. Solano-Carrillo, R. Franco and J. Silva-Valencia, Pairwise entanglement and critical behavior of an anisotropic ferrimagnetic spin chain, submitted to *Physics Letters A* (2010).
- E. Solano-Carrillo, R. Franco and J. Silva-Valencia, Entanglement and quantum phase transition in a mixed-spin Heisenberg chain with single-ion anisotropy, submitted to *Physica A* (2010).
- E. Solano-Carrillo, R. Franco and J. Silva-Valencia, Efecto de la inhomogeneidad en la anisotropía de un único ion en una cadena de espines mixtos (1,3/2), submitted to *Revista Colombiana de Física* (2010).

Some results obtained in this work have been presented in:

- The 11th Joint MMM/Intermag Conference, 18-22 January 2010, Washington DC-USA. Work presented as an *oral talk*: “Magnetic properties of a ferrimagnetic mixed $(1,3/2)$ spin chain with unhomogeneous crystal-field anisotropy”.
- Workshop on the “Dynamics of Strongly Correlated Quantum Systems”, The Abdus Salam International Centre for Theoretical Physics (ICTP), 21-25 June 2010, Trieste-Italy.
- IX Latin American Workshop on Magnetism, Magnetic Materials and Their Applications, July 25-29, 2010, Manizales-Colombia. Work presented as a *poster*: “Entanglement and quantum phase transition in a mixed-spin Heisenberg chain with single-ion anisotropy”.
- XXIII Congreso Nacional de Física, 5-9 October 2009, Santa Marta-Colombia. Work presented as an *oral talk*: “Efecto de la inhomogeneidad en la anisotropía de un único ion en una cadena de espines mixtos $(1,3/2)$ ”.

Acknowledgements

First of all I want to thank Prof. Jereson Silva Valencia for advising me throughout this work. He gave me a constant support and was always interested in the progress of my calculations. It has been a pleasure to work in his research group. I am also very grateful to the Universidad Nacional de Colombia for awarding me with the “Estudiante Sobresaliente de Posgrado” scholarship, supporting this thesis through the project DIB 8003316, and allowing me to collaborate with the research projects: “Modelo de Anderson: nuevas técnicas para tratarlo y aplicaciones” Res. No. 2671 de 2008, “DMRG, entrelazamiento cuántico y sistemas correlacionados” Res. No. 205 de 2010, and “Termoelectricidad en sistemas nanoscópicos” Res. No. 1780 de 2010. I also want to thank the Mazda Foundation for the Arts and Science for awarding me one of its prestigious fellowships, and the Foundation for the Promotion of Research and Technology, Banco de la República, for the financial support to attend international conference.

On the other hand, I want to express my deep gratitude to Adrian Feiguin, from University of Wyoming (USA), for suggesting me one of the solutions to the problems which I encountered in the implementation of the ancilla DMRG for finite temperatures. I want to thank Shigetoshi Sota, from Yukawa Institute for Theoretical Physics, Kyoto University (JAPAN), for his fruitful recommendations for the implementation of the Low-temperature DMRG algorithm using regulated polynomial expansions. I am also grateful to Steven R. White, from University of California at Irvine (USA), for taking a time to comment about my implementation of the DMRG algorithm for finite temperature using METTS.

Last but not least I would like to thank my wife for her continuous support and her tenacity for accompanying me in all the developing moments of this work, and to my family for always being there over all the years.

Introduction

The study of strongly correlated systems in one dimension has received a lot of attention in the past few years. This interest has been triggered by the synthesis of magnetic materials, which in a wide range of temperatures, can be described by three-dimensional arrangements of almost decoupled spin chains. Among the whole compendium of these systems, ferrimagnetic *mixed-spin chains* have attracted the curiosity of many specialists recently. These chains are molecular magnets containing two kinds of distinct magnetic ions (usually transition metal ions) with spin quantum numbers S and s , which are distributed, in the majority of cases, alternately in a line throughout the lattice. Theoretical investigations at low temperatures into these chains have shown that their ground states display both ferromagnetic and antiferromagnetic long-ranged order. That is, the elementary excitations have two branches in the energy spectrum: while ferromagnetic excitations, which reduces the magnetization of the system, are gapless; the antiferromagnetic ones, increasing the magnetization, are gapped, which leads to a temperature dependence of the specific heat and the magnetic susceptibility as $T^{1/2}$ and T^{-1} , respectively, at low temperatures. The most studied system has been the mixed $(S, s) = (1, \frac{1}{2})$ spin chain, due to the simplicity of the spin mixture and its early realization in the compound $\text{NiCu}(\text{pba})(\text{H}_2\text{O})_3 \cdot 2\text{H}_2\text{O}$. Other spin mixtures have also been studied, such as $(S, s) = (\frac{5}{2}, 1)$ which is present in the ferromagnetic compound $\text{MnNi}(\text{NO}_2)_4(\text{ethylenediamine})_2$, and the $(S, s) = (2, 1)$ present in the ferrimagnetic system $[\text{Mn}(\text{Cl}_4\text{saltmen})\text{Ni}(\text{pao})_2(\text{bpy})]\text{PF}_6$, among others.

- In this context, it is natural to ask: which properties are common to all the mixed-spin chains, and which ones, if any, are variable when we change the combination (S, s) ? Can we find instances of mixed-spin chains for which the thermal properties could be different from those ferrimagnetic properties usually attributed to these materials?.

At zero temperature, where thermal fluctuations are no longer present, there appears a variety of interesting quantum critical phenomena in spin chains owing to competing interactions and low dimensionality. One of the most studied topics, similar to the quantized

steps in the resistivity of quantum Hall systems, is the appearance of *plateaux* (steps) in the magnetization curve of some chains, which reveals a macroscopic quantization. The origins of these plateaux are attributed, depending on the system, to mechanisms such as dimerization, frustration, periodic field, crystal-field (or single-ion) anisotropy, and so on. From an experimental point of view, one of the most exciting materials is NH_4CuCl_3 , where just two plateaux at $1/4$ and $3/4$ of the saturation magnetization have been observed due to quantum effects. As to the number of plateaux which appear for a certain system (if any), there is a general necessary condition which selects the values of magnetization for which the plateaux are allowed to appear, but leaves the formation mechanisms unexplained. For mixed-spin (S, s) ferrimagnetic Heisenberg chains, for example, it can be shown that the magnetization curve generally exhibits $2s + 1$ plateaux (including saturation) without any anisotropy and any bond polymerization. For classical Ising chains with single-ion anisotropy, there have been also a great interest in studying magnetization plateaux, since they have been proposed as models for describing certain molecular-based magnets of experimental interest. In this case, it has been found that for spin- S chains with positive single-ion anisotropy, the magnetization curve displays $2S + 1$ plateaux, but nothing has been said about mixed-spin Ising chains. So a pertinent question is:

- Is there any rule as to the number of plateaux in mixed-spin Ising chains with positive single-ion anisotropy?.

A magnetization plateau is just an interesting example of what we may encounter in the ground state (or even at low temperatures) of low-dimensional systems. Since we learn about nature by observing its response to controlled external perturbations, the most intriguing phenomena that we can investigate at absolute zero are quantum phase transitions, which are manifestations of the competence between external stimuli on a system and its internal couplings. Recently there has appeared, in addition to many-body approaches from condensed matter theory, resources from the quantum information community which allows to take another route for describing quantum phase transitions. The quantification of *entanglement*, one of the greatest mysteries of physics, have enabled the signaling of quantum critical points for several many-body strongly correlated quantum systems. For mixed-spin chains, there are very few works to describe quantum critical points by means of measures of entanglement, all of them considering only a small number of sites, which are not always satisfactory to mimic the thermodynamic limit of solid-state systems. This situation raises an immediate query:

- Are we able to detect quantum critical points in large mixed-spin chains using measures of entanglement?.

From this scenario, it follows that a system can be prepared in one of the phases and then obliged to relax under the interactions present in another phase, with a subsequent description of the dynamics of entanglement. Another possibility is to prepare a state in the system, which is not an eigenstate of its Hamiltonian, and let it evolve. Currently, these are hot topics of interest, and to the best of our knowledge, have not been studied in mixed-spin chains. In general, spin dynamics (the core of spintronics and possibly the basis for future quantum computers), has not been investigated for mixed-spin chain. This motivate us to perform, for the first time, theoretical calculations of the real-time dynamics of large mixed-spin systems, in order to test their suitability for quantum information transport.

In this thesis we aim at answering the aforementioned questions which, we think, comprises an important part of the research which has been conducted in recent years on mixed-spin chains, as well as new contributions from us. The thesis is organized as follows: in chapter 1 we introduce the most basic language of quantum magnetism, which is used in the rest of the work. In chapter 2 we start by defining the mixed-spin chains, giving examples and showing some known results. Then we motivate and describe the main technique used in our research: the density matrix renormalization group (DMRG); which is the most powerful method nowadays to study one-dimensional strongly correlated quantum systems. In the rest of the chapter, we present our results for the ground-state static properties which give *positive* answers to the questions 2 and 3. In chapter 3 we describe a recent extension of DMRG to study real-time dynamics of one-dimensional systems with nearest-neighbor interactions. With this, we reproduce some known results and later we show, for the first time, results for the domain-wall dynamics in mixed-spin chains, with a subsequent preliminary analysis of the dynamics of entanglement measured with the von Neumann entropy. In chapter 4 we describe known common features to all ferrimagnetic chains and, after discussing the most up-to-date DMRG algorithms for finite temperatures implemented in this thesis, we give an example of a recently synthesized dimerized mixed-spin chain which deviates from the well-known ferrimagnetic behavior, clarifying the mechanisms which cause this deviation; with this we answer the interrogants in question 1. Finally we give an outlook of a future related work, where we plan to implement a DMRG algorithm for mixed-spin chains proposed last year (for uniform chains) to calculate spectral functions of one-dimensional systems at finite temperatures, which is at the frontiers of condensed matter physics.

Contents

Abstract	I
Papers and presentations at meetings	III
Acknowledgements	V
Introduction	VI
1 The language of quantum magnetism	1
1.1 Model Hamiltonians	1
1.2 Long range order	3
1.3 Excitations	5
2 Ground-state static properties	7
2.1 Ferrimagnetic (mixed-spin) chains	7
2.2 Exact diagonalization of the Hamiltonian	9
2.3 Density matrix renormalization group (DMRG)	10
2.3.1 Infinite-system algorithm	14
2.3.2 Finite-system algorithm	15
2.4 Magnetization plateaux in general anisotropic Ising chains	16
2.4.1 Transfer-matrix method	17
2.4.2 Molecular-field theory	18
2.5 Interacting spin-wave dispersions of Heisenberg chains	24
2.5.1 Second-order spin-wave theory	25
2.5.2 Numerical analysis with DMRG	28
2.6 Entanglement and quantum phase transitions	30
2.6.1 Mixed-spin Heisenberg chain with single-ion anisotropy	31

CONTENTS

2.6.2	Adding an external magnetic field	38
3	Ground-state dynamical properties	43
3.1	Dynamics with DMRG	43
3.2	Adaptive time-dependent DMRG	46
3.3	Spectral function of the spin-1 Heisenberg chain	49
3.4	Evolution of a domain wall in a spin-1/2 chain	51
3.5	Domain-wall dynamics in a mixed-spin XX chain	53
3.6	Evolution of entanglement entropy	54
4	Static properties at finite temperature	57
4.1	Inherent features of one-dimensional ferrimagnets	57
4.2	Purification as an alternative to DMRG at $T > 0$	59
4.3	Unconventional features of a dimerized chain	62
4.3.1	The spin-wave approach	64
4.3.2	DMRG results at $T = 0$	65
4.3.3	Specific heat and magnetic susceptibility	69
	Conclusions and outlook	74
A	Recent DMRG algorithms at $T > 0$	76
A.1	Regulated polynomial expansion	76
A.2	Minimally entangled typical thermal states	78
	Bibliography	80

The language of quantum magnetism

Quantum magnetism is one of the most active areas of research in condensed matter physics. It clearly has a quantum-mechanical basis since the microscopic exchange interactions arise entirely from the exclusion principle, in conjunction with repulsive interactions between electrons. There is significant research interest specially in low-dimensional quantum spin systems. Such systems have a large number of experimental realizations and exhibit a variety of phenomena the origin of which can be attributed to quantum effects and low dimensions. In this chapter we give a brief introduction to the most basic language of this fascinating area of physics.

1.1 Model Hamiltonians

One of the approaches to understand the magnetic behavior of solids is to consider particular microscopic models of the magnetic interaction. The fundamental entity is the magnetic moment $\boldsymbol{\mu} = \mu_B(g_L\mathbf{L} + g_S\mathbf{S})$ which couples the orbital \mathbf{L} and spin \mathbf{S} angular momentum of the constituting atoms to produce collectively a variety of phenomena like ferromagnetism, paramagnetism, among others. Here μ_B is the Bohr's magneton and the g 's are Landé factors. The most well-known model of interacting moments is the Heisenberg model which focus on the energy contribution coming from spin. The corresponding Hamiltonian is

$$\mathcal{H} = \sum_{\langle ij \rangle} J_{ij} \mathbf{S}_i \cdot \mathbf{S}_j, \quad (1.1.1)$$

where \mathbf{S}_i is the spin operator located on the lattice site i and J_{ij} is the strength of the exchange interaction, which is nothing more than an electrostatic interaction arising because charges of the same sign cost energy when they are close together and save energy when they are apart [1]. The strength of the exchange interaction falls down rapidly as

the distance between interacting spins increases. For many solids, the sites i and j are nearest-neighbors on the lattice, which is denoted by brackets in Eq. (1.1.1). We may find, for example, (isotropic) systems where J_{ij} have the same magnitude J for all the nearest-neighbors interactions; examples of (dimerized) systems in which the strengths of the exchange interactions between successive pairs of spins are not the same, and of (frustrated) systems where nearest-neighbors and next-nearest-neighbors exchange interactions are important [2].

Real magnetic solids are three-dimensional but they can be effectively considered as low-dimensional systems if the exchange interactions have different strengths in different directions. To give an example, a magnetic solid may consist of *spin chains*. The solid may be considered as a linear chain compound if the intra-chain exchange interactions are much stronger than the inter-chain ones. In a planar magnetic system, the dominant exchange interactions are intra-planar. Several examples of low-dimensional magnetic systems are given in Ref. [3]. Taking account of these anisotropies of the strength of the exchange interactions, one can write the fully anisotropic Heisenberg Hamiltonian in a spin chain of L sites as

$$\mathcal{H}_{XYZ} = \sum_{i=1}^{L-1} [J_x S_i^x S_{i+1}^x + J_y S_i^y S_{i+1}^y + J_z S_i^z S_{i+1}^z], \quad (1.1.2)$$

where we concentrate only on nearest-neighbor interactions. The special cases of this Hamiltonian are: the Ising model ($J_x = J_y = 0$) in which the individual spins are restricted to lie parallel or antiparallel to a particular direction, the XY model ($J_z = 0$) in which the spins are free to point anywhere in a fixed plane, the XXX or isotropic Heisenberg model ($J_x = J_y = J_z$) and the XXZ or anisotropic Heisenberg ($J_x = J_y \neq J_z$) model where the spins are free to point in any direction.

When orbital contributions are considered, the magnetic energy shows a dependence upon the orientation of the moments relative to the crystal axes. This is known as *single-ion (or crystal-field) anisotropy* and is determined by the interaction between the orbital state (orbitals modelled as negative point charges in crystal field theory) of a magnetic ion and the surrounding crystalline field which is very strong. This field is an electric field derived from neighboring atoms in the crystal, therefore it has the symmetry of the lattice. The magnetocrystalline interaction (as this is usually called) is transferred to the spin moments via the spin-orbit coupling, giving a weaker d -electron coupling of the spins to the crystal lattice. This effect can be included by adding a term to the Hamiltonian to represent the energetic preference for the spin to lie along particular crystalline directions because of the crystal field. For an uniaxial crystal (i.e. one with a particular axis such that the energy just

depends on the angle of the spin with that axis) the term is

$$\mathcal{H}_{\text{SI}} = D(S^z)^2, \quad (1.1.3)$$

where the anisotropy parameter D is proportional to the squared spin-orbit parameter.

The spin quantum number for each spin on the chain depends on the atom. It can be determined easily using the first Hund's rule, which states that in the ground state electrons are accommodated in the orbitals so as to maximize the total spin of the free atom. For example, if we have chains with Cu^{2+} ($3d^9$) the spin quantum number is $S = \frac{1}{2}$, with Mn^{2+} ($3d^5$) it is $S = \frac{5}{2}$, etc. A commonly studied family of systems well described by the above mentioned models is based in crystals of the type ABX_3 where A is a non-magnetic cation of a single charge, B is a doubly charged magnetic cation and X is a halide anion. This leads to a simple hexagonal lattice with transition metal ions forming chains along the c direction. For example CsCoCl_3 behaves almost as a one-dimensional Ising chain since the anisotropy constrains the spins along a particular direction, KCuF_3 behaves like a one-dimensional isotropic Heisenberg spin chain, as do a number of Cu salts with organic ligands.

1.2 Long range order

There are several types of magnetic ground states which can be produced by the exchange interactions between magnetic moments. The different ground states include *ferromagnets* in which all the magnetic moments are in parallel alignment, *antiferromagnets* in which adjacent magnetic moments lie in antiparallel alignment (Néel order), *spiral* and *helical structures* in which the direction of the magnetic moment precesses around a cone or a circle as one moves from one site to the next, and *spin glasses* in which the magnetic moments lie in frozen random arrangements. To see how the exchange interaction leads to magnetic order in the ground state, let us consider the isotropic Heisenberg Hamiltonian. If we treat the spins as classical vectors, each nearest-neighbor spin pair has an interaction energy $JS^2 \cos \theta$ where θ is the angle between spin orientations. When $J < 0$, the lowest energy is achieved when $\theta = 0$, i.e. the interacting spins are parallel (ferromagnetism). When $J > 0$, the lowest energy is achieved for $\theta = \pi$, i.e. the nearest-neighbor spins are antiparallel (antiferromagnetism). This gives only a classical insight of what might happen. However, magnetism is a purely quantum phenomenon and the Hamiltonian in Eq. (1.1.1) has to be treated quantum mechanically rather than classically, as we shall do in the next chapter.

The appearance of spontaneous order at low temperature is a fundamental phenomenon of condensed matter physics. Ferromagnets, antiferromagnets, liquid crystal and super-

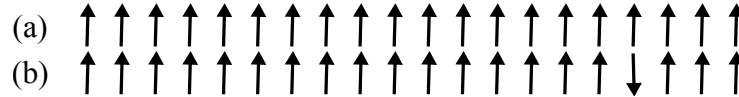


Figure 1.1: The one-dimensional Ising model. (a) The ground state contains all L spins aligned ferromagnetically. (b) A single defect is added.

conductors are all ordered phases, as is the solid state itself. All these phenomena share some fundamental properties and characteristics. For example, they are all characterized by a temperature dependence in which some relevant physical property shows a marked difference above and below a *critical temperature* T_c . For each phase, one can define an *order parameter* which is zero for $T > T_c$ and non-zero for $T < T_c$. This quantity therefore acts as an indicator of whether or not the system is ordered. In the case of ferromagnetism, the order parameter is simply the magnetization, which is the average density of magnetic moments in the material and T_c is the Curie temperature (in antiferromagnetism T_c is the Néel temperature) which divides the paramagnetic and ferromagnetic phases.

The phase transitions which we have mentioned are all driven by temperature. In such phase transitions, it is the thermal fluctuations which destroy the order as the sample is warmed through its transition. However, if one has a transition which is controlled by some other variable (such as pressure, magnetic field, etc.) then at some critical value of this variable one can have a transition which can, in principle, occur at absolute zero. Such a zero temperature phase transition is called *quantum phase transition* and the point at which it occurs is a *quantum critical point*. The relevant fluctuations are no longer thermal but the quantum mechanical fluctuations determined by Heisenberg's uncertainty principle. An example is the Ising quantum magnet LiHoF_4 in which the ferromagnetic order can be destroyed at absolute zero by applying a magnetic field perpendicular to the easy-axis of the Ising spins. This counterintuitive behaviour occurs because the magnetic field facilitates quantum tunneling between the up and down spin states. Above a critical magnetic field the quantum fluctuations are sufficient to destroy the ferromagnetic order.

It is easy to show that for one-dimensional systems there can never occur a (temperature-driven) phase transition at finite temperatures. For this, we consider the ferromagnetic Ising limit of Eq. (1.1.2) in a chain with L spins. Here the ground state is obtained by having all adjacent spins lined up ferromagnetically as illustrated in Fig. 1.1(a). Now consider adding one "mistake", a single defect as shown in Fig. 1.1(b). This cost an extra energy $E = J$ because we have to turn one favourable interaction into an unfavourable one. However, there is an entropy gain equal to $S = k_B \ln(L)$ because we can put the defect in any one of the L places. As we let the chain get very large ($L \rightarrow \infty$) the energy cost of a defect remains the same (J) but the entropy gain becomes infinite. The thermodynamic

properties of the system are determined by the free energy $F = E - TS$ so that, as long as the temperature is not zero, the entropy consideration means that the presence of the defect causes $F \rightarrow -\infty$. Since this is a very stable situation, it means that defects can spontaneously form at finite temperatures, which implies that no long range order occurs for $T > 0$. Another way of saying this is that $T_c = 0$, i.e. a transition to an ordered phase is possible only at absolute zero. Since this consideration is valid for all models on one-dimensional lattices (entropy always wins in one dimension) we conclude that no phase transition at $T \neq 0$ is possible in one-dimensional systems, so we have to incline our attention only to quantum phase transitions. In general, a long-range order, of the Néel type for example, exists in a magnetic system if the correlation function $\mathcal{C}_r \equiv \langle \mathbf{S}_0 \cdot \mathbf{S}_r \rangle$ between a spin at the origin and a spin at distance r apart is finite for infinitely separated spins (in the thermodynamic limit), that is if the condition $\lim_{r \rightarrow \infty} \mathcal{C}_r \neq 0$ holds. At $T = 0$, the expectation value is taken with the ground state and at $T \neq 0$ the state is given by the thermal density matrix.

1.3 Excitations

The antiferromagnetic ground state is, in general, far more complicated than the ferromagnetic one. The ground state properties of quantum antiferromagnets not only have important physical consequences, they also contain some fascinating surprises. In three-dimensional Heisenberg systems, the elementary excitations are called *magnons*, and consist of delocalized defects as the one shown in Fig. 1.1(b). These disturbances propagate in the spin lattice, and the low-energy structure (and thus the low-temperature properties) derived from them can be investigated with the spin-wave theory [4, 5]. In one dimension, the simplest system which is the spin-1/2 Heisenberg antiferromagnet can be solved exactly by the Bethe ansatz [6]. The correlation functions have a power law decay and there exists local excitations with arbitrary low energy, i.e. there is no *gap* in the spectrum immediately above the ground-state energy. For general half-odd integer spin chains described by a Hamiltonian respecting translational and rotational symmetry, the Lieb-Schultz-Mattis (LSM) theorem [7] says that the system either has a gapless excitation spectrum or has degenerate ground states corresponding to spontaneously broken translational symmetry. However, there can be an instability known as *spin-Pierls instability* which can open up a gap in these systems. The driving force of this intrinsic lattice instability is the magnetoelastic coupling between the one-dimensional electronic structure and the three-dimensional lattice vibrations (phonons). This coupling arises because the exchange energy of the chains is a function of the separation between adjacent lattice sites

so a distortion of the lattice influences the magnetic energy.

One might expect a gapless energy spectrum in any one-dimensional isotropic quantum antiferromagnetic chain. Haldane, however, argued that if the spin is integer then the one-dimensional Heisenberg antiferromagnet has completely different properties [8, 9]. He concluded that the ground-state correlation functions have exponential decay and there is a gap in the spectrum above the ground-state energy. There is both experimental and numerical support for these conclusions [10–12]. When a magnetic field H is applied, Oshikawa, Yamanaka and Affleck (OYA) extended the LSM theorem in the following way [13]: translationally invariant spin chains in an applied magnetic field can have a gapped excitation spectrum, without breaking translational symmetry, only when the magnetization per unit cell $m = N^{-1} \sum_{j=1}^N S_j^z$ obeys the relation

$$S_{\text{unit}} - m = \text{integer}, \quad (1.3.1)$$

where S_{unit} is the sum of spins over all the sites in the unit period. The gapped phases correspond to *magnetization plateaux* in the m vs. H characteristic curve, at the quantized values of m which satisfy the OYA criterion Eq. (1.3.1). The appearance of plateaux in the magnetization curve of one-dimensional chains is a fascinating topic of recent interest [14], since it reveals the quantization of magnetization. In the next chapter, we are going to describe our contributions to this topic of condensed matter physics.

It has become apparent that the study of magnetism (arguably already dating back several millennia) has acquired a new urgency along with its new vocabulary. But even when applications evolve rapidly in time, they are still secondary to the immutable basic physical principles that empower them. For an excellent introduction to the state of the arts in quantum magnetism as well as applications we refer the reader to Ref. [15]. In this thesis, it only suffices to keep in mind the above mentioned topics, in order to follow the material presented. Wherever we talk about other topics without giving a detailed exposition, we give the corresponding references for more completeness.

Ground-state static properties

Since the discoveries of experimental methods to cool samples down to fractions of Kelvin, there has been considerable efforts to understand the low-temperature properties of condensed matter systems. We have learned that some materials have a very marked change of their thermodynamic properties known as a phase transition. At zero temperature, quantum systems have zero-point fluctuations which can lead them to suffer quantum phase transitions. In this chapter we investigate ground-state properties, such as the magnetization curve, of mixed-spin chains emphasizing, in some cases, the relevant quantum phase transitions.

2.1 Ferrimagnetic (mixed-spin) chains

Very often antiferromagnetism occurs in systems which can be considered as two interpenetrating sublattices, on one of which the magnetic moments point up and on the other of which they point down. These two sublattices are assumed equivalent. But what if there is some crystallographic reason for them not to be equivalent? In this case the magnetization of the two sublattices may not be equal and opposite (as is the case for antiferromagnets) and therefore will not cancel out: the material will have a net magnetization. This phenomenon is known as *ferrimagnetism*. Sometimes one sublattice can dominate the magnetization at low temperature but another dominates at higher temperature; in this case the net magnetization can be reduced to zero and change sign at a temperature known as the *compensation temperature*. Most ferrimagnets are electrical insulators and this fact is responsible for many of their practical applications. Ferromagnets are often metallic and thus are unsuitable in applications in which an oscillating magnetic field is involved. A rapidly changing magnetic field induces a voltage and causes currents (known as eddy

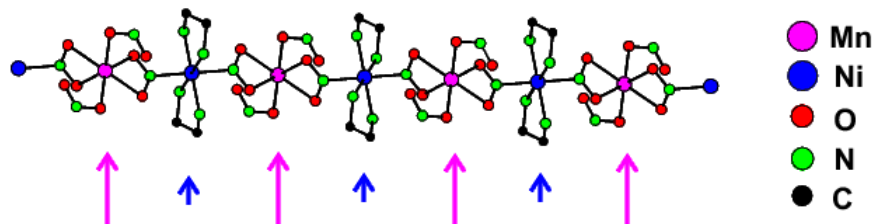


Figure 2.1: One chain segment of the structure of $\text{MnNi}(\text{NO}_2)_4(\text{en})_2$ showing the alternating arrangement of Mn ($S = 5/2$) and Ni ($s = 1$) ions. A full description of the structure is presented in Ref. [16].

currents) to flow in conductors. These currents cause resistive heating in a metal (eddy current losses). Many ferrimagnets therefore can be used when a material with a spontaneous magnetization is required to operate at high frequencies, since the induced voltage will not be able to cause any significant eddy currents to flow in an insulator. Solid ferrite cores are used in many high frequency applications including aerials and transformers requiring high permeability and low energy loss, as well as applications in microwave components; also many ferrimagnets are more corrosion resistant than metallic ferromagnets since they are already oxides.

Low-dimensional quantum ferrimagnets have been attracting much current theoretical and experimental interest. The simplest system in one dimension consists of two kinds of spins S and s alternating on a ring with antiferromagnetic exchange coupling between nearest neighbors; a series of such family compounds were extensively synthesized by Verdaguier, Kahn, and their coworkers [17]. The most cited works [18, 19] are the bimetallic chains of general formula $\text{ACu}(\text{pbaOH})(\text{H}_2\text{O})_3 n\text{H}_2\text{O}$ with $\text{A}=\text{Ni}, \text{Co}, \text{Fe}, \text{Mn}$, which have the spin mixtures $(S, s) = (1, 1/2)$, $(S, s) = (3/2, 1/2)$, $(S, s) = (2, 1/2)$, and $(S, s) = (5/2, 1/2)$, respectively. There are also materials with ferromagnetic coupling such as the compound $\text{MnNi}(\text{NO}_2)_4(\text{en})_2$ ($\text{en}=\text{ethylenediamine}$), a chain of which is shown in Fig 2.1. The isotropic Heisenberg antiferromagnetic Hamiltonian for mixed-spin alternating systems can be written as

$$\mathcal{H} = J \sum_j (\mathbf{S}_j \cdot \mathbf{s}_j + \mathbf{s}_j \cdot \mathbf{S}_{j+1}), \quad (2.1.1)$$

where j runs over N unit cells, i.e. the number of sites in the system is $L = 2N$.

All the properties (statics, dynamics, thermodynamics, etc.) of our mixed-spin chains can be obtained if we know the energy spectrum of the many-body Hamiltonian of interest. That is, we have to solve the time-independent Schrödinger equation $\mathcal{H}|\psi_n\rangle = E_n|\psi_n\rangle$ in order to obtain the energy eigenvalues (E_n) and eigenvectors ($|\psi_n\rangle$) of our system. The most basic step at this point is to do this by constructing the full Hamiltonian matrix and

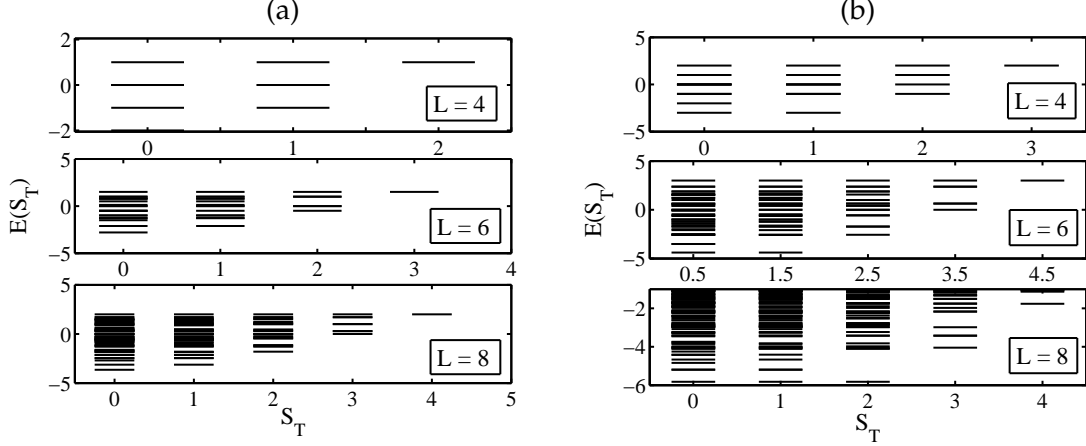


Figure 2.2: Energy spectrum for various system sizes at each sector of total magnetization. (a) Spin-1/2 antiferromagnetic Heisenberg chain. (b) Mixed-spin alternating $(S, s) = (1, 1/2)$ chain. Here only a portion of the energy spectrum is shown for the largest system.

then diagonalize it with an exact procedure. Since this is a very cumbersome task even for small systems, we have to appeal to a numerical diagonalization, which is the core of the next section.

2.2 Exact diagonalization of the Hamiltonian

In order to construct the Hamiltonian matrix, we have to build the matrix representation of the relevant operators in (2.1.1). The dot products can be written as $\mathbf{S}_j \cdot \mathbf{s}_j = \frac{1}{2}(S_j^+ s_j^- + \text{h.c.}) + S_j^z s_j^z$, where h.c. denotes the hermitian conjugate of the former operator. We take the eigenvectors $|S, m_j^S\rangle$ and $|s, m_j^s\rangle$ of the z component of the spin operators as local basis. That is $S_j^z |S, m_j^S\rangle = m_j^S |S, m_j^S\rangle$ and $S_j^+ |S, m_j^S\rangle = \sqrt{S(S+1) - m_j^S(m_j^S + 1)} |S, m_j^S + 1\rangle$, with $S_j^- = (S_j^+)^{\dagger}$ and $\hbar = 1$. Here m_j^S takes the values $-S, -S+1, \dots, S-1, S$. Since the Hamiltonian commutes with the z component of total spin operator (magnetization) $M \equiv \sum_j (S_j^z + s_j^z)$ (the model is invariant under rotations), group theory tells us that its matrix representation is block-diagonal. Then if we take the set of basis vectors $\prod_j |S, m_j^S\rangle \otimes |s, m_j^s\rangle$ with total z component of spin $S_T = \sum_j (m_j^S + m_j^s)$ as the columns of the transformation matrix C , we can diagonalize the Hamiltonian in each S_T sector (or block diagonal): $\mathcal{H}(S_T) = C^{\dagger} \mathcal{H} C$, although once constructed, it can be diagonalized in the full Hilbert space. In Fig. 2.2(a) we show the results for the antiferromagnetic Heisenberg spin-1/2 chain ($S = s$) for several system sizes, and in Fig. 2.2(b) for the simplest mixed-spin system: the $(S, s) = (1, 1/2)$ chain. An observation into these figures reveals that the lowest energy eigenvalue $E_0(S_T)$

for each value of S_T is ordered in a special way. In the ferrimagnetic system we observe that $E_0(S_T + 1) > E_0(S_T)$ for $S_T \geq \mathcal{S}$, and in addition the ground state belongs to $S_T \leq \mathcal{S}$, where $\mathcal{S} = N(S - s)$. The antiferromagnetic ($S = s$) system is when $\mathcal{S} = 0$, and the ground state belongs to total spin zero, i.e., it is a singlet. Marshall [20] was the first to show that the ground state of an antiferromagnet is a singlet. But the natural ordering of the energy levels presented here for the general case of a ferrimagnet is known as the Lieb-Mattis theorem [21], which is valid for a general class of Hamiltonians which need not to be translationally invariant.

With the above described method, we are able to study the thermodynamic properties of small ferrimagnetic chains and judge if the results can well predict the situation for larger systems. We do this in chapter 4; here we are only interested in the ground-state properties. Note from Fig. 2.2(b) that the ground state of mixed-spin chains is highly degenerate, the degeneracy increasing proportional to the system size. To take expectation values of relevant quantities we need to define *the ground state* of the system. One approach for doing this, is to calculate the ground-state density matrix $\rho_0 = \sum_{k=1}^{2\mathcal{S}+1} p_k |\psi_0^k\rangle \langle \psi_0^k|$ which mixes the degenerate *ground states* with equal probabilities p_k . With this, we measure the expectation value of the observable \mathcal{A} as $\langle \mathcal{A} \rangle = \text{Tr}(\rho_0 \mathcal{A})$. The other approach, which we follow in the rest of this thesis, is to define $|\psi_0\rangle$ as the ground state of the perturbed rotationally invariant Hamiltonian $\mathcal{H} - HM$ with $H \rightarrow 0^+$. That is, we add a very small magnetic field H to Eq. (2.1.1) which Zeeman-splits the energy levels and thus breaks the degeneracy of the ground state of \mathcal{H} , leaving $|\psi_0\rangle$ in the sector $S_T = \mathcal{S}$. Therefore we calculate expectation values with the simplest formula $\langle \mathcal{A} \rangle = \langle \psi_0 | \mathcal{A} | \psi_0 \rangle$. This seems to let us equipped for the investigation of definite properties. However, real systems are huge, with sizes of the order of 10^{23} . The worst news is that the Hilbert space dimension $(S \cdot s)^N$ of the systems increases exponentially with size, which makes computer's memories to blow-up if we want to build the Hamiltonian and diagonalize it with an exact procedure. Then we need another strategy to take out the relevant information (low energy physics) from these huge Hilbert spaces. Fortunately the density matrix renormalization group algorithm performs this difficult task for us with a surprising accuracy.

2.3 Density matrix renormalization group (DMRG)

The basic agenda to overcome the system size limitations is to use a set of basis vectors in which the ground state can be represented by only a few base states. In other words, a procedure must be found to identify or construct the important states and discard all others so that the piece of the Hilbert space one operates on remains small. Historically,

the density matrix renormalization group (DMRG) has its roots in the renormalization group approach pioneered by Wilson [22]. The basic idea of this approach is to start with a small system that can be handled exactly as in the previous section. The system size is then increased without increasing the size of the Hilbert space until the desired system size is reached. Increasing the system size without increasing the Hilbert space is typically done in two steps:

- The system size is increased, and therefore the Hilbert space grows at the same time.
- The Hilbert space is truncated to its original size keeping the system size constant.

To characterize such a *renormalization* procedure two basic questions have to be answered: (1) How is the enlargement done? (2) Which criterion do we have to apply in the second step to distinguish between the basis states we will keep from those we will discard? In Wilson's approach, we start with *blocks* (Hilbert space of a given number of sites) of small dimensions. In the first step, two such blocks are linked to form a block which is twice as large. The Hamiltonian of this larger block is then exactly diagonalized and its eigenstates are used as base states. The criterion for keeping states is their energy: only those eigenstates whose energy lies below a certain threshold are kept. The states which are kept represent the new block, which is again linked to an identical block, and the process is iterated. This approach proved to be very effective for the Kondo model investigated by Wilson. However, for other strongly correlated systems, such as the Hubbard and Heisenberg models, it was not successful [23–26]. The main reason for this failure lies in choosing the block eigenstates as the states to be kept. Since the block was not previously connected to the rest of the system (another identical block in the case above) its eigenstates have inappropriate features at the block ends, making them a poor choice as a basis to represent the ground state of a larger system, formed by putting together two (or more) blocks. This problem was pointed out by White and Noack [27] in 1992, who tried to fix it by combining eigenstates from several different blocks under various boundary conditions. However, a better idea was conceived by White the same year, giving rise to the DMRG [28]. The standard algorithm was described by him in some detail in Ref. [29], and a comprehensive review is given by Schollwöck in Ref. [30].

The DMRG algorithm has proved to be a very powerful method for low dimensional interacting systems. Its remarkable accuracy can be seen for example in the $S = 1$ Heisenberg chain: for a system of hundreds of sites a precision of 10^{-10} for the ground state energy can be achieved. Since then it has been applied to a great variety of systems [31] and problems including, among others, spin chains and ladders, fermionic and bosonic systems, disordered models, impurities, molecules, nanoscopic systems and 2D electrons

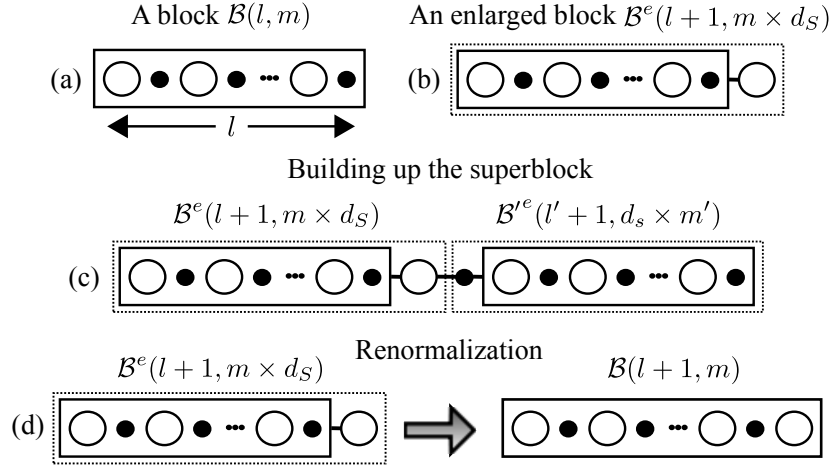


Figure 2.3: Basic steps of a DMRG algorithm. (a) Start with a left block of l sites. (b) Add a site to the right in order to construct the left enlarged block. (c) Construct a right enlarged block and link it to the left one to form a superblock. (d) In the renormalization procedure, an optimal representation for the new left block is obtained without increasing the Hilbert space dimension m .

in high magnetic fields. It has also been improved substantially in several directions like two dimensional (2D) classical systems, stochastic models, inclusion of phonons, quantum chemistry, field theory, finite temperature and the calculation of dynamical properties.

In this section we are going to describe the algorithm for mixed-spin chains which has its own peculiarities. From a computational point of view, a generic block $\mathcal{B}(l, m)$ with l sites and Hilbert space dimension m (see Fig. 2.3(a)) is a portion of memory which contains all the information about the block: the block Hamiltonian (containing only terms involving the sites inside the block), the block basis, and operators needed to link blocks. An operation of enlargement is defined by adding a site to the right (or left) of an existing block as is shown in Fig. 2.3(b). This operation has to be done with care since the alternating structure of the spins must not be destroyed. For example, in the figure we have added a spin- S site to the right of the block shown, which increases the Hilbert space dimension by a factor of $d_S = 2S + 1$. Then a right block enlarged to the left, by adding a spin- s site to an existing block, is linked at the center (and at the ends) with the previous left enlarged block, as shown in Fig. 2.3(c), to form the so-called *superblock*, with open (periodic) boundary conditions.

The DMRG method focus on a single eigenstate of the superblock Hamiltonian (usually the ground state), called the *target state*, which is used to construct the density matrix. The ground state of the superblock Hamiltonian is calculated with a diagonalization routine such as the Lanczos or Davidson algorithm. We then eliminate the states from the basis

of the enlarged block that contribute the least to the ground state of the superblock as is represented in the renormalization procedure of Fig. 2.3(d). To calculate those, the density matrix is used. The concept of the density matrix was developed in statistical mechanics [32] by considering the problem of a system in contact with a much larger environment. The ground state of the universe, i.e. system+environment, is known, and the question is which states of the system contribute the most to this ground state. This is what the density matrix can tell us. One can express the ground state of the universe (the superblock) in a basis that is the tensor product of the basis vectors $|b_i^e\rangle$ of the system (one of the enlarged blocks) and the basis vectors $|b_j'^e\rangle$ of the environment (the other enlarged block),

$$|\psi_0\rangle = \sum_{i=1}^{m \times d_s} \sum_{j=1}^{d_s \times m'} \psi_{ij} |b_i^e\rangle \otimes |b_j'^e\rangle. \quad (2.3.1)$$

Then the (reduced) density matrix of the system is given by tracing $|\psi_0\rangle\langle\psi_0|$ over the degrees of freedom of the environment:

$$\rho_{ii'} = \sum_{j=1}^{d_s \times m'} \psi_{ij} \psi_{i'j}, \quad (2.3.2)$$

which has the same dimension of the Hamiltonian of the system's enlarged block. Since this dimension is small, compared with that of the superblock, we can diagonalize the density matrix exactly. If we denote by $|u_\alpha\rangle$ the eigenstates of ρ ($\alpha = 1, \dots, m \times d_s$) and by w_α its eigenvalues, then w_α is the probability of the system being in the state $|u_\alpha\rangle$ given that the universe is in the state $|\psi_0\rangle$. This is the information we need, to decide which states to keep in a renormalization group approach. That is, we must order the $|u_\alpha\rangle$ by their eigenvalues in a decreasing order and use the first m of those state with largest eigenvalues as the columns of the transformation matrix O to change (truncate) the basis for the enlarged block \mathcal{B}^e , which will then become $\mathcal{B}(l, m)$ as in Fig. 2.3(d). For example, the new block Hamiltonian is related to the old one by the transformation $\mathcal{H}_{\mathcal{B}(l+1, m)} = O^\dagger \mathcal{H}_{\mathcal{B}^e(l+1, m \times d_s)} O$. This change of basis renormalizes the Hilbert space of the system, cutting its size back to m . Constructed in this way, the blocks are being prepared to be connected to another block in the next step, when a new superblock will be formed. It can be shown [30], by a variational calculation, that the *truncation error* of the renormalization procedure is given by the sum of the density matrix eigenvalues of the discarded states $||\psi_0\rangle - |\bar{\psi}_0\rangle|^2 = 1 - \sum_{\alpha=1}^m w_\alpha$, where $|\bar{\psi}_0\rangle$ is the approximate ground state obtained from (2.3.1) when we use the truncated basis $|u\rangle_\alpha$ instead of $|b_i^e\rangle$. The goal is to keep this number as small as possible. In many cases it has been found that this number is roughly proportional to the error in the energy [33], the proportionality factor being of course model dependent; for example in doped fermionic models, we need to keep more states to achieve a good accuracy than in

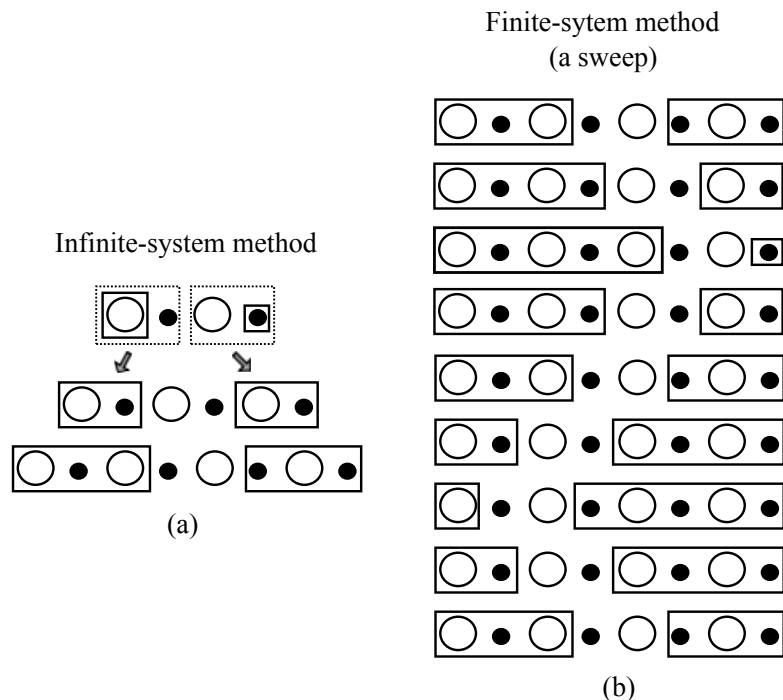


Figure 2.4: Schematic representation of the DMRG algorithm. (a) Enlarge and renormalize until you get the desired system size. (b) Make sweeps to reach a better convergence in a finite system. Here we show a system with $L = 8$ sites.

spin models. To give an idea of acceptable values in spin models, truncation errors are always reported to be less than 10^{-8} . Now we are ready to describe the basic steps of a complete DMRG algorithm for mixed-spin alternating chains.

2.3.1 Infinite-system algorithm

The first implementation by White of the DMRG method was the infinite system algorithm. The goal was to use DMRG's advantage to decouple the system size and the dimension of the Hilbert space in order to calculate ground state energies of large systems, i.e., system sizes that are unreachable for exact diagonalization, eventually converging to the thermodynamic limit. In this algorithm we start with four sites as in Fig. 2.4(a). Then we construct the left and right enlarged blocks¹ and form the superblock. The overall effect is to add to sites in the center of the chain in each step. Having the superblock, we target the ground state with the Lanczos routine and construct the reduced density matrices for the system and the environment *independently*. Then we diagonalize the density matrices,

¹Left and right enlarged block are not mirror images in mixed-spin chains (as is the case in uniform chains), since the systems do not have reflection symmetry with respect to their centers.

and with the m weightest eigenvectors we construct a new truncated basis for the left and right enlarged blocks, which serve as the starting blocks in the next step. Note that m is a parameter in the algorithm; for example, in the $(S, s) = (1, 1/2)$ system where the dimension of the Hilbert space of a unit cell is $d_S \times d_s = 6$; if we choose, say, $m = 20$ then in the first step of the algorithm, the change of basis does not truncate the enlarged block (it is only a rotation). In the second step, the dimension of the Hilbert space of the left enlarged block is $6 \times d_S = 18 < m$ (see Fig. 2.4(a)) and the truncation is not performed either. In the third step, this dimension is $(d_S \times d_s)^2 = 36 > m$, and then from here the truncation does take place, keeping the number of states which describe the block constant. The goal is to grow the chain to a long-enough length, so that the energy and short range correlations around the center have converged. The convergence is checked by keeping track of the difference ΔE_0 between the ground-state energy of the superblocks in two successive steps, which converges to the ground-state energy per unit cell in the thermodynamic limit.

2.3.2 Finite-system algorithm

In the finite-system algorithm the goal is no longer to reach the thermodynamic limit, but rather to restrict ourselves to a finite system size L . At the beginning, until the superblock size reaches the system size, the algorithm is identical to the infinite-system algorithm. When the system size is reached, one applies the steps of infinite-system DMRG, but instead of simultaneous growth of both blocks, growth of one block is accompanied by shrinkage of the other block as shown in Fig. 2.4(b). Reduced basis transformations are carried out only for the growing block. Let the system block grow at the expense of the environment block; to describe it, environment blocks of all sizes must have been stored previously in the infinite-system stage or in previous applications of the finite-system DMRG. When the environment block reaches the minimum size and becomes exact, growth direction is reversed. The environment block now grows at the expense of the system block. A complete shrinkage and growth sequence for both blocks is called a *sweep*. This method usually finds the best approximation to the ground state and convergence is gauged by comparing results from sweep to sweep until they stabilize. In our studied systems, stabilization of the ground-state energy takes place with about four or five sweeps.

We have overcome the difficulty outlined at the end of section 2.2 about the exponentially increasing dimension of the Hilbert space of our many-body systems. Notice that the thermodynamic limit of real chains is well simulated by DMRG when superblocks sizes usually larger than 60 sites are reached. This is signaled by the convergence of the algorithm to definite values of energy per site no matter if we continue increasing the superblock size.

We proceed in the next section to the simplest system in which we can test our developed algorithm: a mixed-spin Ising chain. In this system, the Hamiltonian is already diagonal in the standard basis and the DMRG seems, at first sight, redundant; however it is by no means trivial which are the diagonal entries of such a huge matrix.

2.4 Magnetization plateaux in general anisotropic Ising chains

The quantization of magnetization is one of the most interesting phenomena in the physics of low-dimensional quantum spin systems. Several theoretical and experimental efforts have been made in recent years to understand this fascinating characteristic [34–40]. Oshikawa *et al.* [13] followed an exact treatment for general quantum spin chains suggesting that a magnetization plateau can appear as a result of the quantization of magnetization under the condition

$$S_{\text{unit}} - m = \text{integer} \quad (2.4.1)$$

where S_{unit} is the sum of spins over all the sites in the unit period and m is the magnetization per unit cell. This is only a necessary condition and thus it does not guarantee the existence of the plateau nor specify any mechanism of formation. This condition is still valid for mixed-spin chains with spins S and s ($S > s$). Theoretical investigations into them are the most interesting and important considering the extensive chemical knowledge on ferrimagnetic materials [17–19]. It is well known that these systems have a ground-state spontaneous magnetization which gives a plateau at $m = S - s$, because any elementary excitation increasing the magnetization is of the antiferromagnetic type and these excitations are gapped in ferrimagnets. Since the same plateau appears in the Ising model and in the classical spin (vector) Heisenberg model, Sakai and Yamamoto [41] has called it a *classical plateau*. On the other hand, the condition in Eq. (2.4.1) allows for the appearance of plateaux at higher magnetizations $m = S - s + 1, S - s + 2, \dots, S + s - 1$ for $s > 1/2$. Since these plateaux can never appear in the Ising model or classical Heisenberg model, they called them *quantum plateaux* and gave a valence-bond (or composite picture) representation for some systems [42].

Despite their simplicity, ferrimagnetic Ising systems have attracted a renewed interest recently since they have been proposed as possible models to describe certain types (or class) of molecular-based magnetic materials which are of current experimental interest [43, 44]. Physical mechanisms for the appearance of a multi-plateau structure in the magnetization curve of Ising systems have been searched since Sakai and Yamamoto's findings. When the single-ion anisotropy $D > 0$ is added to the Ising Hamiltonian, Chen *et al.* [45] showed, us-

ing classical Monte Carlo, that for spin- S ($S \geq 1$) chains there appears $2S + 1$ plateaux in the magnetization curve (including the saturated magnetization). This was verified recently using the transfer-matrix technique [46] and formulating the problem on the Bethe lattice [47]. Motivated by this, Aydiner [48] studied the mixed-spin Ising chain $(S, s) = (3/2, 1)$ with single-ion anisotropy obtaining three plateaux which do not obey the $2S + 1$ rule, a situation which was not very clear.

In this section we present our studies of the general alternating mixed-spin (S, s) Ising chain with different single-ion anisotropies on each sublattice of the chain under an applied magnetic field H . Dividing the system into two complementary sublattices α and α' , the Hamiltonian can be written as

$$\mathcal{H} = \sum_{j,\alpha} \left(J \sum_{\delta} S_{j\alpha}^z S_{j\alpha+\delta}^z + D_{\alpha} (S_{j\alpha}^z)^2 - HS_{j\alpha}^z \right), \quad (2.4.2)$$

where j_{α} denotes the j -th ion (j running over N unit cells) in the sublattice $\alpha = \{S, s\}$, δ refers to nearest neighbors, and we consider periodic boundary conditions. Using a molecular-field theory (MFT) we show that the system can exhibit the celebrated $2s + 1$ plateaux at the ground state, including the two classical (initial and saturation) and the quantum ones, which are shown to be generally displayed in the ferrimagnetic Heisenberg chains [42], although in the Ising systems they are explained by purely classical tensor-product states. We compare our results with DMRG calculations (considered exact in these systems) and with the transfer-matrix method, which is a standard technique for investigating thermodynamic properties of Ising systems. We start our analysis giving an overview of this technique applied to the $(S, 1/2)$ chain, which motivates the MFT argument.

2.4.1 Transfer-matrix method

According to our knowledge, this method has not been described in detail for mixed-spin Ising chains. Here, we follow the original procedure developed by Kramers and Wannier [49, 50] which formed the basis for Onsager's solution [51] of the two-dimensional Ising model. Before doing this, we define $G_j \equiv \{m_S, m_s\}_j$ as a particular configuration of spin values inside the unit cell j out of the possible $(2S + 1)(2s + 1)$ ones. With this notation we write $P_{G_{N-1}}$ as the probability of a configuration G_{N-1} regardless of the configurations G_1, G_2, \dots, G_{N-2} . In the thermodynamic limit, this function satisfies the eigenvalue equation

$$\sum_{G_{N-1}} W_{G_N G_{N-1}} P_{G_{N-1}} = \lambda P_{G_N} \quad (2.4.3)$$

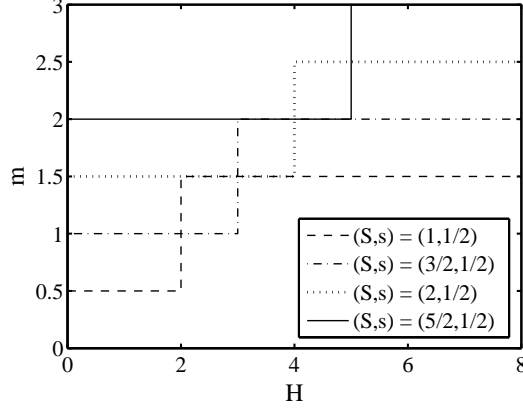


Figure 2.5: The ground state ($T = 0$) magnetization per unit cell as a function of the applied magnetic field, for different mixtures of spin in the unit cell.

where W is the so-called transfer matrix given by

$$W_{GG'} = e^{-\beta[Jm_S(m'_S+m_S)+D_S m_S^2+D_s m_s^2-H(m_S+m_s)]}, \quad (2.4.4)$$

which comes directly from the Boltzmann factor, β being the inverse temperature $1/T$. It can be shown that the partition function can be calculated via the transfer matrix as

$$Z = \text{Tr}(W^N) = \sum_j \lambda_j^N \quad (2.4.5)$$

Then, when $N \rightarrow \infty$ only the largest eigenvalue λ_{\max} dominates in the above sum. Therefore we calculate the ground state magnetization per unit cell as

$$m = \left(\frac{T}{\lambda_{\max}} \frac{\partial \lambda_{\max}}{\partial H} \right)_{\mathcal{F}=0} \quad (2.4.6)$$

where $\mathcal{F} \equiv \{D_S, D_s, H, T\}$ denotes the set of system's parameters. Using this method, we calculate the magnetization curve of the $(S, 1/2)$ system, for some values of $S > 1/2$ as shown in Fig. 2.5. As can be seen, the system only develops the two classical plateaux $m = S - 1/2$ and $m_{\text{sat}} = S + 1/2$ separated by the saturation field $H_{\text{sat}} = 2JS$, independent of the values of D_S and D_s . These results serve as the starting point of our MFT method.

2.4.2 Molecular-field theory

The main idea of this approach is to view each ion as an object which interacts with a magnetic field which is a combination of H and an effective molecular field due to the exchange interaction between the various ions. The magnetic energy at $T = 0$ associated

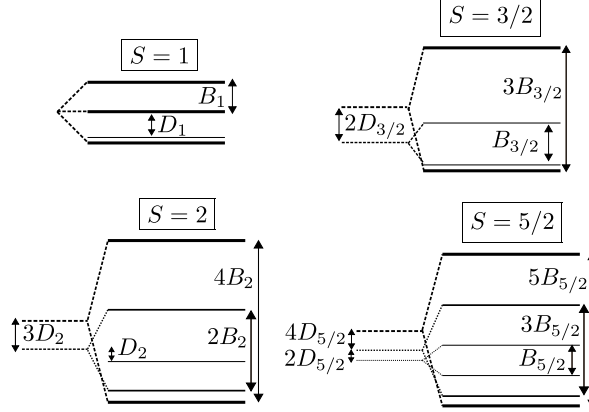


Figure 2.6: Energy levels for different spins S with single-ion anisotropy. The effect of D_S is the zero-field splitting of the energy of the different spin microstates m_S which are represented by solid lines according to their thick and which are further separated by the Zeeman effect produced by B_S .

with this model is

$$\mathcal{H}_{\text{MF}} = \sum_{j,\alpha} (D_\alpha (S_\alpha^z)^2 + B_\alpha S_\alpha^z), \quad (2.4.7)$$

where the magnetic field B_α felt by an α ion is

$$B_\alpha = 2JS_{\alpha'}^z - H, \quad (2.4.8)$$

being proportional to the magnetization of the two neighboring α' ions. It should be noticed that this is just another way to write the Hamiltonian in Eq. (2.4.2) *at zero temperature*, i.e. any approximation has been carried out at all. The only fact that we have used is the translational invariance of the ground state in the infinite-size system which requires spatially modulated spin states with a period equal to the length of the unit cell; that is why the value of $S_{j\alpha}^z$ becomes independent of j and so we have used S_α^z instead. We emphasize that this method is only applicable at zero temperatures. Then, the free energy per α ion can be calculated in the local state $|m_\alpha\rangle$, for which we obtain the two coupled equations

$$U_{m_S} = D_S m_S^2 + (2Jm_S - H) m_S \quad (2.4.9)$$

$$U_{m_s} = D_s m_s^2 + (2Jm_s - H) m_s \quad (2.4.10)$$

We can solve for the two sublattice magnetizations by keeping track of the spin microstates m_S and m_s which *simultaneously* minimize these sublattice energies. We propose doing this diagrammatically [52] by appealing to the energy-level diagrams of some relevant spin quantum numbers as shown in Fig. 2.6. In this figure, we represent the magnitude of spin microstates by solid lines according to their thickness. We remark that the Zeeman splitting of the energy levels increases (decreases), under the applied field, if $|B_\alpha|$ increases (decreases).

$M/2N$	$D_1 \geq 0, D_{3/2} = 0$	$D_1 = 0, D_{3/2} \geq 0$
$1/4$	$\downarrow\uparrow\downarrow\uparrow\downarrow\uparrow\downarrow\uparrow\downarrow\uparrow\downarrow\uparrow\downarrow\uparrow\downarrow\uparrow\downarrow\uparrow\downarrow\uparrow$	$\uparrow\downarrow\uparrow\downarrow\uparrow\downarrow\uparrow\downarrow\uparrow\downarrow\uparrow\downarrow\uparrow\downarrow\uparrow\downarrow\uparrow\downarrow\uparrow$ $\uparrow\uparrow\uparrow\uparrow\uparrow\uparrow\uparrow\uparrow\uparrow\uparrow\uparrow\uparrow\uparrow\uparrow\uparrow\uparrow\uparrow\uparrow$
$3/4$	$-\uparrow-\uparrow-\uparrow\cdots-\uparrow-\uparrow-\uparrow$	$\uparrow\uparrow\uparrow\uparrow\uparrow\uparrow\uparrow\uparrow\uparrow\uparrow\uparrow\uparrow\uparrow\uparrow\uparrow\uparrow\uparrow\uparrow$
$5/4$	$\uparrow\uparrow\uparrow\uparrow\uparrow\uparrow\uparrow\uparrow\uparrow\uparrow\uparrow\uparrow\uparrow\uparrow\uparrow\uparrow\uparrow\uparrow$	$\uparrow\uparrow\uparrow\uparrow\uparrow\uparrow\uparrow\uparrow\uparrow\uparrow\uparrow\uparrow\uparrow\uparrow\uparrow\uparrow\uparrow\uparrow$

Table 2.1: Representation of the magnetization profiles of the system in the various translationally invariant phases. The scaled arrows represent $m_1 = \pm 1$ and $m_{3/2} = \pm 1/2, 3/2$ spin microstates, and the small horizontal line represents the $m_1 = 0$ microstate. In the case $D_1 = 0, D_{3/2} \geq 0$ two different mechanisms generate the plateau at $1/4$. The transition region is $J/2 < D_{3/2} < J$.

In order to describe the magnetization process we need to start from definite values of the sublattice spin microstates, which we call the *initial state* in the following. In the ground state of the system ($\mathcal{F} = 0$) we see from Eqs. (2.4.9) and (2.4.10) that the product $m_S m_s$ must be a minimum. This is accomplished, as we expected, by the two Néel-ordered states $\psi_1 = |S, -s\rangle^{\otimes N}$ and $\psi_2 = | -S, s\rangle^{\otimes N}$, where “up” has been defined as the positive direction along the z axis, i.e. the direction of the applied magnetic field H . Since the system chooses only one of these two states for the magnetization process, as will be seen in the following, we say that the ground state spontaneously breaks the up-down symmetry. As a rule we find that the chosen initial state is that which has the greatest of the spin microstates $\max(m_S, m_s)$ pointing upwards. When $\mathcal{F} = 0$, this state coincides with ψ_1 : it seems as if the system “knew” that a magnetic field is going to be applied eventually and then it gets ready for it (it is less favorable for this field to turn the greatest spin in the unit cell).

Magnetization process of the $(S, \frac{1}{2})$ system

When $s = 1/2$ (and by definition $D_s = 0$) we find, as supported by the transfer matrix results, that the system chooses the ψ_1 initial state regardless of the value of S . Then, a classical magnetization plateau appears at $m = S - 1/2$. When we increase the applied magnetic field H , the splitting of the spin- $1/2$ energy levels decreases and those of the spin- S increases (and hence stabilizing the local state $|m_S = S\rangle$) until we reach the saturation field: $B_{1/2} = 0 \Rightarrow H_{\text{sat}} = 2JS$, from which a transition to the saturated state $|S, \frac{1}{2}\rangle^{\otimes N}$ occurs. Henceforward the splitting of the spin- $1/2$ energy levels increases and the systems displays a magnetization plateau at the saturation value $m_{\text{sat}} = S + 1/2$. This holds irrespective of the value of D_S since the Zeeman splitting of the spin- S energy levels al-

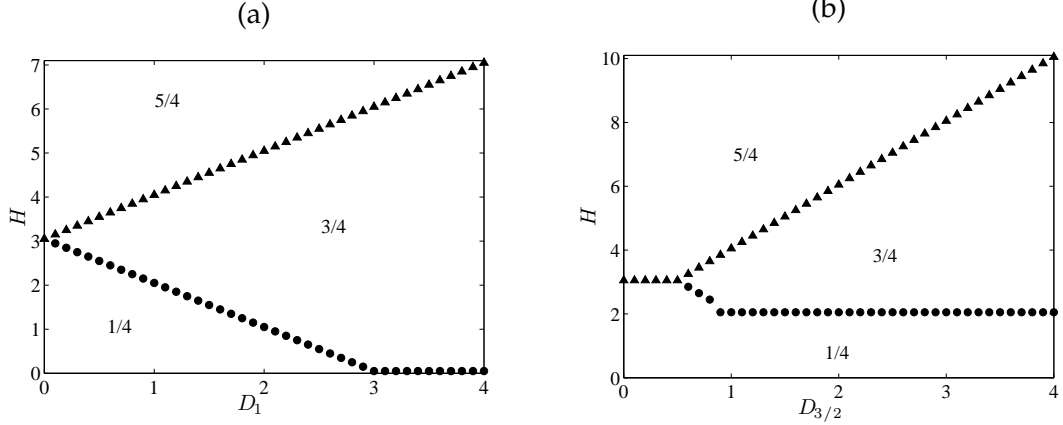


Figure 2.7: Quantum phase diagram for the mixed $(S, s) = (3/2, 1)$ Ising chain. (a) For the case $D_1 \geq 0$, $D_{3/2} = 0$. (b) For the case $D_1 = 0$, $D_{3/2} \geq 0$. The numbers in each region correspond to the total magnetization per site.

ways increases in the magnetization process. Then, our method is able to reproduce the transfer-matrix results shown in Fig. 2.5 under a more intuitive basis. We now concentrate in more elaborate cases which include spin mixtures both greater than $1/2$ and have a simple fascinating physics behind.

Magnetization process of the $(S, s) = (\frac{3}{2}, 1)$ system

We studied this system in Ref. [52] for the two cases of interest $D_\alpha \neq 0$ with $D_{\alpha'} = 0$. Choosing ψ_1 as the initial state, a classical magnetization plateau is displayed at the value $m = 1/2$. When D_1 is turned on (keeping $D_{3/2} = 0$) a quantum magnetization plateau at the value $m = 3/2$ appears when the applied field overcomes the critical field given by $H_c = 3J - D_1$, from which the system undergoes a transition to the state $|\frac{3}{2}, 0\rangle^{\otimes N}$. Then the saturated state $|\frac{3}{2}, 1\rangle^{\otimes N}$ appears above the saturation field $H_{\text{sat}} = 3J + D_1$ giving a plateau at the value $m_{\text{sat}} = 5/2$. When $D_{3/2}$ is turned on (keeping $D_1 = 0$) the same plateaux are found but now there appears two different mechanisms for the plateau at $m = 1/2$: the small- D phase mechanism with ψ_1 as the initial state and $H_{\text{sat}} = 3J$ (the quantum plateau does not appear) and the large- D phase mechanism ($D_{3/2} > J$), with the initial state given by $|\frac{1}{2}, 1\rangle^{\otimes N}$, a critical field $H_c = 2J$ and a saturation field $H_{\text{sat}} = 2(J + D_{3/2})$. These phases are represented in Table 2.1. The results were compared with DMRG calculations in a chain of 200 sites, choosing up to 80 states during 10 sweeps, which gave a truncation error of machine precision. As can be seen in the phase diagrams in Fig. 2.7, the critical fields are reproduced exactly. This stimulates us to investigate the ground state magnetization curve of the $(S, s) = (\frac{5}{2}, 2)$ system in a more general setting.

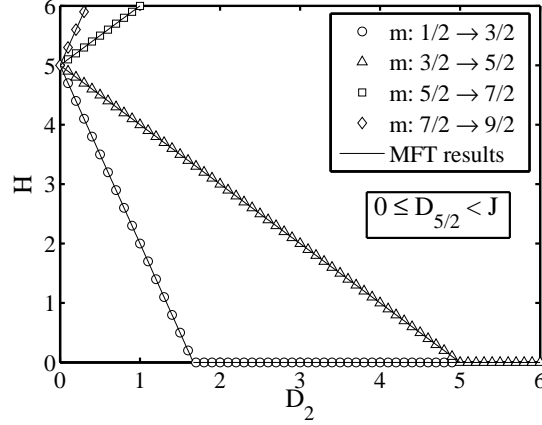


Figure 2.8: Quantum phase diagram indicating the critical fields for the specified transitions in the ranges of D_2 and $D_{5/2}$ shown. The symbols represent DMRG calculations in a ring of 100 sites and the solid line is the prediction of our MFT results (see the text).

Magnetization process of the $(S, s) = (\frac{5}{2}, 2)$ system

Choosing ψ_1 as the initial state, a classical magnetization plateau appears at the value $m = 1/2$. When the applied field H is increased, the Zeeman splitting of the spin-5/2 energy levels increases (therefore stabilizing the local state $|m_{5/2} = \frac{5}{2}\rangle$) and that of the spin-2 decreases. When the critical field $H_{c_1} = 5J - 3D_2$ is reached, a transition to the state $|\frac{5}{2}, -1\rangle^{\otimes N}$ occurs, giving a quantum plateau at $m = 3/2$. If we continue increasing the field, a transition to the state $|\frac{5}{2}, 0\rangle^{\otimes N}$ is produced above the critical field $H_{c_2} = 5J - D_2$ giving a quantum plateau at $m = 5/2$. There is a field value $H_0 = 5J$ at which the Zeeman splitting is zero. Then, at $H_{c_3} = H_0 + D_2$ the system undergoes a transition to the state $|\frac{5}{2}, 1\rangle^{\otimes N}$ in which a quantum plateau at $m = 7/2$ appears. Finally, the magnetization of the system saturates above the saturation field $H_{\text{sat}} = 5J + 3D_2$ giving the classical plateau at $m_{\text{sat}} = 9/2$. We compare these findings with DMRG, using a ring of 100 sites, as can be seen in Fig. 2.8. One may ask about the range of values of $D_{5/2}$ for which the initial state ψ_1 of the described magnetization process is the ground state of the system. This can be answered easily if we take a look at Fig 2.9. When $0 \leq D_{5/2} < J$, the system chooses ψ_1 as the ground state as shown in Fig 2.9(a). Increasing the anisotropy from $D_{5/2} \geq J$, there is a transition to the state $|-\frac{3}{2}, 2\rangle^{\otimes N}$ as shown in Figs. 2.9(b) and 2.9(c) with initial magnetization plateau at the classical value $m = 1/2$. For $D_{5/2} \geq 2J$, a transition to the state $|-\frac{1}{2}, 2\rangle^{\otimes N}$ occurs (see Fig. 2.9(d)) giving an initial quantum plateau at $m = 3/2$. If we increase H from these states, a different magnetization process takes place which is analyzed in the same way as before but no new magnetization plateaux appear.

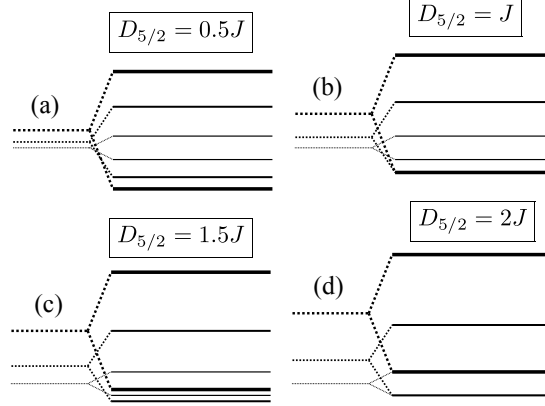


Figure 2.9: Energy levels at $H = 0$ of the spin-5/2 ions when $D_{5/2}$ is increased, showing their ground state as the lowest level. (a) The state $|m_{5/2} = \frac{5}{2}\rangle$ has the lowest energy. (b) The state $|m_{5/2} = -\frac{3}{2}\rangle$ is now the local ground state. (c) The same state as in (b) remains. (d) The state $|m_{5/2} = -\frac{1}{2}\rangle$ is now the most favorable.

Counting the magnetization plateaux in general (S, s) systems

We can generalize the procedure described above for general alternating Ising chains with spins (S, s) and single-ion anisotropy. Starting from ψ_1 at $H = 0$ the system exhibits the classical initial plateau at $m = S - s$. When H is increased, the Zeeman splitting of the energy levels of spin- S ions increases and that of the spin- s ions decreases as shown in Fig. 2.10. When the critical field $H_{c_1} = 2JS - (2s - 1)D_s$ is reached, there is a transition to the state $|S, -s + 1\rangle^{\otimes N}$ and a quantum magnetization plateau appears at $m = S - s + 1$. It is easy to realize from this the subsequent behavior. If we continue increasing the applied field, the system undergoes multiple transitions through the sequence of tensor-product states $|S, -s + 1 + j\rangle^{\otimes N}$ (with j incrementing in unit steps from 1 to $2s - 1$) each time a crossing of levels in the diagram in Fig 2.10 occurs, that is, when the critical fields $H_{c_{j+1}} = 2JS - [2(s + j) - 1]D_s$ are reached. Then, the ground-state (step-like) magnetization curve consists of a series of $2s + 1$ plateaux at the values $m = S - s, S - s + 1, \dots, S + s$: the two classical plateaux and *all* the quantum plateaux allowed by the condition in Eq. (2.4.1). As in the former case we may ask about the range of values of D_s for which ψ_1 is the initial state of the magnetization process. This is always the case for $D_s = 0$. When we increase D_s keeping $H = 0$, the first crossing of energy levels can be found at $D_s = Js/(S - 1/2)$. When D_s exceeds this value, no new plateaux are expected to occur. The range of D_s for which we have this full number of plateaux can be found by making $H_{c_1} = 0$ in the above expressions for the critical fields: we find $D_s < JS/(s - 1/2)$.

With this, we have showed that for the range of single-ion anisotropy parameters $0 \leq D_s < Js/(S - 1/2)$ and $0 \leq D_s < JS/(s - 1/2)$, the system exhibits $2s + 1$ plateaux in the

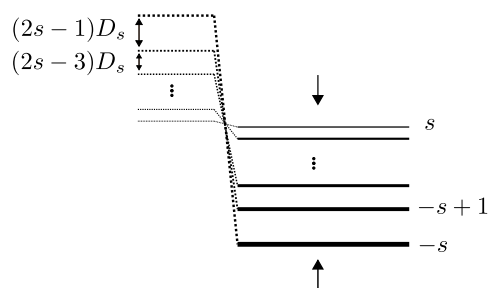


Figure 2.10: Energy levels of spin- s ions with single-ion anisotropy in the ground state ψ_1 . As the applied magnetic field H is increased the Zeeman splitting of these levels decreases (indicated with one-head arrows). We show only one of the two microstate for some values of $|m_s|$.

ground-state magnetization curve separated by the indicated critical fields. This provides a similar rule as that known for spin- S ($S \geq 1$) Ising chains with single-ion anisotropy, for which $2S + 1$ plateaux appear.

2.5 Interacting spin-wave dispersions of Heisenberg chains

As we have said before, Heisenberg ferrimagnetic spin systems have received considerable attention recently. Many theoretical studies have been carried out to calculate the ground-state properties and the low-lying excited states of the alternating (S, s) ($S > s$) chains [18, 53–71]. All of this research was stimulated by an accumulated chemical knowledge on ferrimagnetic materials [17, 19, 72–74]. Kahn *et al.* [75] succeeded in synthesizing a series of bimetallic chain compounds such as $MM'(\text{pba})(\text{H}_2\text{O})_3 \cdot 2\text{H}_2\text{O}$ [pba=1,3-propylenebis(oxamato)= $\text{C}_7\text{H}_6\text{N}_2\text{O}_6$] and also the family $MM'(\text{pbaOH})(\text{H}_2\text{O})_3$ [pbaOH=2-hydroxy-1,3-propylenebis(oxamato)= $\text{C}_7\text{H}_6\text{N}_2\text{O}_7$], where the alternating magnetic ions M and M' are flexible variables and, therefore, the low-dimensional ferrimagnetic behavior could systematically be observed. Caneschi *et al.* [76, 77] synthesized another series of mixed-spin chain compounds of general formula $M(\text{hfac})_2\text{NITR}$, where metal ion complexes $M(\text{hfac})$ with hfac=hexafluoroacetylacetonate are bridged by nitronyl nitroxide radicals NITR. There also exist purely organic molecule-based ferrimagnets [78, 79], where sufficiently small magnetic anisotropy, whether of exchange-coupling type or of crystal-field type, is advantageous for observation of essential quantum mixed-spin phenomena.

The characteristic properties of the elementary excitations of mixed-spin chains have been shown to be the result of a ferromagnetic-antiferromagnetic crossover, due to the competition between excitations to a gapless ferromagnetic and a gapped antiferromagnetic branch in the energy spectrum. The spin-wave theory has been a cornerstone for the es-

tablishment of these facts and, in some instances, has demonstrated a high efficiency. For example, Ivanov [80] showed that for the cases $(S, s) = (1, 1/2)$, $(3/2, 1)$, and $(3/2, 1/2)$, the estimates for the ground-state energy and sublattice magnetizations differ less than 0.03% for the energy and 0.2% for the sublattice magnetizations from DMRG. When the crystal-field (or single-ion) anisotropy term D is taken into account in the spin-wave theory (a term almost always present in real situations, such as in the Ni ($S = 1$) environment of the $(S, s) = (1, 1/2)$ mixed-spin chain $\text{NiCu}(\text{pba})(\text{D}_2\text{O})_32\text{D}_2\text{O}$ [81]), Zhou and Kawazoe [82] introduced a new spin-Bose transformation for arbitrary *uniform* (not mixed) spin-number systems and configurations, arguing that the frequently used Holstein-Primakoff (HP) spin-Bose transformation for the spin-wave approach *completely fails* for systems with easy-plane anisotropy ($D > 0$) and *sometimes fails* for those with easy-axis anisotropy ($D < 0$). Since we can encounter examples (see Ref. [66] and references therein) in which the HP-based spin-wave theory works very well for mixed-spin alternating chains, it remains to be shown whether the inclusion of the D term can reflect the real situation at all.

In this section we investigate the suitability of the HP-based spin-wave theory for mixed-spin Heisenberg chains with crystal-field anisotropy. In order to make a quantitative judgement, we treat the spin-wave expansions up to second order in the particle-number operators in the Fock space which has been proved to work much better than the usual linear expansion, which overestimates the role of the zero-point spin fluctuations. The Hamiltonian of our mixed-spin alternating Heisenberg chain with crystal-field anisotropy D then reads:

$$\mathcal{H} = J \sum_{j=1}^N \left(\mathbf{S}_j \cdot \mathbf{s}_j + \mathbf{s}_j \cdot \mathbf{S}_{j+1} + D(S_j^z)^2 \right), \quad (2.5.1)$$

where \mathbf{S}_j and \mathbf{s}_j are spin operators at the sites with spins S and s respectively, and j runs over N unit cells. Note that the crystal-field term has been put only on the spin- S sites (highest spin numbers), which is more common in real materials. For our analysis, we consider the systems with $(S, s) = (1, 1/2)$, $(3/2, 1/2)$, $(3/2, 1)$, and $(2, 1)$, and compare our results with DMRG. Our primary conclusion is that for the easy-plane anisotropy case the HP-based spin-wave theory indeed fails but for the easy-axis anisotropy case it demonstrates a surprising efficiency.

2.5.1 Second-order spin-wave theory

Assuming the Néel-ordered ferrimagnetic ground state with total magnetization $M = (S - s)N$ we define the bosonic operators for the spin deviation in each sublattice through the

HP transformation [83]

$$\begin{aligned} S_j^+ &= \sqrt{2S - a_j^\dagger a_j} a_j, & S_j^z &= S - a_j^\dagger a_j, \\ s_j^+ &= b_j^\dagger \sqrt{2s - b_j^\dagger b_j}, & s_j^z &= -s + b_j^\dagger b_j. \end{aligned} \quad (2.5.2)$$

Then we can expand the Hamiltonian (2.5.1) as

$$\mathcal{H} = E_{\text{class}} + \mathcal{H}_0 + \mathcal{H}_1 + O(S^{-1}), \quad (2.5.3)$$

where $E_{\text{class}} = (DS^2 - 2Ss)JN$ is the classical ground-state energy, \mathcal{H}_0 gives the *free* spin waves, and \mathcal{H}_1 describes two-body interactions between them, which are respectively, the $O(S^2)$, $O(S^1)$, and $O(S^0)$ terms of the expansion. We follow the perturbational treatment of \mathcal{H}_1 to \mathcal{H}_0 described in Ref. [66]. That is, after a Fourier transformation followed by a Bogoliubov change of coordinates, we diagonalize \mathcal{H}_0 as

$$\mathcal{H}_0 = E_0 + J \sum_k \left(\omega_k^- \alpha_k^\dagger \alpha_k + \omega_k^+ \beta_k^\dagger \beta_k \right), \quad (2.5.4)$$

where $E_0 = J \sum_k [\omega_k - (S + s - \bar{D})]$ (with $\bar{D} \equiv DS$) is the $O(S^1)$ quantum correction to the ground-state energy, and α_k^\dagger and β_k^\dagger are the creation operators of the ferromagnetic and antiferromagnetic spin waves of momentum k whose dispersion relations are given by

$$\omega_k^\pm = \omega_k \pm (S - s + \bar{D}), \quad \text{with} \quad \omega_k = \sqrt{(S + s - \bar{D})^2 - 4Ss \cos^2(k/2)}. \quad (2.5.5)$$

Now we pick up the relevant contributions to the dispersions, as well as to the ground-state energy, from \mathcal{H}_1 . Using the Wick theorem, \mathcal{H}_1 is rewritten as

$$\mathcal{H}_1 = E_1 + J \sum_k \left(\delta \omega_k^- \alpha_k^\dagger \alpha_k + \delta \omega_k^+ \beta_k^\dagger \beta_k \right) + H_{\text{irrel}} + H_{\text{resid}}, \quad (2.5.6)$$

where H_{irrel} contains irrelevant terms such as $\alpha_k \beta_k$ and H_{resid} contains residual two-body interactions, both of which are neglected in the following. The $O(S^0)$ correction to the ground-state energy and those to the dispersion relations are given by

$$\frac{E_1}{2JN} = \frac{\bar{D}}{S} \Gamma_1 (\Gamma_1 + 1/2) - (\Gamma_1^2 + \Gamma_2^2) + \left(\sqrt{S/s} + \sqrt{s/S} \right) \Gamma_1 \Gamma_2, \quad (2.5.7)$$

and

$$\begin{aligned} \delta \omega_k^\pm &= \frac{\bar{D}}{S} \left(\frac{S + s - \bar{D}}{\omega_k} \mp 1 \right) (2\Gamma_1 + 1/2) + \frac{2\Gamma_1}{\omega_k} [\bar{D} - (S + s) \sin^2(k/2)] \\ &+ \frac{\Gamma_2}{\sqrt{Ss}} \left[\omega_k \pm (S - s) + \frac{\bar{D}}{\omega_k} (S + s - \bar{D}) \right], \end{aligned} \quad (2.5.8)$$

where the key constants Γ_1 and Γ_2 are evaluated in the thermodynamic limit as

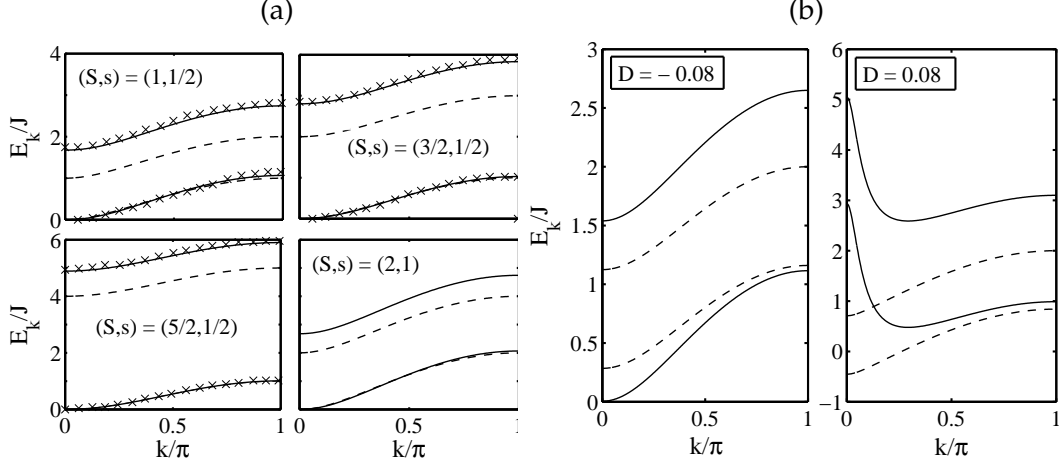


Figure 2.11: Noninteracting (dashed lines) and interacting (solid lines) spin-wave calculations of the dispersion relations for the specified mixed-spin alternating systems (a) with $D = 0$. Corresponding quantum Monte Carlo calculations (x) are also shown for comparison. (b) For the mixed $(S, s) = (1, 1/2)$ alternating spin chain with $D = -0.08$ (left panel) and $D = 0.08$ (right panel). The situation for other spin mixtures is similar.

$$\Gamma_1 = \frac{1}{2\pi} \int_0^\pi \left(\frac{S + s - \bar{D}}{\omega_k} - 1 \right) dk, \quad (2.5.9)$$

$$\Gamma_2 = \frac{1}{\pi} \int_0^\pi \frac{\sqrt{Ss} \cos^2(k/2)}{\omega_k} dk. \quad (2.5.10)$$

Then, up to order $O(S^0)$, we obtain the Hamiltonian

$$\mathcal{H} = E_g + J \sum_k \left(\tilde{\omega}_k^- \alpha_k^\dagger \alpha_k + \tilde{\omega}_k^+ \beta_k^\dagger \beta_k \right), \quad (2.5.11)$$

with $\tilde{\omega}_k^\pm = \omega_k^\pm + \delta\omega_k^\pm$ and $E_g = E_{\text{class}} + E_0 + E_1$. In Fig. 2.11(a) we show the dispersion relations ω_k^\pm and $\tilde{\omega}_k^\pm$ of some spin mixtures for the case $D = 0$. We correctly reproduce the results of Ref. [84], where the interacting spin-wave calculations are in excellent agreement with the numerical findings obtained with quantum Monte Carlo calculations (crosses in Fig. 2.11(a)). We observe, as expected, two distinct branches of spin-wave excitations: the gapless one, which reduces the ground-state magnetization, is of the ferromagnetic type, showing a quadratic dispersion at small momenta; the gapped one is of the antiferromagnetic type, enhancing the ground-state magnetization. Note that the $O(S^0)$ quantum correction has an important effect on the antiferromagnetic spin waves, whereas the ferromagnetic ones appear almost free from two-body interactions. In Fig. 2.11(b) we show the dispersion relations of the mixed $(S, s) = (1, 1/2)$ alternating spin chain for two values of D in the easy-axis ($D < 0$) and easy-plane ($D > 0$) regimes. We note that the $O(S^1)$ (linear) spin-wave description in the easy-plane case breakdowns since the ground-state

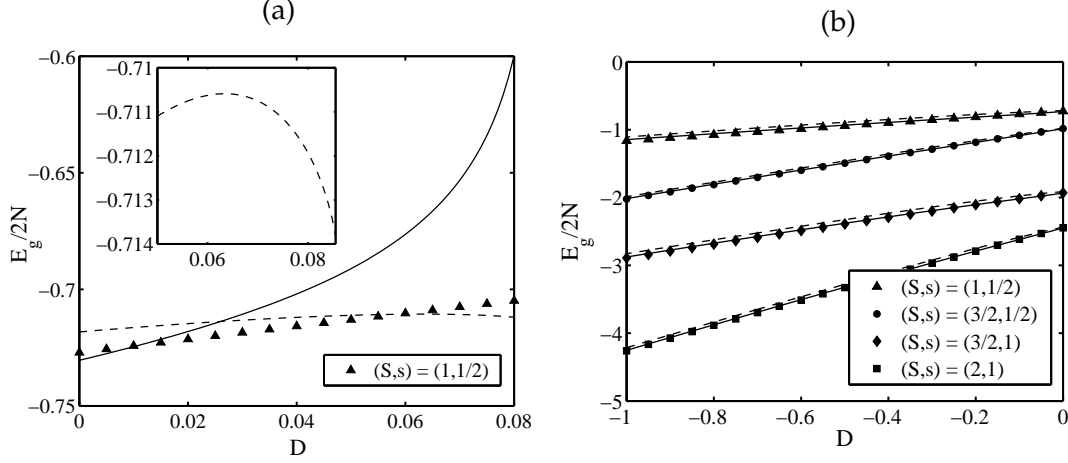


Figure 2.12: Ground-state energy for the specified mixed-spin systems. The solid (dashed) lines are calculations with the (non)interacting spin-wave theory. (a) Mixed $(S, s) = (1, 1/2)$ spin systems in the easy-plane regime; the situation being similar for other spin mixtures. (b) Easy-axis regime. A very good agreement with DMRG is obtained in this case.

energy is no longer the lowest energy of the system. In fact, there is a positive value of $D = D^* \equiv (\sqrt{S} - \sqrt{s})^2/2S$ above which the dispersion relations become imaginary. For the $(S, s) = (1, 1/2)$ system, this value is $D^* \simeq 0.0858$. We shall see in the next section that the ground-state energy seems to diverge at this point. For the other systems, the situation is very similar.

With this spin-wave method, it is also possible to obtain estimates for the sublattice magnetizations. Here the formulas do not distinguish between interacting and noninteracting cases. Only the ground-state energy is vulnerable to the order of the expansion. With the notation $S^z \equiv N^{-1} \sum_j S_j^z$ and $s^z \equiv N^{-1} \sum_j s_j^z$ for sublattice magnetizations, we find

$$\langle S^z \rangle = S - \Gamma_1, \quad \langle s^z \rangle = -(s - \Gamma_1), \quad (2.5.12)$$

which clearly shows the quantum “spin reduction” present in quantum spin chains, which has already been predicted with the spin-wave theory [85]. Note that when $S = s$, Γ_1 is divergent at $k = 0$, a problem known as the infrared-diverging magnetization. Ferrimagnets, however get rid of this difficulty. Now we proceed to compare the obtained ground-state energy and sublattice magnetizations with the results obtained with the DMRG algorithm.

2.5.2 Numerical analysis with DMRG

We consider chains of 100 sites with open boundary conditions and $J = 1$. The number of block states chosen to represent the renormalized Hilbert space was allowed to

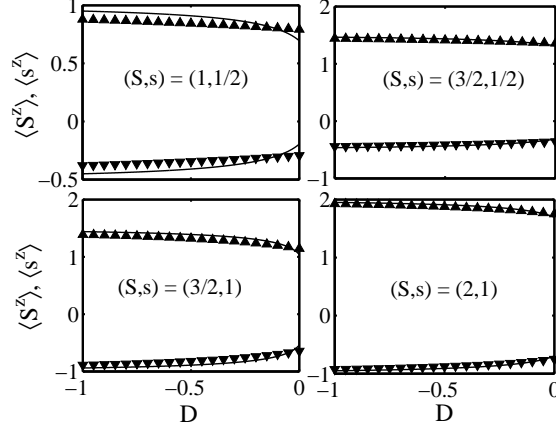


Figure 2.13: Sublattice magnetizations for the specified mixed-spin systems in the easy-axis regime. The solid line is the spin-wave estimate.

vary with the condition of keeping a truncation error less than 10^{-8} . In Fig. 2.12(a) we show the ground-state energy in the easy-plane regime for the $(S, s) = (1, 1/2)$ system. The results for other spin mixtures are similar. Here we observe that the interacting spin-wave description fails to describe the ground-state energy of the system as was expected from the results of Fig. 2.11(b). As can be seen, when $D \rightarrow D^*$ the ground-state energy seems to diverge. Therefore we conclude that the spin-wave theory *fails* for ferromagnetic chains with easy-plane anisotropy. The easy-axis regime is very different as can be noticed from Fig. 2.12(b) for the ground-state energy and in Fig. 2.13 for the sublattice magnetizations. In this regime there is a very good agreement with the DMRG results. For example, for the $(S, s) = (3/2, 1/2)$ system, the discrepancy factor defined as $R = \sum[(E_g)_{\text{DMRG}} - (E_g)_{\text{SWT}}]^2 / \sum[(E_g)_{\text{DMRG}}]^2$ is equal to 6.1×10^{-6} . If we calculate the discrepancy factor using the data of the sublattice magnetizations for the same system we obtain a value of 2.0×10^{-2} , which is reasonable because the DMRG gives a more precise description of the ground-state energy of the system than of its ground-state vector, which is used to take expectation values. We roughly see from the figures that the success of the spin-wave theory in the easy-axis anisotropy regime is enhanced when the spin quantum numbers S and s are both integers or both half-odd integers, but we can not draw a general conclusion from this.

With this, we have shown that the HP-based interacting spin wave theory can be applied, with all the confidence, to mixed-spin Heisenberg chains with single-ion anisotropy provided that the system is in the easy-axis regime. This is an important conclusion since almost all theoretical attempts to study the low-temperature properties of mixed-spin chains (with $D = 0$) have been done with this approach [66], and the inclusion of a D term is often taken into account in experimental research, so that it should have to be included in this

type of calculations. In the next section we jump to the description of quantum critical points in mixed-spin chains concepts from quantum information such as entanglement.

2.6 Entanglement and quantum phase transitions

If two systems interacted in the past it is, in general, not possible to assign a single state vector to either of the two subsystems [86].

This is also known as the principle of non-separability and expresses much of what entanglement is about. First recognized by Einstein, Podolski and Rosen [87] and by Schrödinger [88], it is one of the most astonishing features of quantum mechanics. The main problem of entanglement theory is that we do not have a fully understanding of what entanglement is. More precisely, we only know its mathematical definition and its manifestation [89–91].

Entanglement appears as the consequence of the combination of two of the quantum postulates:

$$\boxed{\begin{array}{l} \text{The state of a quantum system} \\ \text{is described by a vector in a} \\ \text{complex Hilbert space} \end{array}} + \boxed{\begin{array}{l} \text{The Hilbert space of a composite} \\ \text{system is the tensor product of the} \\ \text{two local spaces} \end{array}} = \boxed{\begin{array}{l} \text{There exist superposition of pure} \\ \text{states that can not be written as} \\ \text{the tensor product of pure states} \\ \text{in each local space} \end{array}}$$

Then, the investigation of entanglement in a given quantum state reduces to whether it is separable or not. That is, a state is entangled *if and only if* it is not separable. After playing a significant role in the foundations of the quantum formalism, entanglement has been recently rediscovered, within the quantum information science, as a new physical resource with potential commercial applications such as quantum cryptography, better frequency standards or quantum-enhanced positioning, and clock synchronization. Moreover, the ability to generate entangled states is one of the basic requirements for building quantum computers [92].

In the last few years, there has been a huge interest in deciphering the connection between the theory of critical phenomena in condensed matter systems with quantum information, by exploring the entangling resources of a system close to its quantum critical point [93]. Traditionally many-body systems have been studied by looking for example at their response to external perturbations, various order parameters and excitation spectrum. The study of the ground state of many-body systems with methods developed in quantum information may unveil new properties. At the same time, experience built up over the years in condensed matter is helping in finding new protocols for quantum computation

and communication: A quantum computer is a many-body system where differently from “traditional ones”, the Hamiltonian can be controlled and manipulated [94]. Let us then see how entanglement properties give key information on the critical behavior of some mixed-spin chain systems.

2.6.1 Mixed-spin Heisenberg chain with single-ion anisotropy

In recent years, many efforts have been made to comprehend the relation between entanglement and quantum phase transitions [93, 95–97]. An obvious advantage in determining quantum critical points using measures of entanglement is that we do not require *a priori* knowledge of the order parameter and the symmetries of the system. Most of the systems which have been studied previously are Heisenberg spin-1/2 systems as there exists a good measure of entanglement for a two-spin system, the concurrence [98], which is applicable to an arbitrary state of two qubits. On the other hand, the entanglement in mixed-spin or higher spin systems are not well-studied due to the lack of good operational measures of entanglement. There have been several initial studies along this direction [99, 100], however these works are restricted to the case of only two-particle systems. For the case of general bipartite systems, a non-entangled state has necessarily a positive partial transpose according to the Peres-Horodecki criterion [101, 102]. Fortunately, due to the SU(2) symmetry of the Heisenberg Hamiltonian, it can be shown [99] that a positive partial transpose is also sufficient for a separate state in the case of spin mixtures of the type $(S, 1/2)$. This allows us to investigate entanglement features in this kind of mixed-spin systems, such as the well-known family of bimetallic chains [18, 19] of general formula $ACu(pbaOH)(H_2O)_3nH_2O$ with $A = Ni, Co, Fe, Mn$ in which the largest spin varies from $S = 1$ to $5/2$.

There are very few works on the study of entanglement in quantum mixed-spin chain models. Li *et al.* have considered [103] a polymerized antiferromagnetic mixed-spin chain in which the ground-state entanglement transition found is closely related to the valence-bond-solid phase transition. Sun *et al.* have studied the entanglement properties and its relation with quantum phase transitions in the isotropic [104] and the XXZ anisotropic [105, 106] $(1, 1/2)$ spin chain, respectively. The thermal entanglement has also been studied in more general spin mixtures such as the $(S, 1/2)$ and the $(S, 1)$ systems [107–109]; here the main interest is focused on the characteristic temperature for an entangled thermal state. The effects of external magnetic fields on the entanglement properties has also called the attention recently [110–112], since this plays an important role in improving the characteristic temperature and enlarging the region of entanglement in the system. To the best

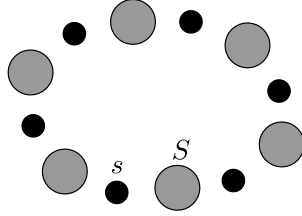


Figure 2.14: Schematic representation of the alternating mixed-spin (S, s) chain arranged on a ring.

of our knowledge, the entanglement and its relation with quantum phase transitions have never been investigated in mixed-spin chains with single-ion anisotropy. This anisotropy (also known as magnetocrystalline or crystal-field anisotropy) is very realistic from an experimental point of view and can be increased locally by adding non-magnetic defects in the system [113]. As an example of this anisotropy in mixed-spin chain compounds, the chain $\text{NiCu}(\text{pba})(\text{D}_2\text{O})_32\text{D}_2\text{O}$, which has the spin mixture $(1, 1/2)$, would possibly have the single-ion anisotropy on the Ni ($S = 1$) ion [81].

Motivated by the above facts, in this section we investigate the mixed-spin $(S, s) = (1, 1/2)$ Heisenberg system with single-ion anisotropy D . We choose this particular spin mixture just for computational convenience, but we have shown, using the interacting spin-wave theory together with density matrix renormalization group calculations, that the ground state properties for general S and s are qualitatively similar [114], so our main results here are expected not to depend on the specific spin mixture. Having said this, the Hamiltonian of our system can be written as

$$\mathcal{H} = J \sum_{j=1}^N [\mathbf{S}_j \cdot \mathbf{s}_j + \mathbf{s}_j \cdot \mathbf{S}_{j+1} + D(S_j^z)^2], \quad (2.6.1)$$

where \mathbf{S}_j and \mathbf{s}_j are spin operators at the unit cell denoted by j and we adopt periodic boundary conditions in a system with N unit cells as sketched in Fig. 2.14. In the following, the strength of the exchange interaction J is set to unity. An important result regarding this model (in any dimension) has been obtained recently by Tian and Lin [115]. They proved rigorously that for an arbitrary bipartite lattice and spin mixture (S, s) with $S > s$, the global ground state is nondegenerate and has the total spin- z component $\mathcal{S}_z = 0$ when $D > 0$. On the other hand, when $D < 0$, the ground state becomes doubly degenerate with $\mathcal{S}_z = \pm N(S - s)$ and each state is antiferromagnetically ordered. When $D = 0$, the model reduces to the isotropic Heisenberg model, whose properties have been thoroughly studied. In particular, the Lieb-Mattis theorem [21] states that the system has total spin $\mathcal{S} = N(S - s)$ and therefore, its ground state is highly degenerate. Then, the value $D = 0$ is a critical (bifurcation) point indicating the reconstruction of the energy spectrum of the

system, so we expect that the entanglement, which is closely related with the structure of the ground-state, will present a special behavior at the critical point. Our aim in this section is to investigate this characteristic behavior which serve to indicate the quantum phase transition without reference to any specific order parameter. Moreover, we go beyond the ground state to study the effects of finite temperatures on the entanglement properties of the system. We do this by using the exact diagonalization of the Hamiltonian in Eq. (2.6.1) for small clusters.

Negativity as a measure of entanglement

We have commented that the Peres-Horodecki criterion is very useful in determining whether a state is entangled in high dimensional bipartite systems. The quantitative version of the Peres-Horodecki criterion was developed by Vidal and Werner [116], who presented a measure of entanglement, called the negativity, that can be computed effectively for any mixed state ρ of an arbitrary bipartite ($\mathcal{A} \otimes \mathcal{B}$) system and does not increase under local manipulations of the system. It essentially measures the degree to which the partial transpose ρ^{T_A} fails to be positive definite, by summing over its negative eigenvalues μ_i :

$$\mathcal{N}(\rho) = \sum_i |\mu_i| = \frac{1}{2}(\|\rho^{T_A}\|_1 - 1). \quad (2.6.2)$$

In the second equality, the trace norm of ρ^{T_A} is equal to the sum of the absolute values of the eigenvalues of ρ^{T_A} . Then if $\mathcal{N} > 0$ the system is in an entangled state. The negativity has been used to quantify the entanglement in a chain of harmonic oscillators [117, 118], in distant regions of XY spin chains at criticality [119], in free one-dimensional Klein-Gordon fields [120], in the spin-chain Kondo model [121], etc. Another quantity which is useful in the investigation of the structure of the ground state is the purity

$$\mathcal{P}(\rho) = \text{Tr}(\rho^2). \quad (2.6.3)$$

This is used to measure the degree of mixedness of a state described by the density operator ρ . For a pure state, we have $\mathcal{P} = 1$, whereas for a maximally mixed state, it reaches a minimum. The relation between entanglement and mixedness have attracted much attention in this last decade [122–126]; therefore it is believed that the purity of states can also indicate the critical point in some systems with quantum phase transitions. We use this concept here in order to complement and understand the results obtained with the negativity.

To study the quantum critical point in our system it suffices to consider the entanglement of two nearest-neighbor sites within a unit cell (pairwise entanglement). Since the finite

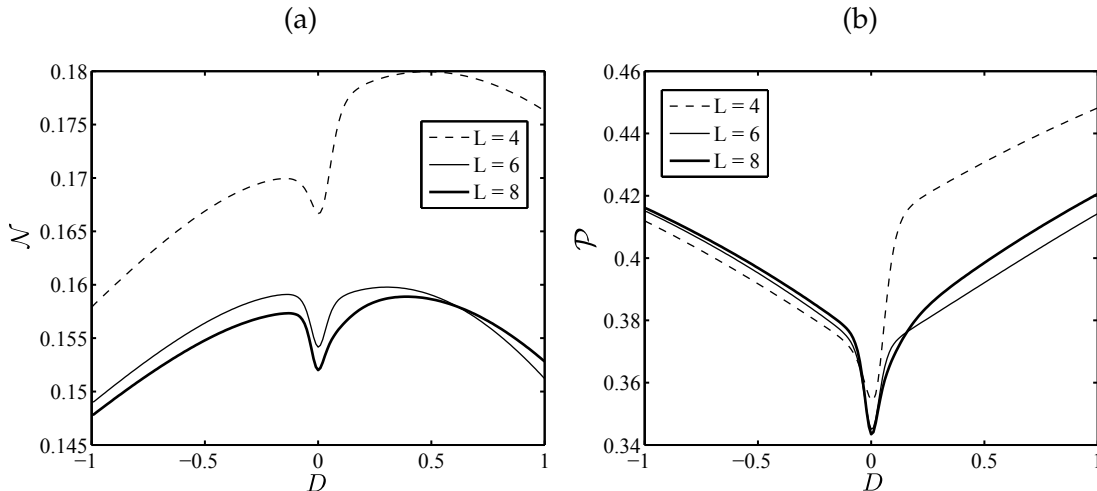


Figure 2.15: (a) Negativity versus the single-ion anisotropy D for different system sizes $L = 2N$ at a low temperature $T = 0.02$. The drop in the curves indicate the quantum critical point. (b) Purity versus the single-ion anisotropy D for different system sizes $L = 2N$ at a low temperature $T = 0.02$. The minimum in the curves indicate the quantum critical point.

system under the periodic boundary conditions is translationally invariant, it does not matter which unit cell we use for the calculation. Having said this, we compute the reduced density matrix of the two-spin subsystem, which then enters in Eqs. (2.6.2) and (2.6.3). Before doing this calculation, we first have to write a convenient form for the global ground state of the system, since as we have said, its degeneracy is not fixed as it explores the various quantum phases. The best way to take into account this, is to approximate the global ground state by considering the thermal state at low enough temperatures. This is described, at thermal equilibrium, by the Gibb's density operator $\rho_s(T) = \exp(-\mathcal{H}/T)/Z$, where the Boltzmann's constant is set to unity. Here $Z = \text{Tr}[\exp(-\mathcal{H}/T)]$ is the partition function, with T being the temperature. For low enough temperatures, the thermal state gives the mixture of all the degenerate ground states with equal probabilities. From this density operator, we proceed to calculate the reduced density matrix ρ by tracing out all other spin degrees of freedom in the subsystem complementary to the chosen unit cell. Although this method is not exact for the determination of the ground-state properties, it can still well manifest the main features [104, 105].

In Fig. 2.15 we show the results for the negativity and the purity versus the single-ion anisotropy for different system sizes $L = 2N = 4, 6, 8$ and temperature $T = 0.02$. As expected from the discussion above, both quantities develop a special behavior at the critical point, that is, whereas the negativity presents a pronounced dip, the purity reaches its minimum value. In the ground state of the total system at $T = 0$, this value can be calculated

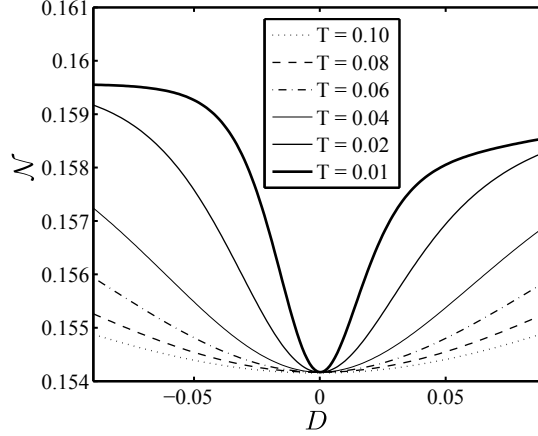


Figure 2.16: Effect of temperature on the dip of the negativity around the quantum critical point, for the system size $L = 6$.

easily as the following argument shows. Since the spin degeneracy at the isotropic point ($D = 0$) is $g = 2S + 1$, then each ground state is mixed with an equal probability $1/g$ in the system's density matrix ρ_s . Thus in the diagonal representation, the squared ground-state density matrix is $(\rho_s^2)_{ii'} = (1/g^2) \delta_{ii'}$. It follows that the minimum value of the purity at the critical point is given by $\mathcal{P}_{\min} = (1/g^2) \text{Tr}(\delta_{ii'}) = 1/[L(S - s) + 1]$. In the system with $S = 1$ and $s = 1/2$ under consideration this gives $\mathcal{P}_{\min} = 1/(N + 1)$. It is remarkable that the purity of the two-spin subsystem shown in Fig. 2.15(b) exhibits the special property of the whole system, namely, it shows a minimum at the critical point which decreases when the system size is increased. Finite size effects in our calculations are clearly appreciable as shown in Fig. 2.15(a), but what turns out to be important is that even in the $L = 4$ system, the information stored in the quantum phase transition is still captured.

The minimum in the purity at the quantum critical point indicates that the system reaches a maximally-mixed state. As pointed out by Fano a long time ago [127], as the system evolves from a pure state to this maximally-mixed state, the statistical fluctuations of any physical quantity measured in the system tend to increase, which is equivalent to say that we lose information about the system. In our present case it is easy to understand why we have a minimum of information at the quantum critical point: the transition to the isotropic point can be thought of as “adding degrees of freedom” to the system (since a high spin-degeneracy appears), or in other words, putting the system in contact with an environment. It is well-known that this operation causes *decoherence* and therefore a loss of information, so that the entanglement at the critical point is reduced as shown in Fig. 2.15(a). If we have this mechanism in mind, then it is natural to ask why the drop in the negativity begins to occur for D values around (and not at) the critical point. This is,

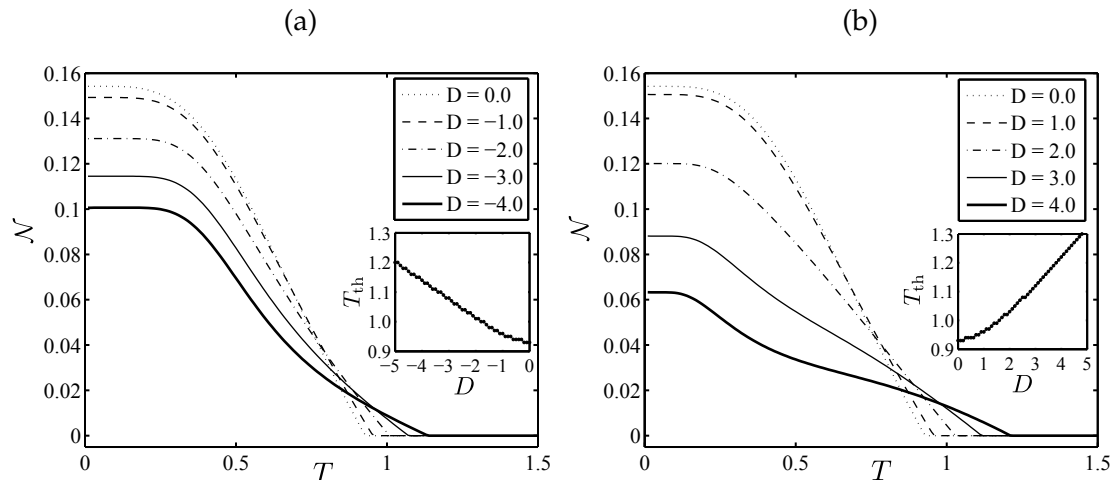


Figure 2.17: Negativity versus temperature for different values of the single-ion anisotropy for the system size $L = 6$. (a) The anisotropy D is varied in the easy-axis regime. (b) The anisotropy D is varied in the easy-plane regime. The inset figure shows the behavior of the threshold temperature (from which the thermal entanglement vanishes)

however, an effect due to finite temperatures as can be clearly seen in Fig. 2.16. As the system is cooled, the dip becomes sharper and sharper, and in the ground state we expect a sudden drop or discontinuity at the critical point. Then, by investigating the pairwise entanglement in the system, we are able to detect the quantum phase transition at $D = 0$ without using any order parameter. Now we proceed to discuss in detail the effects of temperature on the pairwise entanglement as we vary the single-ion anisotropy.

Thermal entanglement

The interest in thermal entanglement has been triggered since the fundamental question posed recently by Ferreira *et al.* [128]: can entanglement and the quantum behavior in physical systems survive at arbitrary high temperatures? They showed that this is indeed the case for an electromagnetic field mode in an optical cavity with a movable mirror in a thermal state. The situation for quantum mixed-spin chains has begun to be examined in the past few years. Experimental measurements of the magnetic susceptibility (an entanglement witness) in the mixed-spin $(S, 1/2)$ chain compounds mentioned before have determined characteristic or “threshold” temperatures above which the entanglement in the systems vanishes [107]. These temperatures are increased with the increase of the exchange interaction J and also with the increase of S . By introducing an inhomogeneous magnetic field [112] (as required for quantum computing), the threshold temperature is

also improved, so that the range where the entanglement exists is broadened. Here we consider the effect of the single-ion anisotropy on the threshold temperatures. In Fig. 2.17 we show the results for the negativity versus temperature as D is varied in the easy-axis ($D < 0$) and the easy-plane ($D > 0$) regimes, respectively. As we expected, for a fixed value of $|D|$, the negativity decreases as temperature increases until the threshold value T_{th} is reached, from which the negativity vanishes. This is reasonable since, as the temperature is increased, entropy is added to the system so that the quantum correlations (and thus entanglement) diminish until the quantum behavior disappears. As can be observed in the inset figures, the threshold temperature T_{th} increases with the increase of the single-ion anisotropy, being arbitrarily high when $|D|$ is large enough. Taking the value $J = 81.4 \text{ cm}^{-1}$ reported for the bimetallic NiCu (1, 1/2) chain compound [19] we find, for the system size $L = 6$, the value $T_{\text{th}} = 108.9 \text{ K}$ when $D = 0$, which can be compared with the approximate value [107] in the thermodynamic limit $T_{\text{th}} \approx 122 \text{ K}$. On the other hand, when $D = 3$, for example, we obtain the value $T_{\text{th}} = 131.1 \text{ K}$ which suggests that the sensitivity of the threshold temperature to variations of $|D|$ is rather weak, as confirmed by the step-like structure of the threshold temperature versus D . We observe that, for the easy-plane case, the step-like behavior is destroyed for values around $D = 2.6$, and then a linear dependence arises at least in the range of D values shown in Fig. 2.17(b).

A remarkable result from our calculations is that the entanglement in the easy-plane regime is more robust against temperature than in the easy-axis regime, although in the latter, the quantity of entanglement (negativity) is larger for large enough values of $|D|$ and low temperatures. This can be explained if we look at the qualitative effect of the single-ion anisotropy on the system in the ground state. When $D < 0$ we see from Eq. (2.6.1) that the states with high $\langle S^z \rangle$ are energetically favorable. Then when we increase D in this regime, the spin- S ions tend to point along the z -axis (up or down). On the other hand, when $D > 0$ the states with low $\langle S^z \rangle$ are preferable, and thus when D is increased in this regime, the spin- S ions turn towards a direction in the xy plane. Since there are infinitely many directions along which the spin- S ions can point within the plane, we say that the system has more degrees of freedom in this case, and therefore if we use the decoherence argument already used before we arrive at the conclusion that the entanglement in this case is less compared to the easy-axis case in which we only have two possibilities when $D \rightarrow -\infty$. Thus we conclude this section by saying that, although the entanglement is more robust against the temperature for the easy-plane regime, we find that, in general, the single-ion anisotropy improves the characteristic temperature above which the quantum behavior disappears.

2.6.2 Adding an external magnetic field

When an external magnetic field is added to the mixed-spin $(1, 1/2)$ chain with positive crystal-field anisotropy D on the spin-1 ions, the system also shows critical behavior. Sakai and Okamoto [129] have studied this mixed-spin system using the numerical exact diagonalization of finite clusters and size-scaling analyses. It exhibits a magnetization plateau at the magnetization per unit cell value $m = S - s = 1/2$ which also appears in the classical system. They found that a quantum phase transition with respect to D at $m = 1/2$ is revealed to occur due to the change of plateau formation mechanism, which they considered as an evidence to clarify that the plateau originates from the quantization of magnetization.

In this section we investigate the $(1, 1/2)$ mixed-spin Heisenberg chain with crystal-field anisotropy under an external magnetic field. Using the negativity as a measure of entanglement complemented with purity calculations we explore the quantum critical behavior of *large* systems by means of the DMRG algorithm. We show that these quantities borrowed from the quantum information theory give, in a very simple way, the quantum critical point of the model with higher accuracy than the one obtained from customary condensed matter approaches.

Competing interactions

The ferrimagnetic $(S, s) = (1, 1/2)$ mixed-spin chain with crystal-field anisotropy D under an external magnetic field H is described by the Hamiltonian

$$\mathcal{H} = \sum_{j=1}^N [\mathbf{S}_j \cdot \mathbf{s}_j + \mathbf{s}_j \cdot \mathbf{S}_{j+1} + D(S_j^z)^2 - H(S_j^z + s_j^z)], \quad (2.6.4)$$

where \mathbf{S}_j and \mathbf{s}_j are spin operators at the unit cell denoted by j and we adopt open boundary conditions in a system with N unit cells. Sakai and Okamoto used the valence-bond composite picture [130], where $S = 1$ is considered as the triplet state of two spin-1/2 variables, in order to describe the plateau state at $m = 1/2$. For small positive D each $S = 1$ site can be in any state of $S^z = -1, 0$, and 1 . Then in the plateau state at $m = 1/2$ the ideal ‘‘Haldane state’’, involving the trimer of three adjacent spin-1/2 variables in a $1 - 1/2 - 1$ spin sequence, namely $|\uparrow\rangle = \frac{1}{\sqrt{6}}(|\uparrow\uparrow\downarrow\rangle - 2|\uparrow\downarrow\uparrow\rangle + |\downarrow\uparrow\uparrow\rangle)$, covers the entire lattice. This state has the Néel order along H with local magnetizations $\langle S^z \rangle = 2/3$ and $\langle s^z \rangle = -1/6$. On the other hand, for large positive D each $S = 1$ tends to point along the xy plane, where $S^z = 0$. This local state at each spin-1 site is supported by one of the triplet states $\frac{1}{\sqrt{2}}(|\uparrow\downarrow\rangle + |\downarrow\uparrow\rangle)$, and in the plateau state at $m = 1/2$, the spin-1/2 sites must have $s^z = 1/2$. Then in the ideal large- D state the local magnetizations should be $\langle S^z \rangle = 0$ and $\langle s^z \rangle = 1/2$, and the

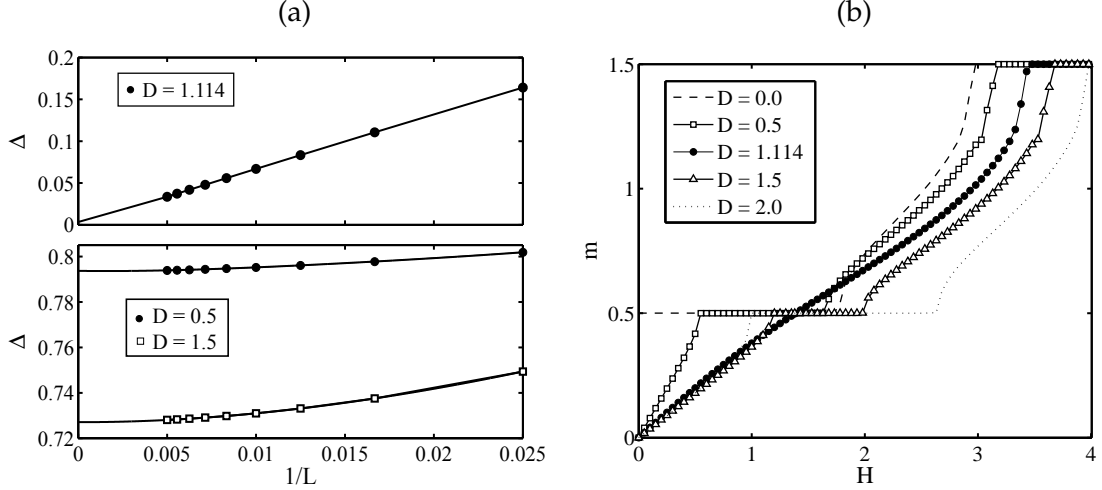


Figure 2.18: (a) Spin Excitation gap vs inverse system size for the critical value $D_c = 1.114 \pm 0.001$ found by Sakai and Okamoto [129] (upper panel) and two values far apart from this critical value (lower panel). The solid lines are fits based on the least-square method to see the asymptotic behavior in the thermodynamic limit. (b) Magnetization curves for different values of the crystal-field parameter D . As can be seen, the magnetization plateau at $m = 1/2$ vanishes (within our field resolution) for the D value used in the upper panel in (a) in which the system is almost gapless in the thermodynamic limit.

system does not exhibit the Néel order along the z axis. The existence of the two different mechanisms (the Haldane phase and the large- D phase) for the same plateau at $m = 1/2$ suggests the occurrence of a quantum phase transition between them with respect to the crystal-field parameter D . The critical point found by Sakai and Okamoto using the level spectroscopy method under the twisted boundary conditions [129], combined with a size-scaling analysis, was $D_c = 1.114 \pm 0.001$. Here we investigate the critical behavior using quantum information resources together with the powerful DMRG algorithm.

The competence between the effects produced by the magnetic field (which tends to align the spins along the z axis) and those produced by the positive crystal-field anisotropy (which tends to align the spin-1 sites along the xy plane) at the plateau state can be realized by using the spin excitation gap Δ at $m = 1/2$ as an order parameter. Let $E(N, M)$ denote the lowest energy in the subspace with a fixed magnetization M for the Hamiltonian in Eq. (2.6.4) without the Zeeman term. The upper and lower bounds of the field which induces the ground-state magnetization M are, respectively, given by

$$\begin{aligned} H_+(N, M) &= E(N, M+1) - E(N, M), \\ H_-(N, M) &= E(N, M) - E(N, M-1). \end{aligned} \quad (2.6.5)$$

Then the excitation gap at $m = 1/2$ (also the plateau length) is given by the quantity

$\Delta = H_+(N, M) - H_-(N, M)$ where $m \equiv M/N = 1/2$. If the system is gapless in the thermodynamic limit, the conformal field theory predicts [131–133] the asymptotic form of the size dependence of the gap as $\Delta \sim \mathcal{O}(1/N)$, i.e. the plateau vanishes in the thermodynamic limit. Otherwise, there is a finite gap and the system exhibits a plateau at $m = 1/2$. We have used the DMRG method with open boundary conditions to obtain the excitation gap for system sizes $L = 2N$ up to 200 sites. In all our calculations, the truncation error of the algorithm was always kept below 10^{-10} which required no more than 400 density matrix eigenstates per block. In Fig. 2.18(a) (upper panel) we show the calculated size-dependence of the excitation gap for the center value of D_c obtained by Sakai and Okamoto. Extrapolating to the thermodynamic limit we observe a dependence of the form $\Delta \sim 1/L$ (with intercept of $\mathcal{O}(10^{-4})$) indicated by the linear fit represented by the solid line, which suggests that very close from this center value, the system is gapless in the thermodynamic limit. For values of D far apart from D_c we observe from the lower panel of Fig. 2.18(a) that there is a finite gap in the thermodynamic limit, which then corresponds to the existence of the plateau at $m = 1/2$. This can be seen in the magnetization curves shown in Fig. 2.18(b), which were calculated for a system size $L = 500$ in order to remove any spurious effect due to the open boundaries. We observe from this figure that, around $H_c = H_+ = H_- \approx 1.38$, the plateau at $m = 1/2$ collapses. This value of the external magnetic field, at which all the magnetizations curve should intercept, may be considered as a critical field. This is the only information we need to determine D_c using the negativity and the purity as we show in the following.

Quantum critical point

We have calculated the negativity and the purity using Eqs. (2.6.2) and (2.6.3) with ρ being the reduced density matrix of the two sites at the middle of the chain (sites at positions $L/2$ and $L/2 + 1$ for even sizes), in order to avoid the boundary effects. This is easily calculated within the DMRG framework once the ground state is determined. We set the magnetic field H_c in the system and make a sweep of the crystal-field parameter D , looking for a special behavior of the quantities \mathcal{N} and \mathcal{P} around a certain point. This is shown in Figs. 2.19 and 2.20 for the system size $L = 200$. As can be seen, the negativity exhibits a very pronounced dip at a point very close to the value of D_c reported by Sakai and Okamoto, and the purity develops its global minimum also around this value. These special points determined with the negativity and the purity (for a given L) are different for finite size systems, as may be realized from the inset figures. However when we extrapolate to the thermodynamic limit we obtain an overlapping region where both quantities give the same

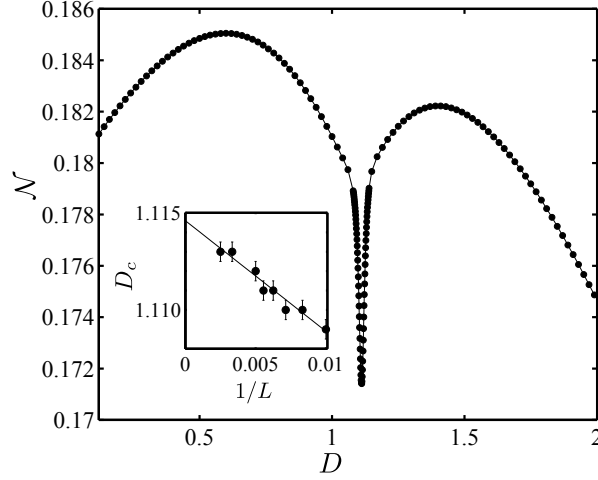


Figure 2.19: Ground-state entanglement (quantified with the negativity) as a function of the crystal-field parameter D , for the critical magnetic field $H_c = 1.38$ and system size $L = 200$. The inset figure shows the size dependence of D_c determined as the local minimum in the dip of the negativity, the solid line being a linear fit.

results. Taking into account the uncertainty $\Delta D = 5 \times 10^{-4}$ with which these points were calculated, the region is determined as $D_c = 1.11445 \pm 0.00065$. Then we can say with all the confidence that the minimum in the purity and the local minimum in the dip of the negativity both give, in the thermodynamic limit, the critical point at which the magnetization plateau at $m = 1/2$ vanishes. The result obtained with this method is more accurate than that obtained by Sakai and Okamoto since we have a wider statistical sample to make the extrapolation. Moreover, calculating minimum values is numerically more comfortable than determining the crossing point of two curves. This should not be considered as a rather detailed problem. The main point of our results is that the entanglement (together with related quantities such as the purity) store the relevant information about the quantum critical behavior of these mixed-spin chain models with competing interactions.

We can connect the qualitative behavior around D_c observed in Figs. 2.19 and 2.20 with those obtained with the excitation gap used as an order parameter of the quantum phase transition. The minimum in the purity indicates that the system reaches a maximally-mixed state, in which the statistical fluctuations of any measured physical quantity are maximized[127], and thus there is a minimum of information about the system. In the present case, it is easy to see why this happens: when the system reaches the critical point, the ground state becomes doubly degenerate, as indicated by the crossing of the lowest two energy levels (breakdown of the excitation gap). This suddenly brings more *alternatives* for the actual state of the system (similar to when a system is put in contact with an

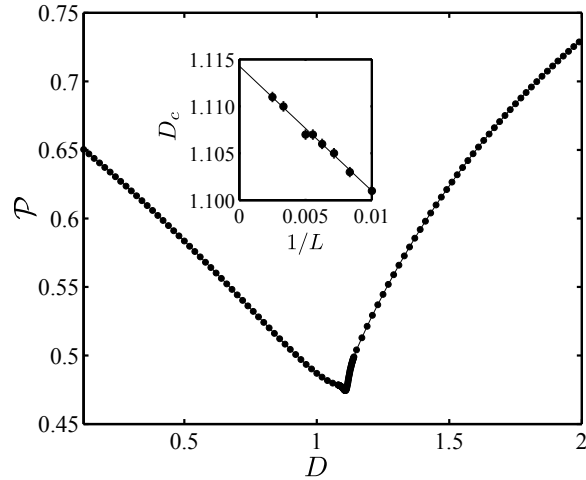


Figure 2.20: Ground-state mixedness (quantified with the purity) as a function of the crystal-field parameter D , for the critical magnetic field $H_c = 1.38$ and system size $L = 200$. The inset figure shows the size dependence of D_c determined as the minimum of the purity, the solid line being a linear fit.

environment) and might be thought of as a decoherence mechanism which causes a loss of information, so that the entanglement at this critical point is reduced, as shown by the local minimum in the dip of the negativity. Then, by considering the crystal-field anisotropy in the ferrimagnetic Heisenberg system, a very interesting physics arises which can be successfully investigated with the pairwise entanglement complemented with the purity, as a very attractive alternative to customary condensed matter techniques.

In summary, we have investigated several static properties of mixed-spin chains. We showed that mixed-spin (S, s) Ising chains with positive single-ion anisotropy exhibit $2s + 1$ plateaux in the ground-state magnetization curve, which generalizes to mixed-spin chains the well-known results for Ising spin- S chains, where $2S + 1$ plateaux appear in the magnetization curve. We also proved the validity of the spin-wave theory for mixed-spin Heisenberg chains with crystal-field anisotropy in the easy-axis regime, which could be important in the theoretical investigation of the low-temperature properties of these systems. Using a measure of entanglement, the negativity, complemented with purity calculations, we were able to signal the quantum phase transition in a mixed-spin Heisenberg chain with positive single-ion anisotropy. We also showed that this anisotropy arbitrarily increases the characteristic temperatures above which the entanglement (and thus the quantum behavior) disappears in the system. When an external magnetic field is added, we showed how the critical point of the system can be calculated using entanglement and purity with more accuracy than customary condensed matter approaches.

Ground-state dynamical properties

Recent experimental achievements in controlling ultracold gases in optical lattices open a new perspective on quantum many-body physics. In these experimental setups it is possible to study coherent time evolution of isolated quantum systems. These dynamics reveal new physics beyond the low-energy properties usually relevant in solid-state many-body systems. In this chapter we introduce the adaptive time-dependent DMRG algorithm in order to study a particular example of the time evolution of a state prepared in a mixed-spin alternating chain, with a subsequent analysis of the corresponding evolution of entanglement.

3.1 Dynamics with DMRG

The dynamical properties of a magnetic system are governed by the time-dependent pair correlation functions or their Fourier transforms. Quantities of experimental interest include the dynamical correlation functions in neutron scattering experiments, the NMR spin-lattice relaxation rate, various relaxation functions and associated lineshapes as well as the dynamical response of the magnetic system to various spectroscopic probes [134]. Dynamical two-point correlation functions (Green's functions) are defined in the Heisenberg picture as

$$iG_{\mathcal{A}}(t' - t) = \langle \psi_0 | \mathcal{A}^\dagger(t') \mathcal{A}(t) | \psi_0 \rangle, \quad (3.1.1)$$

with \mathcal{A} being some operator of interest, $|\psi_0\rangle$ the ground state of the system and $t' \geq t$. After a Fourier transform into frequency space this reads

$$G_{\mathcal{A}}(\omega + i\eta) = \langle \psi_0 | \mathcal{A}^\dagger \frac{1}{E_0 + \omega + i\eta - \mathcal{H}} \mathcal{A} | \psi_0 \rangle, \quad (3.1.2)$$

where E_0 is the ground-state energy of the system with Hamiltonian \mathcal{H} and η is some positive number¹ to be taken to zero at the end. This is related to the spectral or Lehmann representation of correlations, defined as

$$C_{\mathcal{A}}(\omega) = \sum_n |\langle \psi_n | \mathcal{A} | \psi_0 \rangle|^2 \delta(\omega + E_0 - E_n), \quad (3.1.3)$$

via

$$C_{\mathcal{A}}(\omega) = -\frac{1}{\pi} \lim_{\eta \rightarrow 0^+} \text{Im} G_{\mathcal{A}}(\omega + i\eta). \quad (3.1.4)$$

Calculating dynamical properties with DMRG has proven to be much harder than obtaining static properties. The main challenge in calculating a spectral function is to find a basis of the reduced DMRG Hilbert space that optimally represents all states $|\psi_n\rangle$ involved in Eq. (3.1.3). The first approach was made by Hallberg who used the continued fraction method to calculate $G_{\mathcal{A}}(\omega + i\eta)$ [31]. That is, if we write $z = \omega + i\eta$ then Eq. (3.1.2) can be written as

$$G_{\mathcal{A}}(z) = \frac{\langle \psi_0 | \mathcal{A}^\dagger \mathcal{A} | \psi_0 \rangle}{z - a_0 - \frac{b_1^2}{z - a_1 - \frac{b_2^2}{z - \dots}}}, \quad (3.1.5)$$

where the coefficients a_n and b_n can be obtained using the recursion equations

$$|f_{n+1}\rangle = \mathcal{H}|f_n\rangle - a_n|f_n\rangle - b_n^2|f_{n-1}\rangle; \quad |f_0\rangle = \mathcal{A}|\psi_0\rangle, \quad (3.1.6)$$

with

$$\begin{aligned} a_n &= \langle f_n | \hat{\mathcal{H}} | f_n \rangle / \langle f_n | f_n \rangle, \\ b_n^2 &= \langle f_n | f_n \rangle / \langle f_{n-1} | f_{n-1} \rangle; \quad b_0 = 0. \end{aligned} \quad (3.1.7)$$

Then in this method one has to target the ground state $|\psi_0\rangle$ and the first few $|f_n\rangle$ (tens or hundreds, depending on the problem). This works well as long as the spectral representation in Eq. (3.1.3) consists of only a few well separated peaks and hence only a very small number of states have to be represented in the reduced basis. Once a band of excitations occurs this approach breaks down.

Another approach is to use the ‘‘correction vector DMRG’’ [135, 136]. Here, in addition to the ground state $|\psi_0\rangle$ of the system, one also targets the state $|\mathcal{A}\rangle = \mathcal{A}|\psi_0\rangle$ and the real and imaginary part of the so-called correction vector defined as

$$|c(z)\rangle = \frac{1}{E_0 + z - \mathcal{H}} |\mathcal{A}\rangle. \quad (3.1.8)$$

¹This quantity ensures causality in Eq. (3.1.2) and introduces a finite lifetime $\tau \propto \frac{1}{\eta}$ to excitations.

Once these states are known, the Green's function in Eq. (3.1.2) can be calculated by the simple scalar product

$$G_{\mathcal{A}}(z) = \langle \mathcal{A} | c(z) \rangle. \quad (3.1.9)$$

The correction vector itself has to be calculated in every DMRG step, by solving (with the well-known GMRES routine, for example) the system of linear equations

$$(E_0 + z - \mathcal{H})|c(z)\rangle = |\mathcal{A}\rangle, \quad (3.1.10)$$

which is currently done by splitting the correction vector into real and imaginary part and calculating them separately,

$$[(E_0 + \omega - \mathcal{H})^2 + \eta^2]\text{Im}|c(z)\rangle = -\eta|\mathcal{A}\rangle, \quad (3.1.11)$$

$$\text{Re}|c(z)\rangle = \frac{\mathcal{H} - E_0 - \omega}{\eta}\text{Im}|c(z)\rangle. \quad (3.1.12)$$

Since the frequency ω enters explicitly in the correction vector used as a target state one in principle has to perform a DMRG run for every ω of interest. This is of course very time-consuming. Kühner and White [136] showed that taking two correction vectors at different frequencies ω_1 and $\omega_2 = \omega_1 + \Delta\omega$ one can calculate $G_{\mathcal{A}}(z)$ for frequencies between ω_1 and ω_2 using the continued fraction method. This works well as long as $\Delta\omega$ is not too large and the correction vectors thereby not too different. Due to the large number of runs necessary to obtain a spectral function over a large frequency interval, the correction vector method is numerically more expensive than the continued fraction algorithm. Nevertheless it has been applied to many different systems, for example, it was used to calculate the nonlinear optical coefficients of Hubbard chains [137] and the AC-conductivity of the Bose-Hubbard model with nearest neighbor interactions [138]. Also quantum impurity problems have been investigated using this algorithm [139].

Although the above mentioned methods provide high-quality linear response quantities, they fail in truly out-of-equilibrium situations, or for time-dependent Hamiltonians, where they work, they are very time-consuming. It has therefore been of high interest to find DMRG approaches dealing with the time evolution but not in frequency space. Cazalilla and Marston [140] were the first to exploit DMRG to systematically calculate time-dependent quantum many-body effects. They studied a time-dependent Hamiltonian $\mathcal{H}(t) = \mathcal{H}(0) + V(t)$, where $V(t)$ encodes the time-dependent part of the Hamiltonian. After applying a standard DMRG calculation to the hamiltonian $\mathcal{H}(0)$, the time-dependent Schrödinger equation was numerically integrated forward in time. The initial condition was obviously to take $|\psi(0)\rangle$ as the ground state of $\mathcal{H}(0)$ obtained by the preliminary DMRG run. This procedure amounts to working within a *static* effective Hilbert space, namely that optimal

at $t = 0$, and projecting all wave functions and operators onto it. In this approach the hope is that an effective Hamiltonian obtained by targeting the ground state of the $t = 0$ Hamiltonian is capable to catch the states that will be visited by the time-dependent Hamiltonian during time evolution. This approach must however break down after relatively short times as the full Hilbert space is explored, as became quickly obvious. In a comment challenging the accuracy of the calculation, Lou *et al.* proposed [141] to additionally target $|\psi(t_n)\rangle$ for different times $t_n = n\Delta t$, i.e. for the determination of the effective Hilbert space, they used a density matrix given by the superposition $\rho = \sum_{n=1}^{N_t} \alpha_n |\psi(t_n)\rangle \langle \psi(t_n)|$ with $\sum \alpha_n = 1$. This improves the accuracy for larger times but, as this is done at each step of the algorithm, it results very time-consuming.

As we shall see in the next section, the adaptive time-dependent DMRG algorithm, instead of using a static effective Hilbert space, it tries to adjust the states kept in the reduced basis from time to time so that the state $|\psi(t)\rangle$ is always approximated very well.

3.2 Adaptive time-dependent DMRG

Investigating the time-evolution of a given quantum many-body state $|\psi(t)\rangle$ under the action of a Hamiltonian \mathcal{H} is one of the most challenging tasks in theoretical physics. In order to calculate $|\psi(t > 0)\rangle$ one can either integrate the Schrödinger equation ($\hbar = 1$)

$$\frac{\partial}{\partial t} |\psi(t)\rangle = -i\mathcal{H}|\psi(t)\rangle \quad (3.2.1)$$

forward in time or calculate and apply the time-evolution operator $U(t) = e^{-i\mathcal{H}t}$. The textbook solution to do the latter is to expand $|\psi(0)\rangle$ in the eigenbasis of the Hamiltonian leading to $|\psi(0)\rangle = \sum_n c_n |\psi_n\rangle$. From this we can obtain the well-known time-evolution

$$|\psi(t)\rangle = U(t)|\psi(0)\rangle = \sum_n c_n e^{-iE_n t} |\psi_n\rangle, \quad (3.2.2)$$

with time-independent coefficients c_n . If we choose another basis to represent the initial state, i.e. $|\psi(0)\rangle = \sum_m d_m |\chi_m\rangle$, one can of course express each $|\chi_m\rangle$ in terms of the Hamiltonian eigenstates: $|\chi_m\rangle = \sum_n a_{mn} |\psi_n\rangle$. Then the time-dependent state reads

$$|\psi(t)\rangle = \sum_{mn} d_m a_{mn} e^{-iE_n t} |\psi_n\rangle. \quad (3.2.3)$$

Transforming this time-evolved state back into the $|\chi_m\rangle$ basis via $|\psi_n\rangle = \sum_{m'} a'_{nm'} |\chi_{m'}\rangle$ we obtain

$$|\psi(t)\rangle = \sum_{m'} \left(\sum_{mn} d_m a_{mn} a'_{nm'} e^{-iE_n t} \right) |\chi_{m'}\rangle = \sum_{m'} d_{m'}(t) |\chi_{m'}\rangle. \quad (3.2.4)$$

As can be observed, the coefficients $d_{m'}(t)$ are explicitly time-dependent. In order to calculate them, one has to know a complete set of eigenstates and corresponding eigenvalues of the full Hamiltonian. In a DMRG algorithm, a state is always given in the basis of the truncated effective DMRG Hilbert space. Thus an effective Hamiltonian \mathcal{H}_{eff} , acting only on this space, is used to calculate the effective time-evolution operator. The effective Hilbert space is chosen to represent optimally $|\psi(0)\rangle$. However, as said before, $|\psi(t > 0)\rangle$ may get out of this effective space, and the bases states approximating $|\psi(0)\rangle$ optimally may lead to a very poor approximation of $|\psi(t)\rangle$ at larger times. The time-dependence of $d_{m'}(t)$ in Eq. (3.2.4) shows that the effective DMRG Hilbert space should change in time in order to optimally represent $|\psi(t)\rangle$. This is the basic idea of the *adaptive* time-dependent DMRG algorithm (adaptive t-DMRG).

The original adaptive t-DMRG was invented independently by Daley *et al.* [142] on the one hand, and by White and Feiguin [143] on the other hand, for systems with nearest neighbor interactions only. In this case, the time-evolved state $|\psi(t + \Delta t)\rangle = e^{-i\mathcal{H}\Delta t}|\psi(t)\rangle$ can be calculated using the Suzuki-Trotter decomposition of the matrix exponential. Up to second order, this reads [143]

$$e^{-i\mathcal{H}\Delta t} \approx e^{-ih_{1,2}\Delta t/2}e^{-ih_{2,3}\Delta t/2} \dots e^{-ih_{L-1,L}\Delta t} \dots e^{-ih_{2,3}\Delta t/2}e^{-ih_{1,2}\Delta t/2}, \quad (3.2.5)$$

where we have written \mathcal{H} as a sum over nearest neighbor interactions $\mathcal{H} = \sum_i h_{i,i+1}$.

Before the time evolution starts, we typically use the standard DMRG to find the ground state. Next, we either (i) change the Hamiltonian, or (ii) apply an operator to the ground state to study a new wave function which is a combination of excited states. We are going to give examples of these two alternatives in the following two sections. The next step is to apply $\exp(-ih_{1,2}\Delta t/2)$ at finite-system DMRG step 1, then $\exp(-ih_{2,3}\Delta t/2)$ at step 2, etc., forming the usual left-to-right sweep, then reverse, applying all the reverse order terms in the right-to-left sweep. This procedure requires one to use the step-to-step wave function transformation first developed by White to provide a good guess for the starting vector in the Lanczos or Davidson diagonalization routine. It just transforms the wave function from the basis of step $l \pm 1$ to that of step l . It is easy to compute this transformation as follows: at DMRG step $l - 1$, remember that we have the left block $\mathcal{B}(l - 1, m)$ and right block $\mathcal{B}'(L - l - 1, m)$. To transform a quantum state $|\psi^{l-1}\rangle$ of the system into the new basis for the next step l (which involves the blocks $\mathcal{B}(l, m)$ and $\mathcal{B}'(L - l - 2)$ in the left-to-right sweep) one uses the transformation matrices O defined in section 2.3. Let us use the notation O_{l-1} for the matrix applied to truncate the left enlarged block at step $l - 1$ to form the left block at step l . Then if we define $g(a, \alpha)$ as an index in the enlarged block coming from the tensor product of indexes a in the block and α in the site added to the block, we

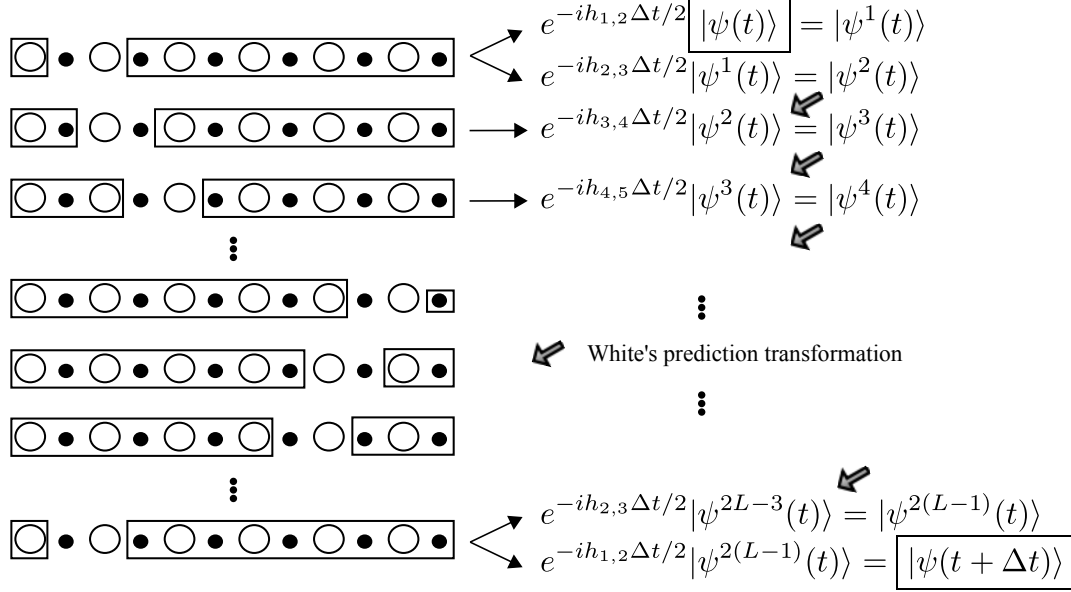


Figure 3.1: Schematic representation of the adaptive t-DMRG algorithm.

can write the White's prediction transformation as

$$\psi_{a\alpha\beta b}^l = \sum_{\bar{a}\bar{b}} O_{l-1}^{*g(\bar{a},\bar{\alpha})a} O'_{L-l-2}{}^{g(\beta,b)\bar{b}} \psi_{\bar{a}\bar{\alpha}\bar{b}}^{l-1}. \quad (3.2.6)$$

A schematic representation of the adaptive t-DMRG algorithm is shown in Fig. 3.1. As can be seen in this figure, the state $|\psi(t)\rangle$ is evolved to $|\psi(t + \Delta t)\rangle$ in one DMRG sweep.

Two main sources of error occur in the adaptive t-DMRG. (i) The *Trotter error* due to the Suzuki-Trotter decomposition of the time-evolution operator. For an n th-order Trotter decomposition [144], the error made in one time step Δt is of order $(\Delta t)^{n+1}$. To reach a given time t one has to perform $t/\Delta t$ time-steps, such that in the worst case the error is of order $t(\Delta t)^n$. Since a linear dependence of the error with the system size is expected for generic initial states, then the overall error is of order $tL(\Delta t)^n$. (ii) The DMRG *truncation error* due to the representation of the time-evolving quantum state in the reduced Hilbert spaces and to the repeated transformations between different truncated basis sets. Nevertheless the most serious error in an adaptive t-DMRG program remains this truncation error. A nearly perfect time evolution with a negligible Trotter error is completely worthless if the wave function is affected by a relevant truncation error. Since the precision of the algorithm becomes poorer and poorer as times grows larger and larger, due to the accumulated truncation and Trotter error at each DMRG step, there will be a certain instant of time, called the *runaway time* where the precision decreases by several order of magnitude. This can be increased with m and a small Δt , but decreases with the number of Trotter steps and with L . A detailed discussion on the runaway time can be seen in Ref. [145].

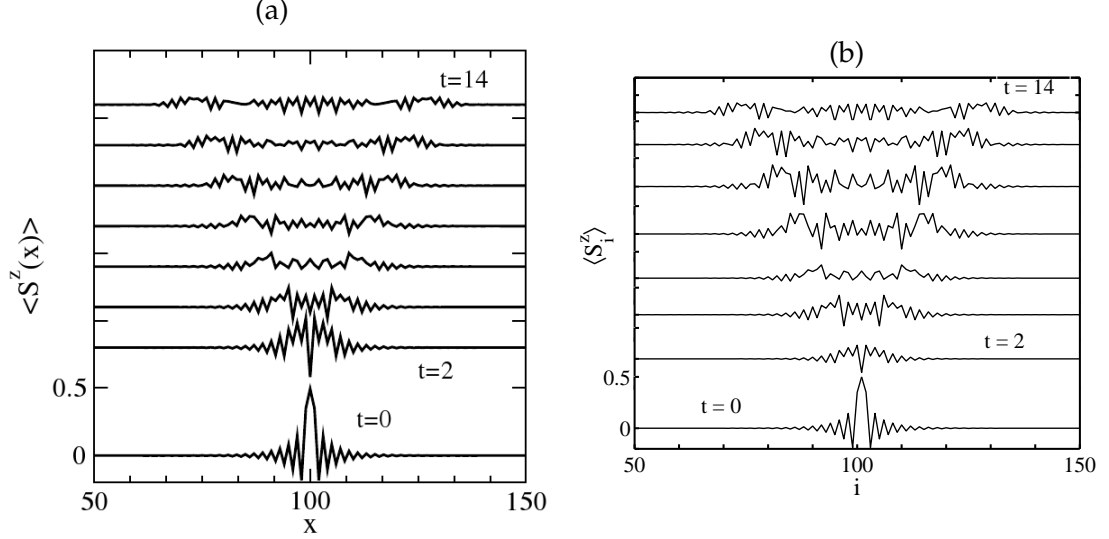


Figure 3.2: Time evolution of the local magnetization $\langle S_i^z \rangle$ of a 200 site spin-1 Heisenberg chain after S_{100}^+ is applied. (a) Results obtained by White and Feiguin in Ref. [143]. (b) Results obtained with our implemented adaptive t-DMRG algorithm.

In the next two sections we reproduce one of the original results of White and Feiguin (applying an operator to the ground state and evolving the resulting state) and one of the results of Gobert *et al.* [145] (evolving the ground state of a Hamiltonian under a different Hamiltonian in the propagator). Then we proceed to study the time-evolution in a mixed-spin chain.

3.3 Spectral function of the spin-1 Heisenberg chain

In this section we reproduce the time evolution of the local magnetization of a 200 site spin-1 antiferromagnetic Heisenberg chain as presented in Ref. [143]. This system has a gap (the Haldane gap) of $\Delta_H = 0.4105J$ to the lowest excitations, which are spin-1 magnons at momentum π , and a finite correlation length of $\xi = 6.03$. First we calculate the ground state $|\psi_0\rangle$ using the standard DMRG. Then we apply the operator $S^+ = S^x + iS^y$ at the center of the chain to obtain the initial state $|\psi(0)\rangle = S_{100}^+|\psi_0\rangle$. This operator constructs a localized wave packet consisting of all wave vectors, which then spreads out. The different components move at different speeds, given by the group velocity, determined as the slope of the dispersion curve at momentum k . In Fig. 3.2 we show the local magnetization $\langle \psi(t) | S_i^z | \psi(t) \rangle$, using a time step of $\Delta t = 0.1$. At $t = 0$, the wave packet has a finite extent, with size given by the spin-spin correlation length ξ . At latter times, the different speeds of the different components give the irregular oscillations in the center of the packet.

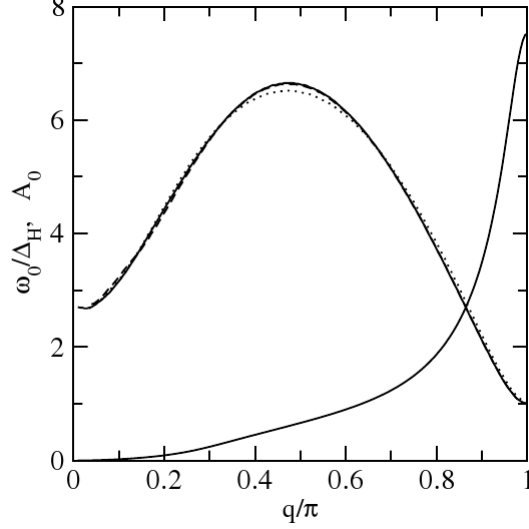


Figure 3.3: The single-magnon line of the spin-1 antiferromagnetic Heisenberg chain. The entire spectrum is obtained from one DMRG run, by Fourier transforming the time and position dependent correlation function $\langle S_x^-(t)S_0^+(0) \rangle$. The broad solid curve shows the location of the maximum in the spectra for a particular q in units of the Haldane gap. The solid curve peaked at $q = \pi$ is the weight A_0 in this quasiparticle peak, i.e., the spectral function is $S(\omega) \approx A_0\delta(\omega - \omega_0)$ (See Ref. [143]).

To calculate time-dependent correlation functions, we have to time evolve both $|\psi_0(t)\rangle$ and $|\psi(t)\rangle$, including both as target states for the DMRG density matrix. Although the time dependence $\exp(-iE_0t)$ of $|\psi_0(t)\rangle$ is known, by evolving it we keep its representation in the current basis. Then, with the above mentioned simulation, we can construct the Green's function

$$iG(x, t) = \langle \psi_0 | T[S_x^-(t)S_0^+(0)] | \psi_0 \rangle \quad (3.3.1)$$

as $iG(x, t) = \langle \psi_0(|t)| | S_x^- | \psi(|t) \rangle$ in the Schrödinger representation. Here x is measured from the center of the chain (where S^+ was applied). While Kühner and White calculated the single-magnon dispersion relation with excellent accuracy [136], they could not calculate the entire magnon spectrum for this system, for as we saw in section 3.1 this is quite tedious with frequency-based DMRG. White and Feiguin succeeded in doing this with only one time-dependent DMRG run. By Fourier transforming the time-dependent correlation function

$$G(k, \omega) = 2 \int_0^\infty dt \cos \omega t \sum_x \cos kx G(x, t), \quad (3.3.2)$$

the spectral function is calculated as $S(k, \omega) = -\frac{1}{\pi} \text{Im} G(k, \omega)$, where $G(x, t)$ is measured for each left-to-right DMRG step, as the evolution in time is performed. In Fig. 3.3 we

show their results for only the single-magnon line, represented by the broad solid line. As can be seen, it shows a minimum at $k = \pi$ representing the lowest excitation (spin-1 magnons) created by exciting the ground state of the system with an energy equal to the haldane gap. The solid curve peaked at this minimum stands for the amplitude A_0 of spectral function $S(\omega) \approx A_0\delta(\omega - \omega_0)$.

3.4 Evolution of a domain wall in a spin-1/2 chain

In this section we reproduce one of the results of Gobert *et al.* [145]. That is, we study the time evolution of the state $|\psi(0)\rangle = |\uparrow \cdots \uparrow \downarrow \cdots \downarrow\rangle$ in a spin-1/2 chain with XX exchange interactions. This state, which contains many high-energy excitations and is thus far from equilibrium, is the ground state of the Hamiltonian $\mathcal{H}(0) = \sum_i B_i S_i^z$ with $B_i < 0$ for i on the left, and $B_i > 0$ for i on the right half of the chain, which is equivalent to switching on a magnetic field that aligns the spins and that is strong enough for all XX interactions to be negligible. Then we turn off the magnetic field and let the system evolve. Note that, since the total energy and magnetization of the system are conserved at all times, even for long times the state can not relax to the ground state.

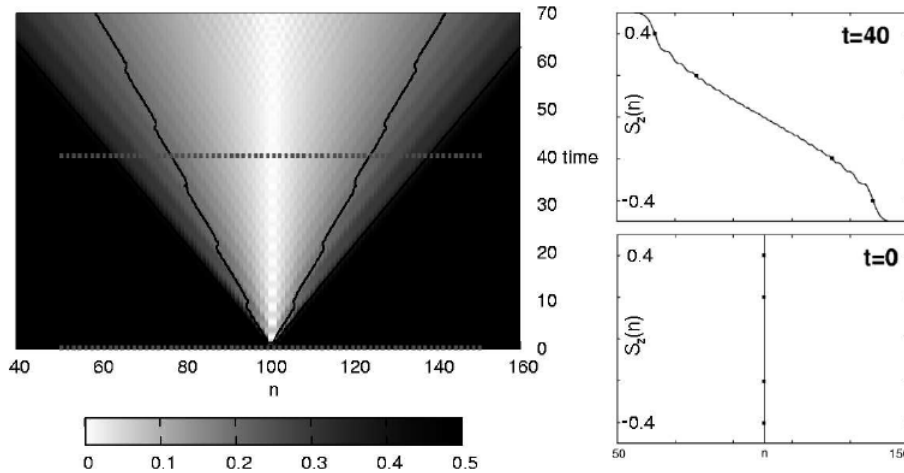


Figure 3.4: Left: Time evolution of the absolute value of the local magnetization $|\langle S_i^z(t) \rangle|$ of a spin-1/2 chain for the XX model shown as a density plot. Right: Local magnetizations for the time slices $t = 0$ and $t = 40$. For details see Ref. [145].

The time evolution, which can be solved exactly in this model by mapping the XX Hamiltonian onto a model of spinless fermions using the Jordan-Wigner transformation, delocalizes the domain wall over the entire chain. For example, the magnetization profile for

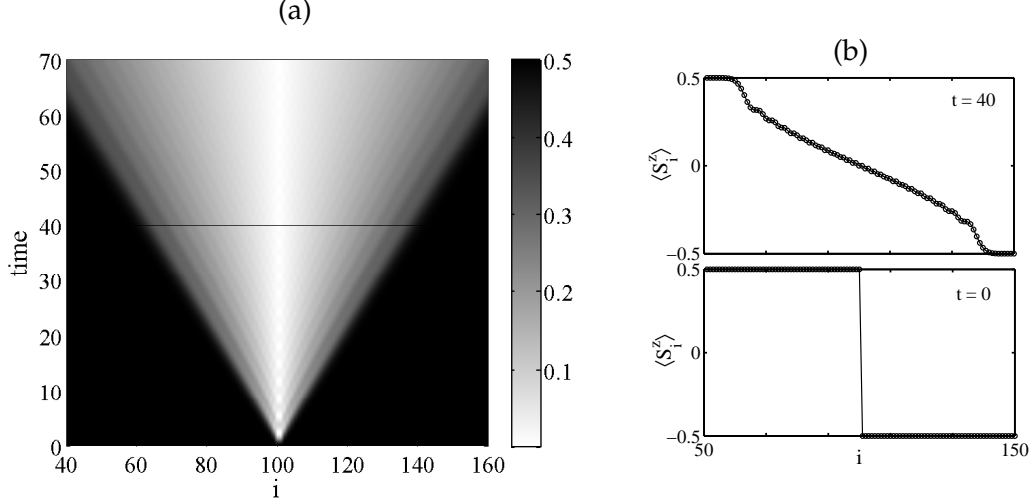


Figure 3.5: Time evolution of the local magnetization of a spin-1/2 chain for the XX model as reproduced by our implemented adaptive t-DMRG algorithm. Compare with the results shown in Fig. 3.4.

the initial state $|\psi(0)\rangle$ reads

$$S_i^z(t) = \langle \psi(t) | S_i^z | \psi(t) \rangle = -\frac{1}{2} \sum_{k=1-i}^{i-1} J_k^2(t), \quad (3.4.1)$$

where J_k is the Bessel function of the first kind, $i = \dots, -3, -2, -1, 0, 1, 2, 3, \dots$ labels chain sites with the convention that the first site in the right half of the chain has label $i = 1$. In Fig. 3.4 we show the results obtained by Gobert *et al.* for the evolution of the local magnetization. It was found that the magnetization in Eq. (3.4.1) can be described for long times in terms of a simple scaling function, $S_i^z(t) \approx \Phi((i - i_c)/t)$, where i_c is the position of the chain center. This function has been shown [146] to describe the macroscopic time evolution of the magnetization profile, which has a well-defined front at $(i - i_c)/t = \pm 1$, i.e. is moving outwards ballistically with velocity $v = 1$. This can be corroborated from the Fig. 3.4 as the slope of the plane cone. On top of this overall scaling form an additional step-like (ray-like in the density plots) substructure arises, which was analysed in detail in Ref. [146]. It represents the “carriers” in terms of which the initial magnetization relaxes. In Fig. 3.5 we show the results obtained with our implemented algorithm, which correctly reproduce those shown in Fig. 3.4. This allows us to apply the same tools to investigate the evolution of a similar initial state prepared in a mixed-spin quantum XX chain, which we outline in the next section.

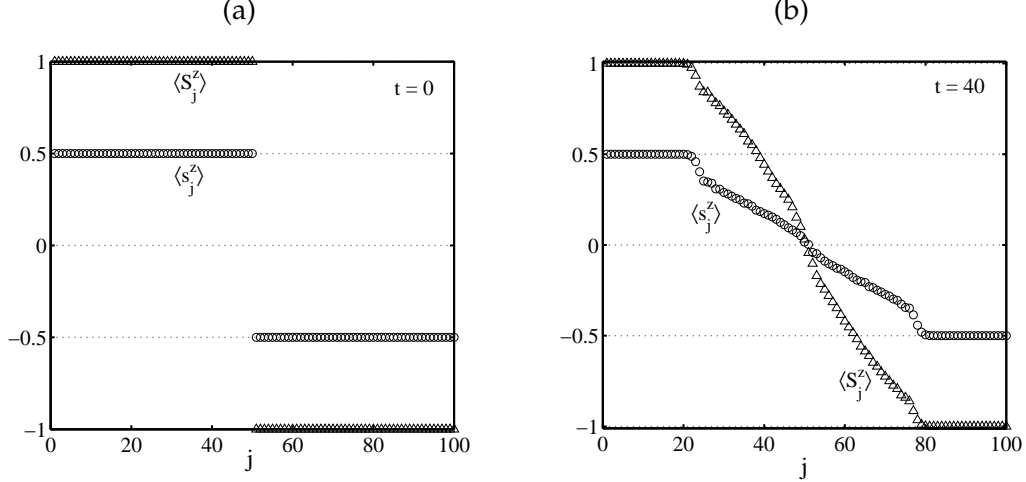


Figure 3.6: Local magnetizations of the mixed-spin $(S, s) = (1, 1/2)$ chain for the XX model. (a) Profile at the initial time $t = 0$. (b) Profile when the system has evolved to the time $t = 40$. Here we show the results for sublattice magnetizations in a 200 site chain.

3.5 Domain-wall dynamics in a mixed-spin XX chain

Now we consider a related problem to that in the former section. We study the time evolution in a mixed-spin $(S, s) = (1, 1/2)$ quantum XX chain. We set out a non-uniform strong-enough magnetic field which aligns the spins in the initial configuration $|\psi(0)\rangle = |\uparrow\uparrow\cdots\uparrow\uparrow\downarrow\downarrow\cdots\downarrow\downarrow\rangle$, where $|\uparrow\rangle$ represents the local spin-1 microstate $|m_S = 1\rangle$, and $|\downarrow\rangle$ represents the local spin-1/2 microstate $|m_s = \frac{1}{2}\rangle$. The magnetization profile for each sublattice in this initial state is shown in Fig. 3.6(a). Then we turn off the magnetic field and let the system evolve. The Hamiltonian of this system for $t > 0$ can be written as

$$\mathcal{H} = J \sum_j (S_j^x s_j^x + S_j^y s_j^y + s_j^x S_{j+1}^x + s_j^y S_{j+1}^y), \quad (3.5.1)$$

where $S = 1$ and $s = 1/2$, and j runs over $N = L/2 = 100$ unit cells. The case $S = s = 1/2$ was envisaged in the former section, where the subsequent evolution of a the domain wall was commented. Here we have a similar behavior as can be seen in Fig. 3.6(b) for the time $t = 40$. The difference is that we can see, in this case, the time evolution as the emergence of two fronts (one within each sublattice) which interfere with each other and propagate outwards with the same speed. In this system, we can also observe a staircase structure in the magnetization profile. In the uniform spin-1/2 system, it was found by Hunyadi *et al.* [146] that while the height of the steps in the staircase decreases with time as $t^{-1/3}$ and their width increases as $t^{1/3}$, the areas under the steps are time-independent constants and, furthermore, the constants are the same for all the steps. The value of this constant (twice the magnetic moment of a spin) suggested that a step carries a localized flipped spin flow-

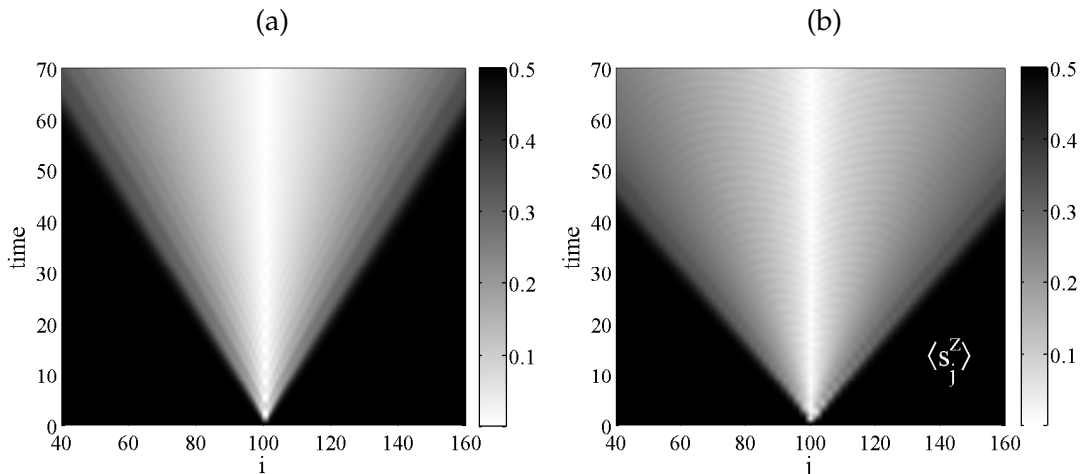


Figure 3.7: Time evolution of the absolute value of the local magnetization shown as density plots (a) for the spin-1/2 chains (b) for the spin-1/2 sublattice in a mixed $(S, s) = (1, 1/2)$ spin chain.

ing outwards with the front velocity (ray-like structure in Fig. 3.5(a)), which keep their identity with respect to other reversed spins. Then, since the initial magnetization relaxes in well defined quantized “steps” (in space and time), they concluded that these quantum fronts, in particular, the steps carrying a unit of spin flips, could be envisioned as ingredients in controlled transport of bitwise information in magnetic nanostructures. This called our attention for the mixed-spin chain, since in this system the “carriers” move with a higher speed in the spin-1/2 sublattice, as can be seen in Fig. 3.7(b), where we compare with the front propagation in the uniform-spin case 3.7(a) discussed in the former section. This is better in a practical application where a much faster transmission of information is preferred. We are currently working in the theoretical description of the front propagation, which includes the investigation of a scaling function for the long-time behavior of the macroscopic magnetization profile. The dependence on the initial state is also under development.

3.6 Evolution of entanglement entropy

It has been shown [147] that the efficiency in simulating a quantum many-body system is strictly connected to its entanglement behavior. More precisely, if the entanglement of a subsystem with respect to the whole system is bounded (or grows logarithmically with its size) an efficient simulation with DMRG is possible. Up to now, it is known that ground states of one-dimensional lattices (whether critical or not) satisfy this requirement.

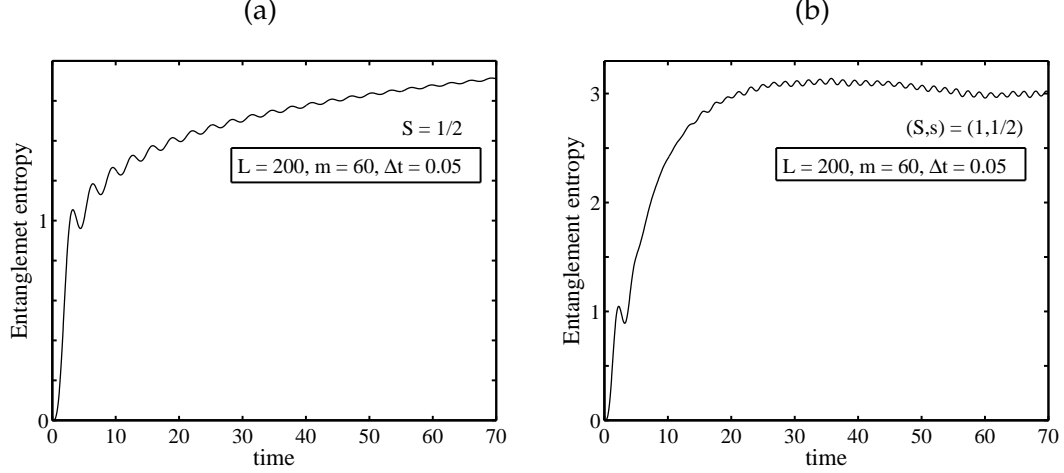


Figure 3.8: Evolution of entanglement entropy between the left and the right half of the chain (a) in the spin-1/2 chain for the XX model (b) in the mixed $(S, s) = (1, 1/2)$ spin chain for the same model.

The interest in the properties of entanglement in condensed matter has also extended to understanding its dynamical behavior. Like for the case of propagation of excitations in condensed media, it recently became of interest to know how entanglement could propagate through spin chains (see Refs. [148–151] and references therein). In this section we inquire into the dynamics of entanglement in the systems studied in the two former sections. We use the von Neumann entropy (entanglement entropy) S_m of the block containing the left half of the chain, as a measure of entanglement between the two halves of the chain. This is defined as

$$S_m = -\text{Tr}(\rho_m \log_2 \rho_m), \quad (3.6.1)$$

where $\rho_m = \rho_m(t)$ is the reduced density matrix of the aforementioned block. In Fig. 3.8(a) we show our results for the spin-1/2 chain with the domain-wall initial state relaxing as discussed in section 3.4. Since this state is a product state, it has no entanglement, as shown in the figure for $t = 0$. As the system evolves, the block entropy increases until a saturation point is obtained. This result improves the one reported by Gobert *et al.* [145]. A similar increasing behavior for the entanglement entropy was discussed in Ref. [149] for blocks containing l sites. There, the system is quenched from initial states in the non-critical regime of the Heisenberg model to the critical one (including the XX regime). The block entropy increases with time and saturates at $t^* = l/v$ where v is the spin-wave velocity: $\partial E_k / \partial k|_{k=0}$, and open boundary conditions are considered. This was interpreted in terms of quasiparticle excitations emitted from the initial state at $t = 0$ and freely propagating with velocity v . In Fig. 3.8(b) we show our results for our mixed $(S, s) = (1, 1/2)$ spin system. We immediately observe that the saturation takes place much earlier than in

the spin-1/2 case, which seems to be highly associated with the much faster propagation of the carriers in the mixed-spin chain. We are currently investigating the relation between these carriers and the quasiparticles of Ref. [149], in order to give a rigorous basis to these beliefs.

In summary, we have discussed an extension of DMRG to study the real-time dynamics in mixed-spin chains. With this, we have reproduce some known results for uniform spin chains. Then we investigated the time evolution of a domain-wall prepared in a mixed-spin $(S, s) = (1, 1/2)$ XX chain with a subsequent study of the dynamics of the entanglement entropy. We have shown that the propagation of fronts in this systems is much faster, under similar conditions, than the propagation in a spin-1/2 chain under the same model, which is better for applications in the transport of bitwise information in magnetic nanostructures.

Static properties at finite temperature

The low-energy structure and the thermodynamic properties of ferrimagnetic quantum chains has remained at the forefront of research in condensed matter physics during several decades. The main interest comes from the ability to synthesize bimetallic magnetic materials which display one-dimensional magnetism, although in recent years, examples of compounds with alternating organic radicals as magnetic centers, rather than metal ions, have appeared. In this chapter we describe the special features in the thermal behavior of alternating mixed-spin chains, and present an example of a recently synthesized material where the low-temperature properties deviate from the expected ferrimagnetic behavior. By using the spin-wave theory and DMRG arguments, we give an explanation of the unconventional features of this material. We also discuss the most up-to-date DMRG algorithms for finite temperatures, which are at the forefront in the investigation of thermal properties of one-dimensional strongly correlated quantum systems.

4.1 Inherent features of one-dimensional ferrimagnets

The thermodynamic properties of one-dimensional ferrimagnets with two kinds of spin S and s ($S > s$) have been studied experimentally for many systems and a theoretical progress into them can be appreciated nowadays. There lie both ferromagnetic and antiferromagnetic long-range orders in the ground state. The ground state, which is a multiplet of spin $(S - s)N$, shows elementary excitations of two distinct types. The excitations of ferromagnetic aspect, reducing the ground state magnetization, form a gapless dispersion relation, whereas those of antiferromagnetic aspect, enhancing the ground state magnetization, are gapped from the ground state. As a result of the low-energy structure of dual aspect, the specific heat shows a Schottky-like peak in spite of the ferromagnetic low-

temperature behavior, and the magnetic susceptibility times temperature exhibits a round minimum [18, 152]. Yamamoto *et al.* [153] have characterized ferrimagnetic Heisenberg chains according to the constituent spins. They used an efficient Quantum Monte Carlo (QMC) technique as well as the modified spin wave theory [154]. The core idea of the latter can be summarized as controlling the number of spin-wave bosons by imposing a certain constraint on the magnetization. They impose the zero-magnetization constraint

$$\sum_j \langle S_j^z + s_j^z \rangle = (S - s)N - \sum_k \sum_{\sigma=\pm} \sigma \tilde{n}_k^{-\sigma} = 0, \quad (4.1.1)$$

which expresses that the thermal spin deviation should cancel the Néel-state magnetization. Here $\tilde{n}_k^\pm = \sum_{n^-, n^+} n^\pm P_k(n^-, n^+)$ with $P_k(n^-, n^+)$ being the probability of n^- ferromagnetic and n^+ antiferromagnetic spin waves appearing in the k -momentum state. Minimizing the free energy with respect to $P_k(n^-, n^+)$ at each k under the condition in Eq. (4.1.1) as well as the trivial constraints $\sum_{n^-, n^+} P_k(n^-, n^+) = 1$, they obtain for the specific heat and magnetic susceptibility the low-temperature expansions

$$\begin{aligned} \frac{C}{Nk_B} &= \frac{3}{4} \left(\frac{S-s}{Ss} \right)^{\frac{1}{2}} \frac{\zeta(\frac{3}{2})}{\sqrt{2\pi}} \tilde{t}^{\frac{1}{2}} - \frac{1}{Ss} \tilde{t} + O(\tilde{t}^{\frac{3}{2}}), \\ \frac{\chi J}{N(g\mu_B)^2} &= \frac{Ss(S-s)^2}{3} \tilde{t}^{-2} - (Ss)^{\frac{1}{2}} (S-s)^{\frac{3}{2}} \frac{\zeta(\frac{1}{2})}{\sqrt{2\pi}} \tilde{t}^{-\frac{3}{2}} + (S-s) \left[\frac{\zeta(\frac{1}{2})}{\sqrt{2\pi}} \right]^2 \tilde{t}^{-1} + O(\tilde{t}^{-\frac{1}{2}}), \end{aligned} \quad (4.1.2)$$

where $\tilde{t} = k_B T / J\gamma$ with $\gamma = 1 - \Gamma_1(S+s)/Ss - \Gamma_2/\sqrt{Ss}$, with Γ_1 and Γ_2 defined as in section 2.5 with $D = 0$. The (ferromagnetic-like) low-temperature properties of the model are qualitatively the same regardless of the values of S and s as long as they differ from each other. The dispersions for the mixed-spin systems are $\omega_k^\pm = J\sqrt{(S-s)^2 + 4Ss \sin^2(ak)} \pm J(S-s)$ (see section 2.5), while that of the spin- S ferromagnetic Heisenberg chain is the well-known quadratic dispersion $\omega_k = 2JS[1 - \cos(ak)]$. Thus, only in the $S = 2s$ cases, the ferromagnetic branch ω_k^- of the spin- (S, s) ferrimagnets show exactly the same dispersion as the spin- s ferromagnets at small momenta. Consider for example the mixed $(S, s) = (1, 1/2)$ Heisenberg chain. The precise low-temperature behavior of the spin-1/2 ferromagnet has been determined by Takahashi and Yamada [155]. Numerically solving the thermodynamic Bethe-ansatz integral equations, they succeeded in explaining the thermal quantities in powers of $t^{1/2}$ as

$$\begin{aligned} \frac{C}{Nk_B} &= 0.7815t^{1/2} - 2.00t + 3.5t^{3/2} + O(t^2), \\ \frac{\chi J}{N(g\mu_B)^2} &= 0.04167t^{-2} + 0.145t^{-3/2} + 0.17t^{-1} + O(t^{-1/2}), \end{aligned} \quad (4.1.3)$$

where $t = \gamma\tilde{t}$. The coefficients in this expansions coincide up to four digits in the leading terms (the $T^{1/2}$ asymptotic behavior of the specific heat and the T^{-2} divergence of the magnetic susceptibility) with those of Eq. (4.1.2) for $(S, s) = (1, 1/2)$. Then this system is identified with the spin-1/2 ferromagnet at low enough temperatures.

At mid temperatures in the specific heat, the antiferromagnetic aspect most clearly appears. The specific heat exhibits a sharp peak, rather than the broad one characteristic of ferromagnets, and therefore reminds us of the Schottky anomaly peculiar to the antiferromagnetic specific heat [64]. Therefore the mid-temperature behavior of the specific heat is reasonably attributed to gapped antiferromagnetic excitations. At these mid temperatures, the χT product displays a rounded minimum.

The high temperature behavior of the system is paramagnetic since the thermal fluctuations destroy the correlations among the spins. In this limit, the energy of the system does not vary appreciably (due to saturation) when we make a slight change in the temperature and thus the specific heat must go to zero, and the magnetic susceptibility behaves as

$$\frac{\chi k_B T}{N(g\mu_B)^2} = \frac{1}{3} [S(S+1) + s(s+1)] \quad (4.1.4)$$

In the next section we show results of this characteristic behavior using our implemented DMRG algorithm for finite temperatures, using enlarged Hilbert spaces.

4.2 Purification as an alternative to DMRG at $T > 0$

In recent years, ideas from the quantum information field have greatly extended the capabilities of DMRG [147, 156]. Zwolak and Vidal [157], and Verstraete *et al.* [158], separately, devised methods allowing finite-temperature DMRG. The approach of Zwolak and Vidal introduced the idea of a matrix-product description of density operators, rather than of wave functions. Within this formulation, the infinite temperature system is trivial to describe, and imaginary-time evolution is used to reach finite temperature. Verstraete *et al.* argued that a more efficient procedure is to enlarge the Hilbert space with auxiliary sites (called ancillas), and to evolve in imaginary time a pure state within the larger space. The auxiliary states act as a perfect heat bath, and when traced out give exact thermodynamic averages. Feiguin and White [159] applied this idea to standard DMRG, and here we adapt it to mixed-spin systems. The essential procedure can be sketched as follows:

Let the energy eigenstates of the system in question be $\{|\psi_n\rangle\}$. Then we build the unnormalized pure quantum state, in an enlarged Hilbert space (purification)

$$|\psi(\beta)\rangle = e^{-\beta\mathcal{H}/2}|\psi(0)\rangle = \sum_n e^{-\beta E_n/2}|\psi_n\rangle \otimes |\tilde{\psi}_n\rangle, \quad (4.2.1)$$

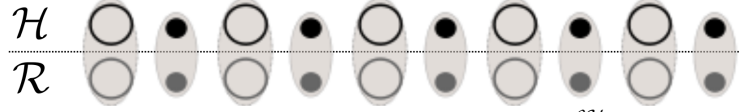


Figure 4.1: The purification of the density operator $\rho(\beta) = e^{-\beta\mathcal{H}}$ on a Hilbert space \mathcal{H} is a pure state $|\psi(\beta)\rangle$ on an enlarged Hilbert space $\mathcal{H} \otimes \mathcal{R}$ such that $\rho(\beta) = \text{Tr}_{\mathcal{R}}|\psi(\beta)\rangle\langle\psi(\beta)|$. The infinite temperature state is obtained by preparing each pair of a physical site and the corresponding auxiliary site in a maximally entangled state.

where $|\tilde{\psi}_n\rangle$ is the matching state to $|\psi_n\rangle$, and $|\psi(0)\rangle = \sum_n |\psi_n\rangle \otimes |\tilde{\psi}_n\rangle$ is the thermal vacuum. Note that the Hamiltonian only applies to the real sites; the ancilla evolve only through their entanglement acting as a thermal bath. From this, it is easy to show that the partition function is

$$Z(\beta) = \langle\psi|\psi\rangle, \quad (4.2.2)$$

and the exact thermodynamic average of an operator \mathcal{A} (acting only on the real sites) is given by

$$\langle\mathcal{A}\rangle = Z(\beta)^{-1}\langle\psi|\mathcal{A}|\psi\rangle. \quad (4.2.3)$$

At $\beta = 0$, the state $|\psi\rangle$ is the maximally entangled state between the real system and the fictitious system. Notice that if we change basis from the energy eigenstates to some other arbitrary basis $|s\rangle$, then $|\psi\rangle$ is still maximally entangled: $|\psi(0)\rangle = \sum_s |s\rangle \otimes |\tilde{s}\rangle$. Therefore, using the local basis at site i indexed by s_i , the vacuum state can be written as

$$|\psi(0)\rangle = \prod_i \sum_{s_i} |s_i\rangle \otimes |\tilde{s}_i\rangle. \quad (4.2.4)$$

In Fig. 4.1 we show the representation of the enlarged Hilbert space, where site+ancilla is comprised into a “supersite”, shown as ellipses. Then the essence of the ancilla finite-temperature method (T-DMRG) is to start in this local $\beta = 0$ state, and evolve in imaginary time¹ through a succession of temperatures β . To evolve in time we use the adaptive t-DMRG algorithm discussed in section 3.2. The infinite temperature initial state has a correlation length of 0 and requires only one state per block. As the system evolves in imaginary time, longer range entanglement is produced and the correlation length grows. Thus the number of DMRG basis states needed for a given accuracy grows as the temperature decreases. In our results we kept the truncation error below 10^{-10} , which in the systems considered corresponded typically to no more than $m = 200$. We calculate the specific heat by taking the numerical derivative of the energy with respect to the temperature, using energy differences between adjacent time steps. On the other hand, the magnetic

¹Note that the exponential operator in Eq. (4.2.1) is like a time-evolution operator with $t \rightarrow -i\beta/2$.

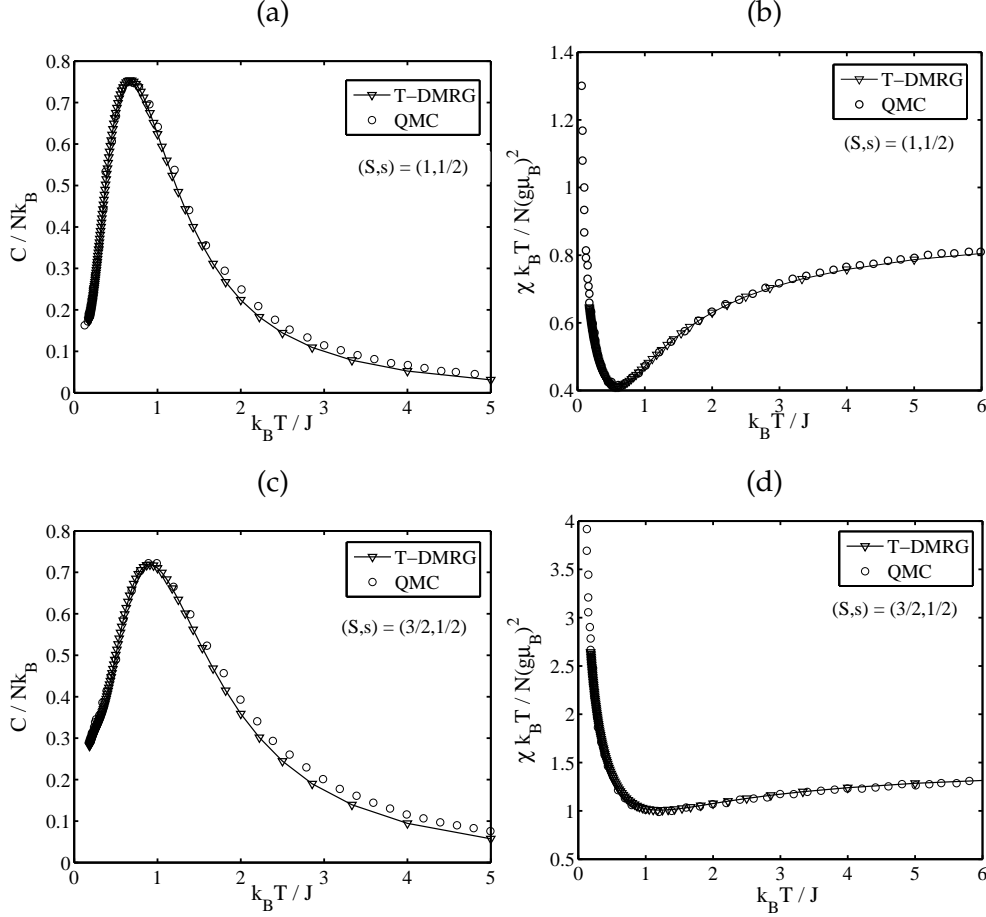


Figure 4.2: Specific heat and magnetic susceptibility of (a)-(b) the mixed $(S, s) = (1, 1/2)$ spin chain, and (c)-(d) the mixed $(S, s) = (3/2, 1/2)$ spin chain, both with $L = 64$ sites. The circles represent quantum Monte Carlo calculations taken from Ref. [153].

susceptibility is calculated by adding a very small magnetic field, and taking the numerical derivative of the magnetization of the system with respect to this field. The results obtained by Feiguin and White reproduce with extreme accuracy, in chains with $L = 64$, those obtained by Xiang, in the thermodynamic limit, using the transfer-matrix DMRG [160], and also the exact calculations with the Bethe ansatz.

To the best of our knowledge, the present T-DMRG algorithm has not been used for mixed-spin chains before. Here we compare with the results obtained by Yamamoto *et al.* [153] using the modified spin-wave theory and QMC. In order to test the veracity of our implementation, we only show the cases $(S, s) = (1, 1/2)$ and $(S, s) = (3/2, 1/2)$, comparing only with the QMC calculations. We use chains with $L = 64$ sites. The results are shown in Fig. 4.2. As can be seen, the agreement with QMC is excellent, particularly for low temperatures. We believe that the errors in the QMC data are amplified for the specific heat

at high temperatures. Note that for the two systems shown there appears a Schottky-like peak in the specific heat, and the χT curve decreases continuously upon cooling (characteristic of 1D antiferromagnets), reaches a rounded minimum, and then increases at low temperatures (characteristic of 1D ferromagnets), as was discussed in the former section. The same qualitative behavior was observed in Ref. [153] for the systems $(S, s) = (3/2, 1)$ and $(S, s) = (2, 1)$. It is believed that this is a generic feature of the thermodynamic properties of one-dimensional ferrimagnets.

The ancilla T-DMRG algorithm is nowadays one of the most used methods to study thermal properties of one-dimensional strongly correlated quantum systems. Two years ago, Sota and Tohyama [161] proposed a DMRG algorithm which is a straightforward extension of the standard ground-state DMRG and is suitable for low temperatures. On the other hand, White [162] introduced last year the minimally entangled typical thermal states, whose ensemble, generated by thermalizing classical product states and then making quantum measurement on the results, give excellent thermodynamic averages. In order to keep continuity in the exposition we refer the reader to appendix A for a brief discussion of these algorithms. In the next section we proceed to the description of a recently synthesized alternating mixed-spin chain with a novel magnetic behavior which deviates from the aforementioned ferrimagnetic features.

4.3 Unconventional features of a dimerized chain

Low-dimensional quantum ferrimagnets have been attracting much current theoretical and experimental interest. The simplest system in one dimension consists of two kinds of spins S and s alternating on a ring with antiferromagnetic exchange coupling between nearest neighbors, and a series of such family compounds were extensively synthesized by Verdaguer, Kahn, and their coworkers [17]. The most well-known systems [18, 19] are the bimetallic chains of general formula $ACu(pbaOH)(H_2O)_3 \cdot nH_2O$ with $A=Ni, Co, Fe, Mn$. They all show the same qualitative behavior inherent to one-dimensional ferrimagnets, namely the $\chi_M T$ product (χ_M being the molecular susceptibility per unit cell) smoothly decreases upon cooling, reaches a minimum and then increases at low temperatures, and the specific heat shows a sharp Schottky-like peak at mid temperatures. The elementary excitations of these chains have been extensively analysed and the characteristic properties have been shown to be the result of a ferromagnetic-antiferromagnetic crossover [55, 63–66], due to the competition between excitations to a gapless ferromagnetic and a gapped antiferromagnetic branch in the energy spectrum. This is believed to be the generic scenario for arbitrary ferrimagnetic Heisenberg chains [53]. When a bond alternation $0 \leq \delta \leq 1$ is

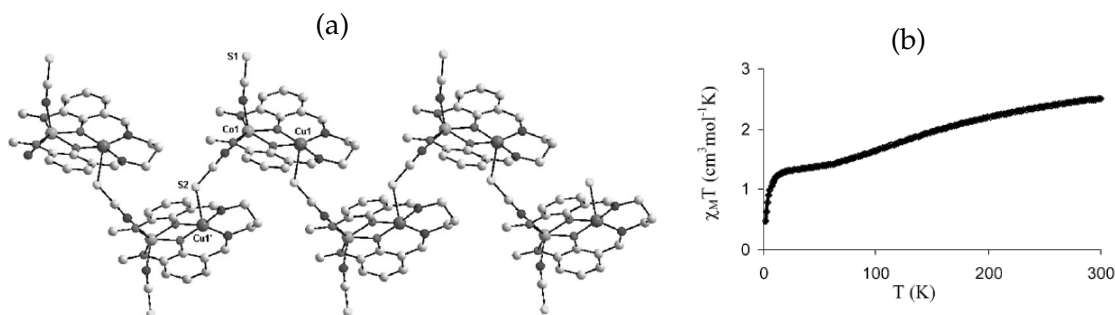


Figure 4.3: (a) Crystal structure of the 1D coordination polymer $1_{\infty}[\text{LCu}^{\text{II}}\text{Co}^{\text{II}}(\text{NCS})_2]$. For more details see Ref. [164]. (b) Corresponding temperature dependence of $\chi_M T$. The full line represents the best data fit using exact diagonalization for $L = 8$ sites.

introduced in the Hamiltonian:

$$\mathcal{H} = J \sum_j \left[\mathbf{S}_j \cdot \mathbf{s}_j + \delta \mathbf{s}_j \cdot \mathbf{S}_{j+1} + D(S_j^z)^2 \right], \quad (4.3.1)$$

it has been shown that the qualitative behavior for an arbitrary combination (S, s) and a single-ion anisotropy term $D = 0$, remains unchanged [55, 63]. To the best of our knowledge, there are no extensive theoretical works for the case $\delta < 0$. We believe this is due to the lack of experimental data concerning these mixed-spin alternating chains. The difficulties found in the synthesis of these systems are associated with both the design of ferromagnetically coupled dimers and their polymerization through bridging ligands which mediate intradimer antiferromagnetic coupling. A few systems with $S = s$ have been reported and reviewed [163]. They consist of alternate chains of Ni(II) and Mn(II) ions with alternating end-on and end-to-end azido bridges. Recently, a novel bimetallic (Co,Cu) alternating chain $1_{\infty}[\text{LCu}^{\text{II}}\text{Co}^{\text{II}}(\text{NCS})_2]$ with ferromagnetically coupled ($\delta < 0$) dimers has been synthesized by Costes *et al.* [164] (see Fig. 4.3(a)). The magnetic behavior of this mixed-spin $(S, s) = (3/2, 1/2)$ system is very different from the aforementioned ferromagnetic $\delta > 0$ case. The $\chi_M T$ values decrease upon lowering the temperature but not continuously, for where a minimum followed by a rapid increase is expected, a pseudo-plateau followed by a rapid decrease at low temperatures is observed, as can be seen in Fig. 4.3(b). They first suggested that this decrease could be due to the zero-field splitting D of the cobalt(II) ion ground state but later in the paper they showed evidence for absence or very small D contribution in their chain compound. Moreover, from structural studies they also came to the conclusion that the decrease was induced by the ferromagnetic δ term. Using exact diagonalization at finite temperatures for a tetranuclear complex and for a closed-chain of four dinuclear units they found very similar results which allowed them to think of these results as well describing the thermodynamic limit.

The best fit to the $\chi_M T$ vs. T curve using this method gave the experimental parameters $J_{\text{exp}} = 101.2 \text{ cm}^{-1}$, $(J\delta)_{\text{exp}} = -2.8 \text{ cm}^{-1}$ and $(JD)_{\text{exp}} = 0.11 \text{ cm}^{-1}$, with an agreement factor given by $R = 7.0 \times 10^{-5}$.

In this section we clarify the role of δ and D on the observed low-temperature properties of the above mentioned dimerized mixed-spin chain compound. In the following, *when left unspecified*, we use the dimensionless parameters $J = 1$, $\delta = (J\delta)_{\text{exp}}/J_{\text{exp}} \approx -0.0277$ and $D = (JD)_{\text{exp}}/J_{\text{exp}} \approx 0.0011$ which resembles the experimental parameters. In section 4.3.1 we develop a spin-wave argument which clearly shows us the need for a departure from the ferrimagnetic ground state in chains with $\delta < 0$. In section 4.3.2 we inquire further into the ground state properties of the system by using DMRG at $T = 0$. Finally, in section 4.3.3 we investigate the effect of δ and D on the specific heat and the magnetic susceptibility, using exact diagonalization at finite temperatures.

4.3.1 The spin-wave approach

We assume that the system has a Néel-ordered ferrimagnetic ground state with total magnetization $M = (S - s)N$ and define the bosonic operators for the spin deviation in each sublattice through the Holstein-Primakoff transformation [83]

$$\begin{aligned} S_j^+ &= \sqrt{2S - a_j^\dagger a_j} a_j, & S_j^z &= S - a_j^\dagger a_j, \\ s_j^+ &= b_j^\dagger \sqrt{2s - b_j^\dagger b_j}, & s_j^z &= -s + b_j^\dagger b_j. \end{aligned} \quad (4.3.2)$$

In order to obtain the dispersion relations of the spin-wave excitations, we rewrite the Hamiltonian in terms of the above defined bosonic operators, expand to quadratic order and Fourier transform to get

$$\mathcal{H} = J \sum_k \left(c_a a_k^\dagger a_k + c_b b_k^\dagger b_k + \gamma_k a_k b_k + \gamma_k^* a_k^\dagger b_k^\dagger \right), \quad (4.3.3)$$

where $k = \pi l/Na$ runs over half of the first Brillouin zone ($l = -N/2 + 1, -N/2 + 2, \dots, N/2$), with a being the distance between two neighboring spins and N the number of unit cells. We note that the unit cell is of length $2a$. Here $c_a = (1 + \delta)s - 2DS$, $c_b = (1 + \delta)S$ and $\gamma_k = \sqrt{Ss}[1 + \delta \exp(2iak)]$. Then we diagonalize the bosonic Hamiltonian by means of a Bogoliubov transformation of the form

$$\begin{aligned} \alpha_k &= e^{ia\lambda_k/2} u_k a_k + e^{-ia\lambda_k/2} v_k b_k^\dagger, \\ \beta_k &= e^{-ia\lambda_k/2} v_k a_k^\dagger + e^{ia\lambda_k/2} u_k b_k, \end{aligned} \quad (4.3.4)$$

where the hyperbolic relation $u_k^2 - v_k^2 = 1$ must hold in order to preserve the bosonic commutation relations. The conditions for simultaneous elimination of the $\alpha_k \beta_k$ and $\alpha_k^\dagger \beta_k^\dagger$

contributions in the Hamiltonian are

$$\begin{aligned} (1 + \delta) \tan[a(k - \lambda_k)] &= (1 - \delta) \tan(ak), \\ (u_k^2 + v_k^2)R_k - (c_a + c_b)u_kv_k &= 0, \end{aligned} \quad (4.3.5)$$

where $R_k = (Ss)^{1/2} \sqrt{(1 + \delta)^2 - 4\delta \sin^2(ak)}$ is defined for the sake of clarity. With this, we obtain

$$\mathcal{H} = E_0 + \frac{J}{2} \sum_k \left(\omega_k^- \alpha_k^\dagger \alpha_k + \omega_k^+ \beta_k^\dagger \beta_k \right), \quad (4.3.6)$$

where $E_0 = -JNS(D + c_a) + J/2 \sum_k [\omega_k - (c_a + c_b)]$ is the ground state energy up to $O(S^1)$ and the dispersion relations are given by

$$\omega_k^\pm = \omega_k \pm (c_b - c_a), \quad \text{with } \omega_k = \sqrt{(c_a + c_b)^2 - 4R_k^2}. \quad (4.3.7)$$

We see that the assumption of a Néel state leads to a ferromagnetic-like branch ω_k^- , which is gapped

$$\Delta_{k \rightarrow 0}^- = \frac{J}{2} \left[\sqrt{(c_b - c_a)^2 - 8Dsc_b} - (c_b - c_a) \right] + \frac{J\delta Ss(2ak)^2}{\sqrt{(c_b - c_a)^2 - 8Dsc_b}}, \quad (4.3.8)$$

as long as $D \neq 0$, and an antiferromagnetic branch ω_k^+ which is gapped regardless of the D value

$$\Delta_{k \rightarrow 0}^+ = \frac{J}{2} \left[\sqrt{(c_b - c_a)^2 - 8Dsc_b} + (c_b - c_a) \right] + \frac{J\delta Ss(2ak)^2}{\sqrt{(c_b - c_a)^2 - 8Dsc_b}}. \quad (4.3.9)$$

Although the effect of the D term on the elementary excitations (and thus in the thermodynamics) of systems with $\delta > 0$ is interesting in its own, here we just notice, as may be seen in Fig. 4.4, that when $D = 0$ and we decrease δ from the Heisenberg point, the lowest-energy band starts to flatten until we reach a negative value and a change in concavity occurs. It seems that the spin-wave description fails in this regime, since the ground-state energy E_0 is no longer the lowest energy of the system. We believe this is due to the destruction of the Néel order, which was our starting assumption. It is worthy to mention that a similar phenomenon was found by Ivanov *et al.* in frustrated Heisenberg ferrimagnetic chains [165] for which a critical value of the frustration parameter produces a discontinuous transition from the long-range ferrimagnetic state to a singlet spiral state. So in our studied system we expect that the ground state is not a ferrimagnet. This is indeed the case as the following DMRG results show.

4.3.2 DMRG results at $T = 0$

We have studied the ground state properties of our system with the density matrix renormalization group algorithm. For this we used open boundary conditions in a chain of

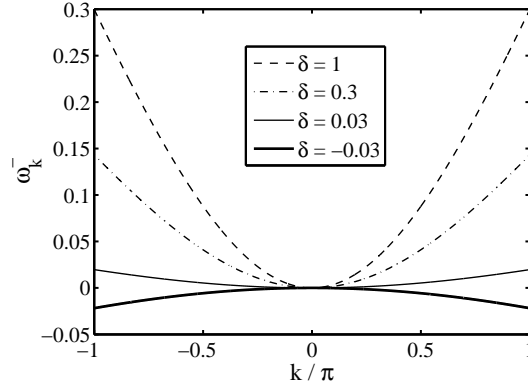


Figure 4.4: Low-energy excitations of the Hamiltonian (4.3.1) with $D = 0$, as δ decreases from the Heisenberg point and reaches a negative value. The branch ω_k^+ behaves in a similar way.

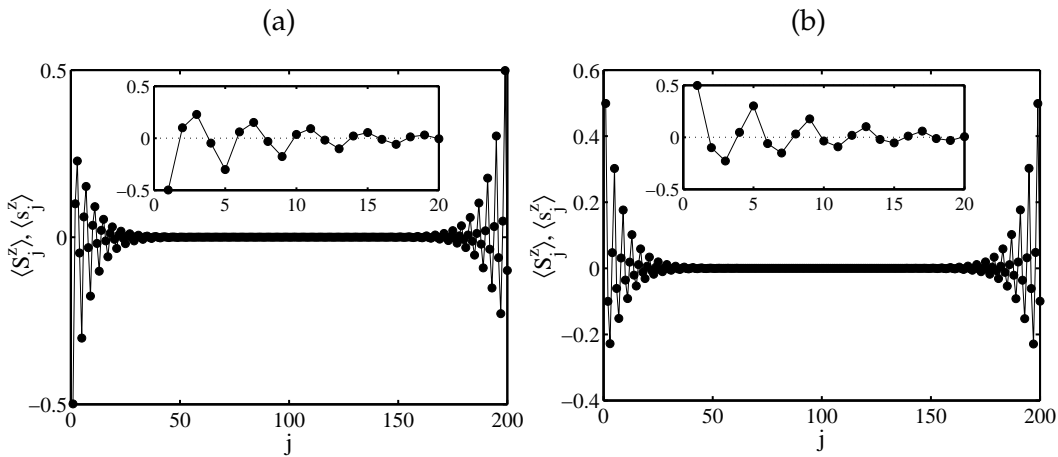


Figure 4.5: Expectation value of the z component of the site spin vs unit-cell index j (a) in the singlet ground state of the system (b) in a low-lying triplet state. The end oscillations decay exponentially to zero as we move towards the center of the chain.

200 sites, keeping up to 100 density matrix eigenstates, which maintained the truncation error less than 10^{-10} . The ground state energy per site converged to the value $E_0/2N = -0.630483 J$. We have targeted, in a 20-site chain, the lowest-energy state in each total spin sector S_T in order to investigate the low-energy spectrum of the system. When $D = 0$ we find a singlet ground state with a triplet just above it, since the energy of the ground state appears in both the sectors $S_T = 0$ and $S_T = 1$. Otherwise, when $D \neq 0$ there is a zero-field splitting and the ground state energy belongs only to the $S_g = 0$ sector. In this case we have checked that the structure of the low-lying energy levels follows the Lieb-Mattis theorem [21]: $E(S_T + 1) > E(S_T)$, $S_T \geq S_g$. With this we verified the assumption that the ground state of our system is not magnetized.

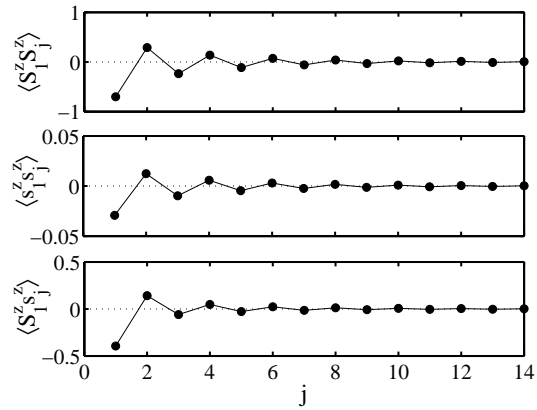


Figure 4.6: Spin-spin correlation functions vs distance between the first spin- S site and the other spin- S sites along the chain (upper panel), between the first spin- s site and the other spin- s sites along the chain (central panel), and between the first spin- S site and the spin- s in other unit cells (lower panel). Here we only show the most interesting region which is between the units cells 1 and 14.

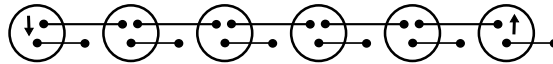


Figure 4.7: Proposed valence-bond representation of the ground state of our system. The bullet (arrow) symbol denotes a spin $1/2$ with its (fixed) unfixed projection value. The solid segment is a singlet pair (valence bond): $\uparrow\downarrow - \downarrow\uparrow$. The circle represents an operation of constructing a spin $3/2$ by symmetrizing the three spin $1/2$'s inside.

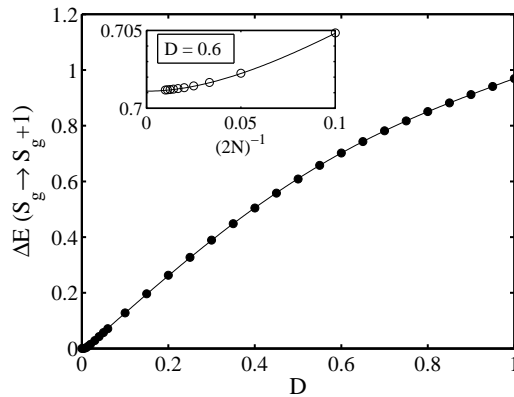


Figure 4.8: Energy gap (units of J) between the ground state and the lowest-lying excitation as a function of D . The effect of the single-ion anisotropy term is the zero-field separation between the singlet and the triplet states. The solid line is a 4th degree polynomial fit. The inset figure shows the extrapolation to the thermodynamic limit of the energy gap for a sample value $D = 0.6$ for which we obtain $\Delta E = 0.7009(5)J$.

In Fig. 4.5(a) we show the ground-state expectation value of the z component of the site spin along the chain, and in Fig. 4.5(b) the results in the lowest excitation which is one of the triplet states. We immediately note that the long-ranged Néel order is absent in the ground state as it was expected. The profile of expectation values reminds us that of the spin-1 antiferromagnetic Heisenberg chain [29] in which the open ends act as effective spin $1/2$ sites. As noted by Kennedy [166], these spin- $1/2$'s bind very weakly through the chain to form a singlet and a triplet just above it. The singlet is the ground state for even numbered chains, and the triplet is the ground state for odd numbered chains. In our system, the value of $\langle S_j^z \rangle$ on the end sites is $0.4987(3)$, slightly smaller than $1/2$, the result for real spin- $1/2$'s. We have observed that when the number of unit cells N is odd, the up-down configuration at the end spin- S sites is present in the ground state as opposed to the down-up configuration when N is even (the one shown). Here the chosen ground state depends on the parity of the number of unit cells instead of the number of sites, which seems to be the case for mixed-spin alternating chains [52]. The antiferromagnetic oscillations which accompany the end states in Fig. 4.5 decay exponentially from the edges. We have fitted $\ln |S_j^z|$, which is extremely linear away from the ends, taking independent values from the two exponential envelopes and have calculated an averaged value for the decay length: $\xi_d = 7.3(1)a$. The decay of the $\langle s_j^z \rangle$ values away from the ends is governed by the same averaged decay length. In order to compare this value with the correlation length of the system we calculate the two-spin correlation functions. Owing to the alternation of the spin- $3/2$ and spin- $1/2$ sites along the chain, one has to distinguish between $\langle S_1^z S_j^z \rangle$, $\langle s_1^z s_j^z \rangle$, and $\langle S_1^z s_j^z \rangle$ pair correlations. We show these calculated functions in Fig. 4.6. As can be seen, the correlations decay exponentially to zero as we move towards the center of the chain. An averaged correlation length can be calculated in a similar fashion as the decay length. For the $\langle S_1^z S_j^z \rangle$ and the $\langle s_1^z s_j^z \rangle$ functions we find $\xi = 6.6(1)a$, which can be compared with the correlation length for the spin-1 antiferromagnetic Heisenberg chain [28, 167] $\xi = 6.03(1)a$. For this latter case it was found $\xi = \xi_d$. In our system we do not have this equality although the results are not quite different. For the $\langle S_1^z s_j^z \rangle$ function we roughly see from the figure that the correlation length is slightly smaller.

The existence of a singlet ground state with effective spin- $1/2$ states at each spin- S end of our (S, s) open chain can be understood if we refer to the AKLT composite picture [130] shown in Fig 4.7. In this picture, each spin S is obtained by symmetrization of $2S$ spin- $1/2$ variables. Then a global singlet state for the whole chain can be written with $2S$ valence bonds emanating from each site and terminating on different sites. We remind that this kind of states can explain the oscillating exponential decay (see Fig. 4.6) of some spin-spin correlation functions, for example in a spin-1 valence-bond-solid state which is readily

obtained from Fig. 4.7 after removing all the lower spin-1/2 variables, it can be shown [130, 168] that for an infinite chain $\langle S_1^z S_j^z \rangle = 4/3(-1)^j e^{-j/\xi}$ with $\xi = 1/\ln 3$.

The similarities of the present system with the spin-1 antiferromagnetic Heisenberg chain (a full analogy will be given later) are easy to understand if we remember that the value of $|\delta|$ is quite small compared with J which allows the system to be very close to (but not in) the decoupled-dimer limit, in which intradimer antiferromagnetic interactions establish effective spin-1 objects at each unit cell. We will show that slight deviations from this limit are necessary to explain the low-temperature properties of the system.

Now that we are convinced that our system is far from being a ferrimagnet, although it is an alternating mixed-spin chain compound with mainly antiferromagnetic interactions, we come into the description of the low-temperature properties arisen from the low-energy excitations from the ground state. Before doing so, we inquire into the effect of the D term on these low-energy excitations. For this purpose we calculate the gap, in the 200-site chain, between the ground state energy, which is in the $S_T = S_g = 0$ sector, and the lowest energy in the $S_T = 1$ sector; this is shown in Fig 4.8. A very interesting conclusion can be drawn from this figure, namely, the existence of a gap (in addition to the antiferromagnetic gap) which increases with increasing D should give rise to a low-temperature extra peak (in addition to the Schottky-like peak) in the specific heat, which moves to the high temperature region as D increases. This double-peak structure of the specific heat has been shown to occur in several low-dimensional systems and the different mechanisms for this to occur are a hot matter of current interest in condensed matter physics [84, 170–175].

4.3.3 Specific heat and magnetic susceptibility

We have performed exact-diagonalization of the full Hamiltonian under periodic boundary conditions for system sizes ranging from 4 to 8 without observing substantial differences and thus we show the results for a cluster of $2N = 6$ sites. As we expected from the DMRG results there appears a low-temperature peak in the specific heat (see Fig. 4.9(a)) which moves to the high temperature region as D is increased. While this happens, the pseudo-plateau in the $\chi_M T$ vs T curve begins to disappear as may be seen in Fig. 4.9(b), giving rise to an antiferromagnetic low-dimensional behavior in which the $\chi_M T$ product decreases continuously upon cooling [176]. This is quite reasonable because as we increase D the singlet-to-triplet gap gets closer and closer to the antiferromagnetic gap which produces the Schottky-like peak in the specific heat, and thus an antiferromagnetic behavior is expected. It is remarkable, as is shown in Fig. 4.10(a), that a low-temperature peak is also found in the specific heat (even when $\delta > 0$) if the dimerization parameter is decreased

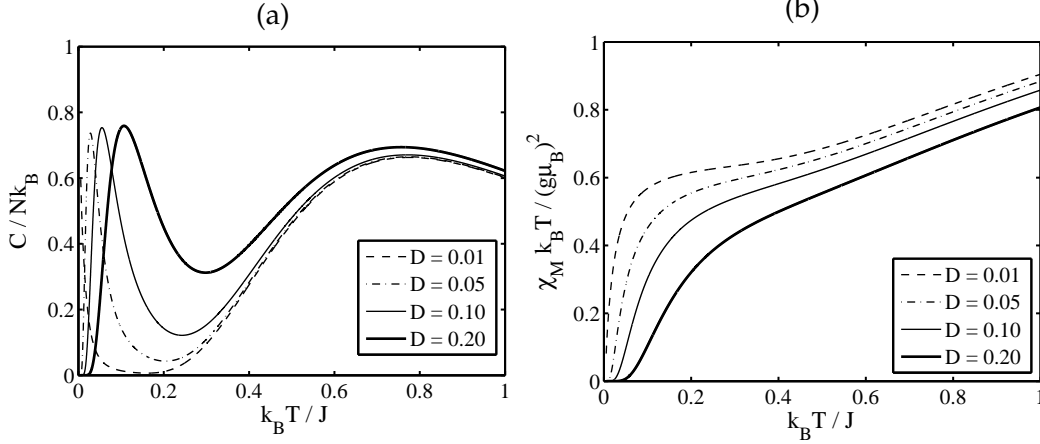


Figure 4.9: (a) Effect of the D term in the specific heat of the system (in dimensionless units). As predicted from DMRG calculations the low-temperature extra peak moves to the high temperature region as we increase D . (b) Effect of the D term in the $\chi_M T$ product (in dimensionless units). As D increases the pseudo-plateau is gradually destroyed, giving rise to an antiferromagnetic low-dimensional behavior.

from the Heisenberg point with $D = 0$. In the decoupled-dimer limit ($\delta = 0$) this peak disappears as it is shown in Fig. 4.10(a). Then we believe that a gap $\Delta_{k=0}^-$, which is not described by the present *linear* spin wave theory, is opened by dimerization. We notice that our spin-wave results do predict a linear δ -dependence of the antiferromagnetic gap $\Delta_{k=0}^+$, in agreement with DMRG calculations for the $(S, s) = (1, 1/2)$ spin chain [55]. When the interdimer interaction is ferromagnetic ($\delta < 0$), the position of the peak moves to the low-temperature region and its height increases considerably, as can be seen in the inset figure.

Although the zero-field splitting of the ground state induces a decrease of the $\chi_M T$ values at low temperatures with $\delta > 0$, as may be seen in Fig. 4.10(b) for the case $\delta = 0.3$ and $D = 0.001$, it does not explain the pseudo-plateau observed before the triggering of this rapid decay. Thus the ferromagnetic nature of interdimer interactions is completely necessary to explain the low-temperature properties of our studied system (compare with the case $\delta = -0.03$ and $D = 0$). The pseudo-plateau in the curve indicates a quasi-paramagnetic behavior in which the classical Curie law for the magnetic susceptibility is a good approximation. In the non-interacting-dimer limit discussed before, the system *is* actually an effective paramagnet. Within this limit it can be shown [1] that $\chi_M k_B T / (g\mu_B)^2 \approx S(S+1)/3$ (see also Eq. (4.1.4) with $s = 0$) where we have assumed that the orbital contribution to the magnetic moments is negligible. Then, if we take the discussed effective value $S = 1$ at each unit cell we obtain $\chi_M k_B T / (g\mu_B)^2 \approx 0.6667$ which coincides exactly with the constant value shown in Fig. 4.10(b) for the case $\delta = 0$ (para-

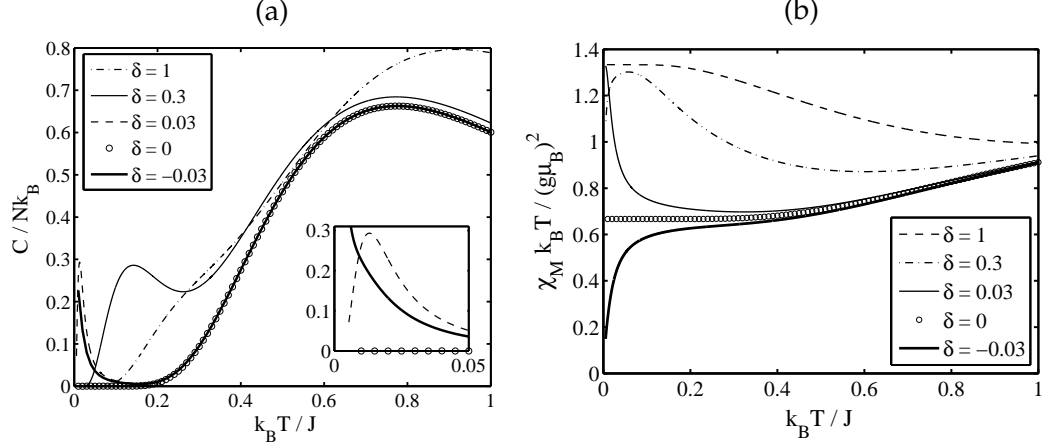


Figure 4.10: (a) Variation of the specific heat vs T (in dimensionless units) as δ decreases, with $D = 0$, from the Heisenberg point and reaches a negative value. A double-peak structure induced by dimerization can be seen. (b) Variation of the $\chi_M T$ vs T curve (in dimensionless units) as δ decreases, with $D = 0$, from the Heisenberg point and reaches a negative value. Then a pseudo-plateau and a rapid decrease at low temperatures can be seen. The dashed-dotted line represents the case $\delta = 0.3$ and $D = 0.001$.

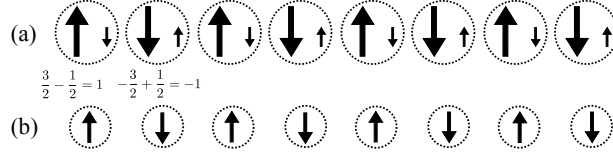


Figure 4.11: Effective picture of our dimerized chain at low temperatures. The scaled arrows represent the magnitudes of spins $3/2$, 1 , and $1/2$. (a) Interdimer ferromagnetic interactions make the spins in the bonds align parallel to each other. (b) Together with the strong intradimer antiferromagnetic interactions, the interdimer ferromagnetic interactions produce an antiferromagnetic ordering of the effective spin-1 ions at each unit cell.

magnetic case), around which the pseudo-plateau develops. Note that this limit is valid at high enough temperatures where the thermal fluctuations predominate over the interdimer interactions. For low enough temperatures (below $0.2J/k_B$ in the present case) the ferromagnetic bonds begin to unveil and nearest neighbors at the ends of these bonds tend to align parallel to each other as shown in Fig. 4.11(a). Since the intradimer interactions are strong antiferromagnetic forces, the unit cells still behave as effective $S = 1$ spins. Then as a result of this bond alternation the system is effectively described by a chain of spin-1 ions ordered antiferromagnetically as shown in Fig. 4.11(b). This qualitative picture explains the decay to zero of the $\chi_M T$ vs T curve at low temperatures, as it should be for antiferromagnets due to the nonmagnetic ground state. Therefore we conclude that slight variations from the decoupled-dimer limit with interdimer ferromagnetic interactions are

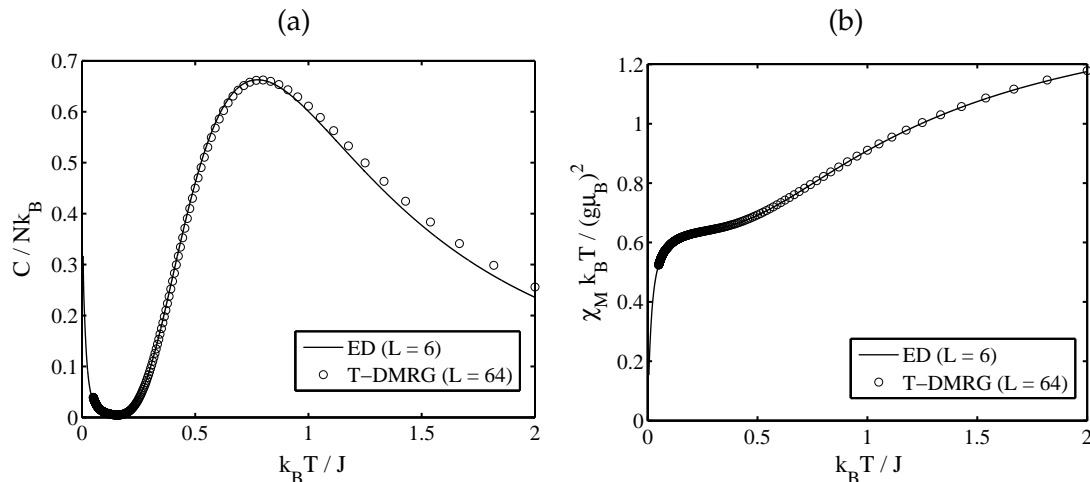


Figure 4.12: Specific heat (a) and $\chi_M T$ (b) vs T curves (in dimensionless units) of the dimerized chain compound for the values $\delta = -0.0277$ and $D = 0.0011$, using exact diagonalization (ED) compared with the ancilla T-DMRG results.

necessary to explain the observed $\chi_M T$ vs T curve at low temperatures of our dimerized quantum mixed-spin chain. We have checked, as can roughly be seen when comparing Figs. 4.10(a) and 4.10(b), that the temperature from which the rapid decay in this curve is observed to be triggered when cooling, coincides with the temperature from which the specific heat starts to climb the extra peak (that of the local minimum), which suggests that the mechanism which opens the $\Delta_{k=0}^-$ gap when $\delta < 0$ is intimately related with the formation of the antiferromagnetic (Haldane) gap of the effective spin-1 system. In Fig. 4.12 we show one of results of the present calculations using exact diagonalization (ED) compared with the results using the ancilla T-DMRG algorithm described in the former section. We observe that the thermodynamic limit is indeed reproduced with the ED calculations, i.e. the thermal properties in this system are not vulnerable at all to finite size effects. With this, we think to have reached our initial goal of *clarifying* the role of δ and D in the observed low-temperature properties of our dimerized mixed-spin quantum chain compound.

In summary, we have discussed the common features of the thermal properties of quantum ferrimagnets, in which the $\chi_M T$ product decreases upon cooling, shows a rounded minimum at mid temperatures and then increases at low temperatures; and the specific heat shows a sharp Schottky-like peak at mid temperatures. Then we have investigated the unconventional low-temperature properties of a dimerized antiferromagnetic-ferromagnetic mixed $(S, s) = (3/2, 1/2)$ alternating chain. Using a spin-wave argument we have seen that the ferromagnetic interdimer interactions in this system enforces the need for a depar-

ture of the otherwise expected ferrimagnetic ground state in the system. The ground state properties are studied using the density matrix renormalization group algorithm, which corroborates the spin-wave predictions and give evidence for a singlet ground state with a triplet just above it. The presence of single-ion anisotropy on the spin-3/2 sites produces a zero-field splitting of these energy levels which is observed as a low-temperature extra peak in the specific heat. A slight deviation from the decoupled-dimer picture with effective spin-1 sites at each unit cell gives a satisfactory explanation of the pseudo-plateau appearing in the $\chi_M T$ vs T curve and the rapid decrease of this product, investigated with exact-diagonalization of a finite cluster, is attributed to the ferromagnetic nature of the dimerization parameter. Here we emphasize on the properties of a particular real system but give an overview of what might happen in general mixed-spin quantum chains with antiferromagnetic-ferromagnetic bond alternation.

Conclusions and outlook

We have investigated some open questions in the physics of mixed-spin chains using the density matrix renormalization group (DMRG), and its extensions to study dynamics (t-DMRG) and thermal properties (T-DMRG), as the main numerical technique. We showed that in mixed (S, s) Ising spin chains with single-ion anisotropy there appears $2s + 1$ plateaux in the magnetization curve which generalizes to mixed-spin chains the well-known results for Ising spin- S chains where the system exhibits $2S + 1$ plateaux. We also prove the validity of the spin-wave theory for quantum Heisenberg chains with crystal-field anisotropy in the easy-axis regime, which could be of vital importance for theoretical investigations on the low-temperature behavior of these systems. The use of measures of entanglement to determine quantum critical points in a mixed-spin chain was also investigated, showing that the purity and negativity are suitable measures to signal the quantum phase transition which appear in the $(S, s) = (1, 1/2)$ Heisenberg system with crystal-field anisotropy. We also inquired into the time evolution of a state prepared in mixed-spin XX chain as well as the corresponding dynamics of entanglement entropy, which displayed interesting features of practical importance in the transport of bitwise information in magnetic nanostructures. The ferrimagnetic properties common to all Heisenberg mixed-spin chains at finite temperature, regardless of the spin mixture in the unit cell, were also studied, and we discussed unconventional features of a recently synthesized material where the magnetic properties deviate from the expected ferrimagnetic behavior.

Last year, Barthel *et al.* [177] combined the adaptive t-DMRG with the ancilla T-DMRG to study, for the first time, dynamics of one-dimensional quantum systems at finite temperature. The problem they solved was the following: real-time simulations are plagued by the same limitations as at zero temperature, namely, the propagation of excitations through the system which leads to entanglement growth in the purified state. As entanglement entropy is related roughly exponentially to DMRG resources, this strongly limits achievable simulation times, or inversely the ω -resolution for spectral functions, as those are derived by Fourier transformation from the real-time data. Therefore, in order to overcome

this limitation at very low numerical cost, they adapted a linear prediction technique to extrapolate data beyond the run-away time. They could reproduce, with a surprising accuracy, the exact results known for the structure factors of XX spin-1/2 chains, and the Bethe ansatz together with quantum Monte Carlo data for the isotropic Heisenberg chain. Since there are no related work for mixed-spin chains, this motivates us to investigate the dynamics of mixed-spin chains at finite temperature. The only thing which we have to implement, as an extra code in our programs, is the linear prediction technique. This will allow us to study quantities such as optical conductivity in mixed-spin chains at finite temperature, which can be compared directly with already existing experimental results.

Recent DMRG algorithms at $T > 0$

In this appendix we describe, in the order they were developed, the most up-to-date DMRG algorithms for finite temperatures. They all rest upon the same basis (including the one presented in chapter 4): building a thermal state $|\psi\rangle = e^{-\beta\mathcal{H}/2}|\psi^*\rangle$ at inverse temperature $\beta^{-1} = k_B T$, $|\psi^*\rangle$ being some initial state, such that we can extract the partition function from $\langle\psi|\psi\rangle$ in some way. It is worthy to mention that the DMRG algorithm was adapted to calculate the transfer matrix of 1D quantum systems. In the transfer-matrix DMRG method [178, 179], the usual DMRG sweeping takes place in the imaginary time direction, whereas the thermodynamic limit in one spatial direction is automatically obtained by targeting the maximum transfer matrix eigenvalue and eigenvector. This algorithm gives excellent results, but is also technically more difficult to implement, in part because the transfer matrix is non-Hermitian. Here we do not give details about this method; we only describe the most recent DMRG algorithms. We start with the description of a finite-temperature algorithm which has more in common with the standard DMRG algorithm at $T = 0$ and works very well for low temperatures.

A.1 Regulated polynomial expansion

Two years ago, Sota and Tohyama [161] proposed a scheme of DMRG at finite temperatures, which is a straightforward extension of the target-state procedure at zero temperature. The target state is weighted by a Boltzmann factor. Making use of a polynomial expansion and a random sampling, they could calculate static and dynamical quantities at finite temperature. Since in order to obtain good convergence at high temperature, a large truncation number of the density matrix is needed, the method is more suitable for low temperatures.

The DMRG procedure at zero temperature requires a target state in order to obtain the ground-state properties. Even for finite temperatures, it is possible to have a target state suitable for the evaluation of physical quantities. A possible target state is

$$|\tilde{\xi}\rangle = e^{-\beta\hat{H}/2}|\xi\rangle = \sum_{n=1}^{\mathcal{D}} e^{-\beta E_n/2} a_n |\psi_n\rangle, \quad (\text{A.1.1})$$

where $|\xi\rangle$ is a normalized arbitrary vector, \mathcal{D} is the dimension of the superblock, and the coefficient $a_n = \langle \psi_n | \xi \rangle$. The amplitude of this target state is $\langle \tilde{\xi} | \tilde{\xi} \rangle = \sum_n a_n^2 e^{-\beta E_n}$. Then, provided that $a_n^2 = 1$, the partition function can be calculated as $Z(\beta) = \langle \tilde{\xi} | \tilde{\xi} \rangle$. The essence of this method is to evaluate the exponential operator without decomposing it with a Suzuki-Trotter formula. Instead they expand the delta function in terms of Legendre polynomials $\delta(\epsilon - \tilde{E}_n) = \sum_{l=0}^{\infty} w_l^{-1} P_l(\epsilon) P_l(\tilde{E}_n)$, with $w_l = 2/(2l+1)$, and evaluate

$$e^{-\beta\tilde{E}_n/2} = \int_{-1}^1 e^{-\beta\epsilon/2} \delta(\epsilon - \tilde{E}_n) d\epsilon = \int_{-1}^1 e^{-\beta\epsilon/2} \sum_{l=0}^{\infty} w_l^{-1} P_l(\epsilon) P_l(\tilde{E}_n) d\epsilon, \quad (\text{A.1.2})$$

where \tilde{E}_n is an energy eigenvalue rescaled to be confined within the interval $[-1,1]$, being $\hat{\mathcal{H}}_s = w_H(\hat{H} - \lambda)$ the corresponding rescaled Hamiltonian, with scaling parameters w_H and λ . In general, there appears the so-called Gibbs oscillations in any polynomial expansion. Fortunately, these oscillations can be eliminated by regulating the $P_l(\tilde{E}_n)$ with the Gaussian distribution function through

$$\langle P_l(\tilde{E}_n) \rangle_{\sigma} = \frac{1}{\sqrt{2\pi\sigma^2}} \int_{-1}^1 e^{-(\epsilon - \tilde{E}_n)^2/2\sigma^2} P_l(\epsilon) d\epsilon, \quad (\text{A.1.3})$$

where σ is the half width of the Gaussian distribution set to be $2\pi/l_m$, with l_m denoting the highest number of l in the expansion. Then, inserting the Boltzmann factor (Eq. (A.1.2)) into the target state (Eq. (A.1.1)), they obtained, after the integration with respect to ϵ (which leads to the modified spherical Bessel functions $i_l(x)$ of the first kind),

$$|\tilde{\xi}\rangle \simeq C(\beta) \sum_{l=0}^{l_m} w_l^{-1} i_l(-\beta/2) \langle P_l(\hat{\mathcal{H}}_s) \rangle_{\sigma} |\xi\rangle, \quad (\text{A.1.4})$$

where $C(\beta)$ is a normalization constant, and we have returned to the operator representation. In order to calculate $\langle P_l(\hat{\mathcal{H}}_s) \rangle_{\sigma} |\xi\rangle$ they employed a coalitional recursive relation which reduces to matrix-vector multiplications of the form $\hat{\mathcal{H}}|\xi\rangle$.

In the DMRG method, physical quantities are measured when the system size is reached to a given number in the infinite-system algorithm or enough convergency is obtained in the finite-system algorithm. At this stage, Sota and Tohyama introduced a technique to guarantee the relation $a_n^2 = 1$ for the coefficients in Eq. (A.1.1). They achieved this by

taking a random sampling of the state $|\tilde{\zeta}\rangle$ and averaging over the samplings. That is, we start by representing the randomly generated state as $|\tilde{\zeta}\rangle = \sum_i r_i |\zeta_i\rangle$, where $|\zeta_i\rangle$ is the basis state of the system and r_i is a normalized random number within the interval $[-1,1]$. Then we expand the energy eigenvectors as $|\psi_n\rangle = \sum_i b_{n,i} |\zeta_i\rangle$, so that the coefficients a_n can be expressed as $a_n^2 = \sum_i r_i^2 b_{n,i}^2 + 2 \sum_{i \neq j} r_i r_j b_{n,i} b_{n,j}$. After averaging over many samplings (M of them), r_i^2 will become a constant approximately independent of i , and $r_i r_j$ will vanish according to $1/\sqrt{m^2 M}$. Therefore, a relation a_n^2 is expected to be satisfied for each n . With this procedure, the expectation value of an operator \hat{A} is given by

$$\langle \tilde{\zeta} | \hat{A} | \tilde{\zeta} \rangle = \sum_n a_n^2 e^{-\beta E_n} \langle \psi_n | \hat{A} | \psi_n \rangle + \sum_{n \neq m} a_n a_m e^{-\beta(E_n + E_m)/2} \langle \psi_m | \hat{A} | \psi_n \rangle. \quad (\text{A.1.5})$$

But, following the above argument, $a_n a_m = \sum_i r_i^2 b_{n,i} b_{m,i} + 2 \sum_{i \neq j} r_i r_j b_{n,i} b_{m,j} \simeq \langle \psi_n | \psi_m \rangle = 0$, and $a_n^2 \simeq 1$, after the random sampling and averaging. Then the thermodynamic average can be obtained as

$$\langle \hat{A} \rangle_\beta = \frac{\sum_n e^{-\beta E_n} \langle \psi_n | \hat{A} | \psi_n \rangle}{\sum_n e^{-\beta E_n}} = \frac{\langle \tilde{\zeta} | \hat{A} | \tilde{\zeta} \rangle}{\langle \tilde{\zeta} | \tilde{\zeta} \rangle}. \quad (\text{A.1.6})$$

For the Hubbard chain at half filling studied by Sota and Tohyama, the method was shown to give very accurate results at low temperatures. However, they always consider small systems in order to compare with exact diagonalization. With the collaboration of Sota, we were able to implement this method for our mixed-spin chains. Now we are running, for the first time, the algorithm for these systems in order to test its suitability for the large systems typically considered in a standard DMRG calculation.

A.2 Minimally entangled typical thermal states

Last year, White proposed a finite-temperature method [162] which is more efficient than those mentioned before, although the idea is similar. He assumed the existence of a set of states $\{|\psi(i)\rangle\}$, which he called minimally entangled typical thermal states (METTS), with unnormalized probabilities $P(i)$ from which we can select these states at random in order to calculate expectation values of relevant operators. Let us see how to build METTS.

For any orthonormal set $\{|i\rangle\}$, the thermal density matrix can be written as

$$\rho_\beta = e^{-\beta \mathcal{H}} = e^{-\beta \mathcal{H}/2} \sum_i |i\rangle \langle i| e^{-\beta \mathcal{H}/2}. \quad (\text{A.2.1})$$

This can be expressed as a convex sum

$$\rho_\beta = \sum_i P(i) |\psi(i)\rangle \langle \psi(i)|, \quad (\text{A.2.2})$$

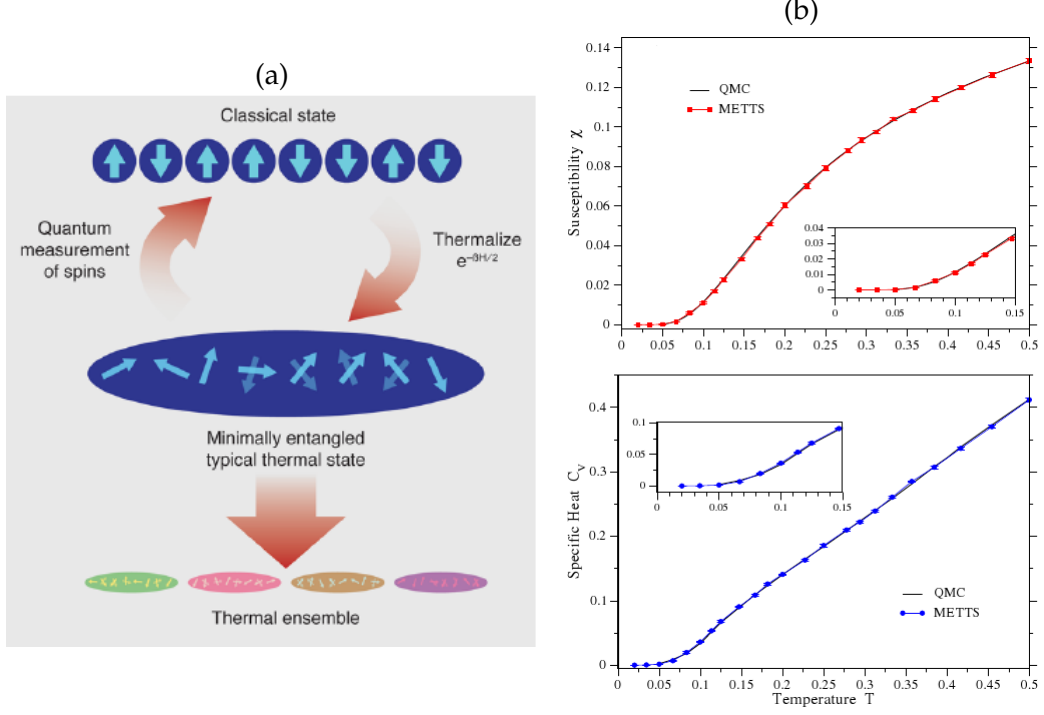


Figure A.1: (a) Representation of the METTS algorithm (taken from Ref. [180]). The algorithm begins with a classical state. Minimally entangled typical thermal states (METTS) are created by evolving a classical state in imaginary time. Subsequently, by performing a quantum measurement on the METTS, a new classical state is created and the circles closes. After discarding the first few METTS produced from this loop in order to erase any memory of the initial choice, an ensemble of only a few states allows calculation of static quantities with high accuracy. (b) Susceptibility and specific heat at low temperatures of the spin-1 Heisenberg chain with 100 sites using the METTS algorithm (taken from Ref. [181]) compared with QMC.

provided the states $|\psi(i)\rangle$ are defined as

$$|\psi(i)\rangle = \frac{1}{\sqrt{P(i)}} e^{-\beta\mathcal{H}/2} |i\rangle, \quad \text{with } P(i) = \langle i | e^{-\beta\mathcal{H}} | i \rangle. \quad (\text{A.2.3})$$

The essence of the method is to choose classical product states (CPS) as the basis states $|i\rangle = \prod_{\text{sites } l} |i_l\rangle$, where i_l labels the state of a site in the chain. Since these states are not entangled, it is expected that the application of the exponential operator onto them (Eq. (A.2.3)) generates minimally entangled states. Note that the partition function can be calculated as $Z(\beta) = \sum_i P(i)$, and then thermodynamic averages are taken over the ensemble of METTS:

$$\langle A \rangle_\beta = Z^{-1} \sum_i P(i) \langle \psi(i) | A | \psi(i) \rangle. \quad (\text{A.2.4})$$

A natural question is, how do we generate an ensemble of METTS for a given tempera-

ture? White answers this question by analogy to the updates in Monte Carlo steps: the last METTS is used to produce the next CPS (and from there the next METTS) by a quantum measurement of all the spins in the chain. How do we do this? A physical measurement projects the wave function into one eigenstate of the measured operator, with the appropriate probability. For example, to measure one particular spin in the z direction in a spin-1/2 chain, we have to compute the probabilities $P(\uparrow) = \langle S^z \rangle + \frac{1}{2}$, $P(\downarrow) = 1 - P(\uparrow)$, and then roll the dice (random number generator which chooses either $|\uparrow\rangle$ or $|\downarrow\rangle$ according to the calculated probabilities). Say the spin stayed at $|\uparrow\rangle$ after the measurement. Then, the wave function (METTS) collapses as $|\psi\rangle \rightarrow P(\uparrow)^{-1/2}|\uparrow\rangle\langle\uparrow|\psi\rangle$. With this procedure we measure all the spins taking one half-sweep in DMRG. It can be shown [181] that the probability of the final CPS $|i'\rangle$ is given by $P(i')$ as in Eq. (A.2.3). Note that the application of the exponential operator is performed as an imaginary-time evolution, just as in the case of the ancilla algorithm. In Fig. A.1(a) we show a schematic representation (taken from Ref. [180]) of the present algorithm. We are in a final stage of the implementation of this algorithm, since it is very accurate and requires less computational cost. Moreover it is able to reach significantly lower temperatures than with previous DMRG-based finite temperature methods. For example, with the ancilla T-DMRG, Feiguin and White were able to simulate the spin-1 Heisenberg chain down to about $T = 0.05$, where about $m = 500$ states had to be kept at the lowest temperatures when using a truncation cutoff of 10^{-10} . In contrast, to reach comparable temperatures using METTS requires only about $m = 60$ states when using the same cutoff. Stoudenmire and White [181] were able to produce accurate results down to at least $T = 0.02$, as we show in Fig. A.1(b) for the susceptibility and the specific heat, which are in excellent agreement with the quantum Monte Carlo.

Bibliography

- [1] S. Blundell, *Magnetism in Condensed Matter* (Oxford University Press, 2001).
- [2] I. Bose, arXiv: cond-mat/0107399 (2001).
- [3] L. J. de Jongh and A. R. Miedema, *Adv. Phys.* **23**, 1 (1974).
- [4] P. W. Anderson, *Phys. Rev.* **86**, 694 (1952).
- [5] R. Kubo, *Phys. Rev.* **87**, 568 (1952).
- [6] H. Bethe, *Z. Phys.* **71**, 205 (1931).
- [7] E. Lieb, T. Schultz, and D. Mattis, *Ann. Phys. (N.Y.)* **16**, 407 (1961).
- [8] F. D. M. Haldane, *Phys. Rev. Lett.* **93 A**, 464 (1983).
- [9] F. D. M. Haldane, *Phys. Rev. Lett.* **50**, 1153 (1983).
- [10] H. J. Blote and M. P. Nightingale, *Phys. Rev. B* **33**, 659 (1986).
- [11] W. Buyers et al., *Phys. Rev. Lett.* **56**, 371 (1986).
- [12] H. J. Schulz and T. Ziman, *Phys. Rev. B* **33**, 6545 (1986).
- [13] M. Oshikawa, M. Yamanaka, and I. Affleck, *Phys. Rev. Lett.* **78**, 1984 (1997).
- [14] D. C. Cabra et al., arXiv: cond-mat/0010376v1 (2000).
- [15] D. C. Mattis, *The theory of magnetism made simple: an introduction to physical concepts and to some useful mathematical methods* (World Scientific, Singapore, 2006).
- [16] R. Feynherm, C. Mathonière, and O. Kahn, *J. Phys.: Condens. Matter* **13**, 2639 (2001).
- [17] O. Kahn, *Magnetism of the Heteropolymetallic Systems* (Springer-Verlag, Berlin, 1987).
- [18] M. Drillon et al., *Phys. Rev. B* **40**, 10992 (1989).

BIBLIOGRAPHY

- [19] P. J. van Koningsbruggen et al., *Inorg. Chem.* **29**, 3325 (1990).
- [20] W. Marshall, *Proc. Roy. Soc. (London)* **A232**, 48 (1955).
- [21] E. Lieb and D. Mattis, *J. Math. Phys.* **3**, 749 (1962).
- [22] K. Wilson, *Rev. Mod. Phys.* **47**, 773 (1975).
- [23] J. W. Bray and S. T. Chui, *Phys. Rev. B* **1979**, 4876 (1979).
- [24] C. Y. Pan and X. Chen, *Phys. Rev. B* **36**, 8600 (1987).
- [25] M. D. Kovarik, *Phys. Rev. B* **41**, 6889 (1990).
- [26] T. Xiang and G. A. Gehring, *J. Magn. Magn. Mater.* **104-107**, 861 (1992).
- [27] S. R. White and R. M. Noack, *Phys. Rev. Lett.* **68**, 3486 (1992).
- [28] S. R. White, *Phys. Rev. Lett.* **69**, 2863 (1992).
- [29] S. R. White, *Phys. Rev. B* **48**, 10345 (1993).
- [30] U. Schollwöck, *Rev. Mod. Phys.* **77**, 259 (2005).
- [31] K. A. Hallberg, *Adv. Phys.* **55**, 477 (2006).
- [32] R. P. Feynman, *Statistical Physics: A set of Lectures* (Bejaming, Reading, MA, 1972).
- [33] O. Legeza and G. Fáth, *Phys. Rev. B* **53**, 14349 (1996).
- [34] K. Hida, *J. Phys. Soc. Jpn.* **63**, 2359 (1994).
- [35] K. Totsuka, *Phys. Rev. B* **57**, 3454 (1998).
- [36] T. Sakai and M. Takahashi, *Phys. Rev. B* **57**, R3201 (1998).
- [37] T. Tonegawa et al., *J. Phys. Soc. Jpn.* **65**, 3317 (1996).
- [38] T. Yamamoto, M. Asano, and C. Ishii, *J. Phys. Soc. Jpn.* **69**, 3965 (2000).
- [39] T. Sakai and S. Yamamoto, *Phys. Rev. B* **60**, 4053 (1999).
- [40] T. Tonegawa et al., *J. Phys.: Conference Series* **51**, 171 (2006).
- [41] T. Sakai and S. Yamamoto, *J. Phys.: Condens. Matter* **12**, 9787 (2000).
- [42] S. Yamamoto and T. Sakai, *Phys. Rev. B* **62**, 3795 (2000).

BIBLIOGRAPHY

- [43] T. Kaneyoshi and Y. Nakamura, *J. Phys.: Condens. Matter* **10**, 3003 (1998).
- [44] T. Kaneyoshi et al., *J. Phys.: Condens. Matter* **10**, 7025 (1998).
- [45] X. Y. Chen et al., *J. Magn. Magn. Mater.* **262**, 258 (2003).
- [46] F. Litaiff, J. R. de Sousa, and N. S. Branco, *Solid State Commun.* **147**, 494 (2008).
- [47] C. Ekiz and H. Yaraneri, *J. Magn. Magn. Mater.* **318**, 49 (2007).
- [48] E. Aydiner, *Chin. Phys. Lett.* **21**, 2289 (2004).
- [49] H. A. Kramers and G. H. Wannier, *Phys. Rev.* **60**, 252 (1941).
- [50] H. A. Kramers and G. H. Wannier, *Phys. Rev.* **60**, 263 (1941).
- [51] L. Onsager, *Phys. Rev.* **65**, 117 (1944).
- [52] E. Solano-Carrillo et al., *J. Magn. Magn. Mater.* **322**, 1917 (2010).
- [53] F. C. Alcaraz and A. L. Malvezzi, *J. Phys. A: Math. Gen.* **30**, 767 (1997).
- [54] G.-S. Tian, *Phys. Rev. B* **56**, 5355 (1997).
- [55] S. K. Pati, S. Ramasesha, and D. Sen, *Phys. Rev. B* **55**, 8894 (1997).
- [56] S. K. Pati, S. Ramasesha, and D. Sen, *J. Phys.: Condens. Matter* **9**, 8707 (1997).
- [57] T. Ono, T. Nishimura, M. Katsumura, T. Morita, and M. Sugimoto, *J. Phys. Soc. Jpn.* **66**, 2576 (1997).
- [58] H. Niggemann, G. Uimin, and J. Zittartz, *J. Phys.: Condens. Matter* **9**, 9031 (1997).
- [59] H. Niggemann, G. Uimin, and J. Zittartz, *J. Phys.: Condens. Matter* **10**, 5217 (1998).
- [60] T. Kuramoto, *J. Phys. Soc. Jpn.* **67**, 1762 (1998).
- [61] T. Kuramoto, *J. Phys. Soc. Jpn.* **68**, 1813 (1999).
- [62] S. K. Pati and R. R. P. Singh, *Phys. Rev. B* **60**, 7695 (1999).
- [63] S. Yamamoto, S. Brehmer, and H.-J. Mikeska, *Phys. Rev. B* **57**, 13610 (1998).
- [64] S. Yamamoto and T. Fukui, *Phys. Rev. B* **57**, R14008 (1998).
- [65] S. Brehmer et al., *J. Phys.: Condens. Matter* **9**, 3921 (1997).
- [66] S. Yamamoto et al., *J. Phys.: Condens. Matter* **10**, 11033 (1998).

BIBLIOGRAPHY

- [67] A. K. Kolezhuk, H.-J. Mikeska, K. Maisinger, and U. Schollwöck, *Phys. Rev. B* **59**, 13565 (1999).
- [68] C. Wu, B. Chen, X. Dai, Y. Yu, and Z.-B. Su, *Phys. Rev. B* **60**, 1057 (1999).
- [69] S. Yamamoto, *Phys. Rev. B* **61**, R842 (2000).
- [70] S. K. Pati, *Phys. Rev. B* **67**, 184411 (2003).
- [71] S. Mohakud, S. K. Pati, and S. Miyashita, *Phys. Rev. B* **76**, 014435 (2007).
- [72] J. S. Miller and M. Drillon, eds., *Magnetism: Molecules to Materials*, vol. 4 (Wiley-VCH, 2002).
- [73] S. K. Pati and C. N. R. Rao, *Chem. Commun.* p. 4683 (2008).
- [74] S. Mandal, S. K. Pati, M. A. Green, and S. Natarajan, *Chem. Mater.* **17**, 2912 (2005).
- [75] O. Kahn, Y. Pei, and Y. Journaux, *Inorganic Materials* (Wiley-New York, 1995).
- [76] A. Caneschi, D. Gatteschi, J. P. Renard, P. Rey, and R. Sessoli, *Inorg. Chem.* **28**, 1976 (1989).
- [77] A. Caneschi, D. Gatteschi, J. P. Renard, P. Rey, and R. Sessoli, *Inorg. Chem.* **28**, 2940 (1989).
- [78] D. Shiomi, M. Nishizawa, K. Sato, T. Takui, K. Itoh, H. Sakurai, A. Izuoka, and T. Sugawara, *J. Phys. Chem. B* **101**, 3342 (1997).
- [79] M. Nishizawa, D. Shiomi, K. Sato, T. Takui, K. Itoh, H. Sawa, R. Kato, H. Sakurai, A. Izuoka, and T. Sugawara, *J. Phys. Chem. B* **104**, 503 (2000).
- [80] N. B. Ivanov, *Phys. Rev. B* **57**, R14024 (1998).
- [81] M. Hagiwara, K. Minami, Y. Narumi, K. Tatani, and K. Kindo, *J. Phys. Soc. Jpn.* **67**, 2209 (1998).
- [82] L. Zhou and Y. Kawazoe, *J. Phys. A: Math. Gen.* **32**, 6687 (1999).
- [83] T. Holstein and H. Primakoff, *Phys. Rev.* **58**, 1098 (1940).
- [84] T. Nakanishi and S. Yamamoto, *Phys. Rev. B* **65**, 214418 (2002).
- [85] S. Yamamoto, *Solid State Phys.* **38**, 332 (2003).
- [86] B. d'Espagnat, *Conceptual Foundations of Quantum Mechanics* (Reading, MA, 1976).

BIBLIOGRAPHY

- [87] A. Einstein et al., *Phys. Rev.* **47**, 777 (1935).
- [88] E. Schrödinger, *Naturwissenschaften* **23**, 807 (1935).
- [89] J. S. Bell, *Physics* **1**, 194 (1964).
- [90] C. Bennett et al., *Phys. Rev. Lett.* **70**, 1895 (1993).
- [91] A. Barenco et al., *Phys. Rev. Lett.* **74**, 4083 (1995).
- [92] M. Nielsen and I. Chuang, *Quantum Computation and Quantum Communication* (Cambridge University Press, Cambridge, 2000).
- [93] A. Osterloh et al., *Nature* **416**, 608 (2002).
- [94] L. Amico et al., *Rev. Mod. Phys.* **80**, 517 (2008).
- [95] T. J. Osborne and M. A. Nielsen, *Phys. Rev. A* **66**, 032110 (2002).
- [96] S. J. Gu, H. Q. Lin, and Y. Q. Li, *Phys. Rev. A* **68**, 042330 (2003).
- [97] J. J. Mendoza-Arenas, R. Franco, and J. Silva-Valencia, *Phys. Rev. A* **81**, 062310 (2010).
- [98] W. K. Wootters, *Phys. Rev. Lett.* **80**, 2245 (1998).
- [99] J. Schliemann, *Phys. Rev. A* **68**, 012309 (2003).
- [100] Y. Q. Li and G. Q. Zhu, *quant-ph/0408155* (2004).
- [101] A. Peres, *Phys. Rev. Lett.* **77**, 1413 (1996).
- [102] M. Horodecki, P. Horodecki, and R. Horodecki, *Phys. Lett. A* **223**, 1 (1996).
- [103] S.-B. Li, Z.-X. Xu, J.-H. Dai, and J.-B. Xu, *Phys. Rev. B* **73**, 184411 (2006).
- [104] Z. Sun, X. Wang, A. Hu, and Y. Q. Li, *Physica A* **370**, 483 (2006).
- [105] Z. Sun, X. Guang, and H.-N. Xiong, *Physica A* **388**, 1337 (2009).
- [106] Z. Sun, X.-M. Lu, H.-N. Xiong, and J. Ma, *New J. Phys.* **11**, 113005 (2009).
- [107] X. Hao and S. Zhu, *Phys. Lett. A* **366**, 206 (2007).
- [108] H. Huang, X. Wang, Z. Sun, and G. Yang, *Physica A* **387**, 2736 (2008).
- [109] X. Wang and Z. D. Wang, *Phys. Rev. A* **73**, 064302 (2006).

BIBLIOGRAPHY

- [110] F. Wang, H. Jia, H. Zhang, X. Zhang, and S. Chang, *Sci. China Ser. G - Phys. Mech. Astron.* **52**, 1919 (2009).
- [111] F. Wang, L.-P. Fu, and K.-T. Guo, *Commun. Theor. Phys.* **50**, 341 (2008).
- [112] G.-H. Yang and L. Zhou, *Phys. Scripta* **78**, 025703 (2008).
- [113] A. W. Holleitner, H. Knotz, R. C. Myers, A. C. Gossard, and D. D. Awschalom, *Appl. Phys. Lett* **85**, 5622 (2004).
- [114] E. Solano-Carrillo, R. Franco, and J. Silva-Valencia, accepted in *Solid State Comm.* (2010).
- [115] G.-S. Tian and H.-Q. Lin, *Phys. Rev. B* **70**, 104412 (2004).
- [116] G. Vidal and R. F. Werner, *Phys. Rev. A* **65**, 032314 (2002).
- [117] K. Audenaert, J. Eisert, M. B. Plenio, and R. F. Werner, *Phys. Rev. A* **66**, 042327 (2002).
- [118] J. Kofler, V. Vedral, M. S. Kim, and C. Brukner, *Phys. Rev. A* **73**, 052107 (2006).
- [119] H. Wichterich, J. Molina-Vilaplana, and S. Bose, *Phys. Rev. A* **80**, 010304(R) (2009).
- [120] S. Marcovitch, A. Retzker, M. B. Plenio, and B. Reznik, *Phys. Rev. A* **80**, 012325 (2009).
- [121] A. Bayat, P. Sodano, and S. Bose, *Phys. Rev. B* **81**, 064429 (2010).
- [122] V. Vedral and M. B. Plenio, *Phys. Rev. A* **57**, 1619 (1998).
- [123] S. Bose and V. Vedral, *Phys. Rev. A* **61**, 040101(R) (2000).
- [124] T.-C. Wei, K. Nemoto, P. M. Goldbart, P. G. Kwiat, W. J. Munro, and F. Verstraete, *Phys. Rev. A* **67**, 022110 (2003).
- [125] M. Ziman and V. Bužek, *Phys. Rev. A* **72**, 052325 (2005).
- [126] D. McHugh, M. Ziman, and V. Bužek, *Phys. Rev. A* **74**, 042303 (2006).
- [127] U. Fano, *Rev. Mod. Phys.* **29**, 74 (1957).
- [128] A. Ferreira, A. Guerreiro, and V. Vedral, *Phys. Rev. Lett.* **96**, 060407 (2006).
- [129] T. Sakai and K. Okamoto, *Phys. Rev. B* **65**, 214403 (2002).
- [130] I. Affleck et al., *Phys. Rev. Lett.* **59**, 799 (1987).
- [131] J. L. Cardy, *J. Phys. A* **17**, L385 (1984).

BIBLIOGRAPHY

- [132] H. W. J. Blöte, J. L. Cardy, and M. P. Nightingale, *Phys. Rev. Lett.* **56**, 742 (1986).
- [133] I. Affleck, *Phys. Rev. Lett.* **56**, 746 (1986).
- [134] M. Steiner et al., *Adv. Phys.* **25**, 87 (1976).
- [135] S. Ramasesha et al., *Synth. Met.* **85**, 1019 (1997).
- [136] T. D. Kühner and S. R. White, *Phys. Rev. B* **60**, 335 (1999).
- [137] S. K. Pati and R. R. P. Singh, *Phys. Rev. B* **60**, 7695 (1999).
- [138] T. D. Kühner et al., *Phys. Rev. B* **61**, 12474 (2000).
- [139] C. Raas et al., *Phys. Rev. B* **69**, 041102 (2004).
- [140] M. A. Cazalilla and J. B. Marston, *Phys. Rev. Lett.* **88**, 256403 (2002).
- [141] H. G. Lou et al., *Phys. Rev. Lett.* **91**, 049701 (2003).
- [142] A. J. Daley et al., *J. Stat. Mech.: Theor. Exp.* p. P04005 (2004).
- [143] S. R. White and A. E. Feiguin, *Phys. Rev. Lett.* **93**, 076401 (2004).
- [144] M. Suzuki, *Prog. Theor. Phys.* **56**, 1454 (1976).
- [145] D. Gobert et al., *Phys. Rev. E* **71**, 036102 (2005).
- [146] V. Hunyadi et al., *Phys. Rev. E* **69**, 066103 (2004).
- [147] G. Vidal, *Phys. Rev. Lett.* **91**, 147902 (2003).
- [148] P. Calabrese and J. Cardy, *J. Stat. Mech.: Theor. Exp.* p. P04010 (2005).
- [149] G. D. Chiara et al., *J. Stat. Mech.: Theor. Exp.* p. P03001 (2006).
- [150] V. Eisler and I. Peschel, *J. Stat. Mech.: Theor. Exp.* p. P06005 (2007).
- [151] V. Eisler et al., *J. Stat. Mech.: Theor. Exp.* p. P01023 (2008).
- [152] M. Drillon et al., *Phys. Lett.* **96A**, 413 (1983).
- [153] S. Yamamoto et al., *Eur. Phys. J. B* **15**, 211 (2000).
- [154] M. Takahashi, *Phys. Rev. B* **40**, 2494 (1989).
- [155] M. Takahashi and M. Yamada, *J. Phys. Soc. Jpn.* **54**, 2808 (1985).

BIBLIOGRAPHY

- [156] F. Verstraete, Phys. Rev. Lett. **93**, 207204 (2004).
- [157] M. Zwolak and G. Vidal, Phys. Rev. Lett. **93**, 207205 (2004).
- [158] F. Verstraete et al., Phys. Rev. Lett. **93**, 227205 (2004).
- [159] A. E. Feiguin and S. R. White, Phys. Rev. B **72**, 220401(R) (2005).
- [160] T. Xiang, Phys. Rev. B **58**, 9142 (1998).
- [161] S. Sota and T. Tohyama, Phys. Rev. B **78**, 113101 (2008).
- [162] S. R. White, Phys. Rev. Lett. **102**, 190601 (2009).
- [163] J. Ribas et al., Coord. Chem. Rev. **193-195**, 1027 (1999).
- [164] J.-P. Costes et al., New J. Chem. **30**, 572 (2006).
- [165] N. B. Ivanov et al., Phys. Rev. B **58**, 14456 (1998).
- [166] T. Kennedy, J. Phys.: Condens. Matter **2**, 5737 (1990).
- [167] S. R. White and D. A. Huse, Phys. Rev. B **48**, 3844 (1993).
- [168] I. Affleck et al., Commun. Math. Phys. **115**, 477 (1988).
- [169] S. H. Glarum et al., Phys. Rev. Lett. **67**, 1614 (1991).
- [170] A. V. Syromyatnikov and S. V. Maleyev, JETP Letters **79**, 221 (2004).
- [171] Y. Yoshida et al., J. Phys. Soc. Jpn. **74**, 2917 (2005).
- [172] N. Fukushima et al., Physica B **359-361**, 1409 (2005).
- [173] H. H. Fu et al., Phys. Lett. A **358**, 443 (2006).
- [174] M. S. Reis et al., J. Phys.: Condens. Matter **19**, 446203 (2007).
- [175] S.-H. Qu and L. Zhu, Phys. Lett. A **372**, 5918 (2008).
- [176] R. Cortés et al., Inorg. Chem. **36**, 677 (1997).
- [177] T. Barthel et al., Phys. Rev. B **79**, 245101 (2009).
- [178] X. Wang and T. Xiang, Phys. Rev. B **56**, 5061 (1997).
- [179] K. Maisinger and U. Schollwöck, Phys. Rev. Lett. **81**, 445 (1998).
- [180] U. Schollwöck, Physics **2**, 39 (2009).
- [181] E. M. Stoudenmire and S. R. White, arXiv: cond-mat/1002.11305v1 (2010).